Development of ultrasound localization microscopy to measure cerebral perfusion during stroke : a study in mouse models prior to its translation in humans

Vincent Hingot

Sorbonne Université

ED 391 - SMAER

Physics for Medicine Paris

Development of Ultrasound Localization Microscopy to measure cerebral perfusion during stroke

A study in mouse models prior to its translation in humans

Par Vincent Hingot

Thèse de doctorat de Physique

Dirigée par Dr Olivier Couture

Présentée et soutenue publiquement le 09/12/2019

Devant un jury composé de :

- Gianmarco Pinton (Rapporteur)
- Emmanuel Bossy (Rapporteur)
- Lori Bridal
- Cyrille Orset
- Denis Vivien
- Thomas Deffieux
- Mickael Tanter
- Olivier Couture (Directeur de thèse)

Résumé en Français

L'échographie est une technique d'imagerie médicale employant des ultrasons. Un examen classique se base sur deux modes principaux, le mode B pour l'imagerie anatomique et le mode Doppler pour l'imagerie des flux sanguins. Dans le contexte des maladies cérébro-vasculaires, l'échographie sert principalement à estimer les altérations du flux sanguin dans les artères cérébrales majeures au travers du Doppler transcranien. Cependant, la faible qualité des images à travers le crâne ne permet pas à l'échographie d'être aussi performante que l'imagerie par résonance magnétique. Les récents progrès en échographie ont permis l'émergence de nouveaux modes d'imagerie, en particulier une technique de super-résolution ultrasonore qui permet d'augmenter la résolution ainsi que le contraste de l'imagerie vasculaire. Elle se base sur l'imagerie rapide de microbulles couramment utilisées comme agents de contraste pour l'échographie. En utilisant cette méthode, il a été possible d'imager jusqu'aux plus petits vaisseaux et permettrait chez l'homme l'imagerie de la perfusion cérébrale de manière plus performante que le Doppler transcranien. Cela pourrait rendre possible une prise en charge plus précoce et plus efficace des patients victimes d'accidents vasculaires cérébraux.

Avant d'être utilisée dans un contexte médical, la technique de super-résolution ultrasonore doit être mieux comprise, mieux réalisée, et adaptée au contexte particulier des accidents vasculaires cérébraux. En particulier, ce manuscrit discutera des meilleures méthodes de formation d'image, et se penchera sur les performances réelles de l'imagerie super résolue. Nous discuterons également des possibilités de corriger les artefacts dus aux mouvements physiologiques et des possibilités d'utiliser l'imagerie super résolue dans divers organes et en particulier les reins, les tumeurs et la moelle épinière. L'étude approfondie par imagerie super résolue de modèles d'ischémie cérébrale chez le rongeur permettra de construire des biomarqueurs vasculaires adaptés au diagnostic des pathologies cérébro-vasculaires et devrait aider la translation vers des patients humains.

Abstract

Ultrasonography is a medical imaging technique that uses ultrasound. A typical examination is based on two main modes, B-mode for anatomical imaging and Doppler mode for blood flow imaging. In the context of cerebrovascular diseases, ultrasonography is used primarily to estimate alterations in blood flow in major cerebral arteries through transcranial Doppler. However, the low quality of the images through the skull does not allow ultrasound to be as efficient as magnetic resonance imaging. Recent advances in ultrasound have led to the emergence of new modes of imaging, particularly a super-resolution ultrasound technique that increases the resolution and contrast of vascular imaging. It is based on the rapid imaging of microbubbles commonly used as contrast agents for ultrasound. This method has shown that it can image even the smallest vessels and allows to perform cerebral perfusion imaging more effectively than Transcranial Doppler. This would allow earlier and more effective management of stroke patients.

Before being used in a medical context, this ultrasound super-resolution technique must be better understood, better realized, and adapted to the particular context of cerebrovascular diseases. In particular, this manuscript will discuss how to best form images, and will look at the actual performance of super-resolved imaging. We will also discuss the possibilities of correcting artefacts due to physiological movements and the possibilities of using super-resolved imaging in various organs, particularly the kidneys, tumors and spinal cord. Finally, imaging of models of cerebral ischemia in rodents will enable the construction of vascular biomarkers suitable for the diagnosis of cerebrovascular pathologies and should aid translation into human patients.

Summary

Chapter 1: Ultrasound for cerebral perfusion imaging in stroke medical care

1. Stroke is a serious health issue

Cognitive and vascular organization in the human brain

To ensure proper functionality of all vital functions, our organs have to be continuously provisioned with oxygen and nutrients which are transported through the circulatory system. This system is a closed and complex network of vessels going to and from the heart allowing constant circulation of blood. The capillaries are the vessels with the smallest diameter (< 10 μm) and the slowest flow (<1 $mm.s^{-1}$). They allow most of the exchanges of oxygen and nutrients between blood and tissues.

The brain requires a high and constant supply of nutrients to ensure proper cognitive abilities. This supply is ensured by a specific vasculature feeding on the Common Carotid Arteries (CCA) and Vertebral Arteries (VA) flowing on the side and back of the neck (*Figure 1.A*). Before reaching the brain, the CCA separate in the External Carotid Arteries (ECA) which feed the face and the Internal Carotid Arteries (ICA) which feed the brain. Once they penetrate the skull, the ICA reaches a communicating ring called the circle of Willis, responsible for balancing blood flow and blood pressure in the brain. From this ring are branched the major cerebral arteries that are the Middle Cerebral Arteries (MCA) that flow on the sides of the brain, the Anterior Cerebral Artery (ACA) and Posterior Cerebral Artery (PCA) which flow on the outer front and outer back of the brain. The major arteries then separate in smaller arterioles until reaching the capillaries. The capillaries then regroup in bigger venules until reaching major cerebral sinuses and eventually the jugular and vertebral veins to go back to the heart.

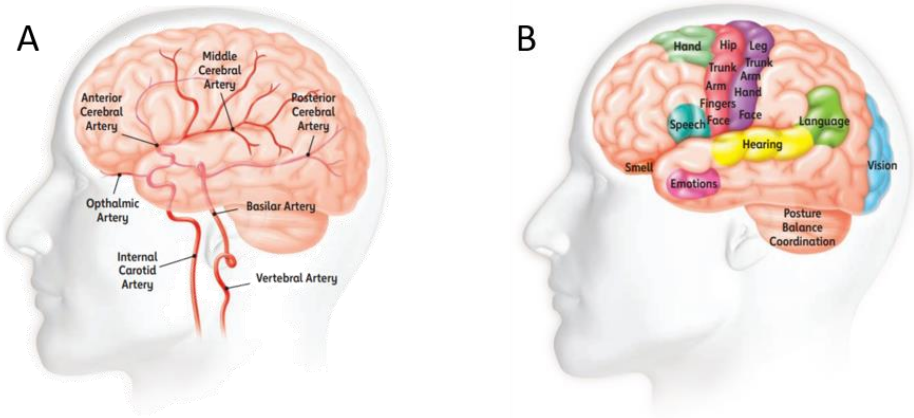

Figure 1: Vascular and cognitive organization of the brain

A. Organization of the cerebral arterial network. **B**. Examples of cognitive structures often affected by stroke. (Images from American Stroke Association Brochure)

The major cerebral arteries each have a well-defined territory. In the territory of the MCA, for instance, are some cognitive areas associated with motor control, in particular of the face and superior limbs, spatial consciousness, hearing, and speech (*Figure 1.B*). Any alteration of blood flow in the MCA causes impairment in those functions and symptoms such as loss of muscle function in the face and superior limbs, impairment of speech, loss of balance, etc.

Stroke is a major alteration of cerebral blood flow

Stroke is the generic term referring to the shortage of oxygen and nutrients caused by impaired blood supply to the brain. In 80% of the case, stroke is of ischemic origin and caused by the formation or the migration of a clot (*Figure 2.A*), which causes the occlusion of a major cerebral artery. In a majority of cases, this happens in the MCA and causes cognitive impairments of speech, motor function, spatial consciousness, etc. In the remaining 20% of the cases, stroke is caused by a hemorrhage following a trauma or the rupture of an aneurism (*Figure 2.B*). The shortage of flow can be caused by a downstream shortage or by a peripheral hematoma causing compression of the tissue thus preventing blood supply.

In France, 130 000 persons are estimated to suffer a stroke every year (***French Health Ministry, 2009***), that is one person every 5 minutes! More generally, about 1 in 6 people will suffer a stroke in the course of their life and around 35 % of them will die within the first year. 60 % of the survivors suffer from heavy neurological sequels. Age is a major risk factor as 75% of cases involve people over 65 years old, together with hypertension, diabetes, and high cholesterol. Like cardio-vascular diseases, unhealthy living habits dramatically increase the risk to suffer a stroke *(**World Health Organization, 2014**)*.

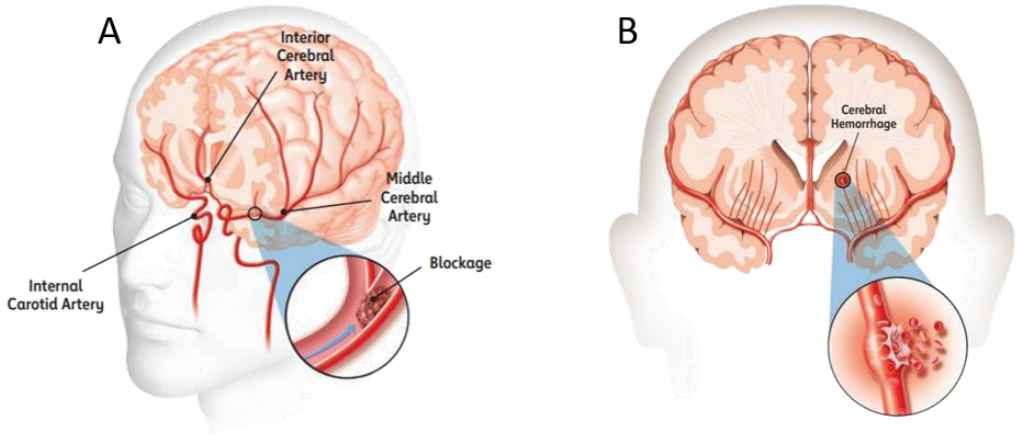

Figure 2: Stroke is an alteration of cerebral blood flow

A. Ischemic stroke caused by a clot in the MCA. **B**. Hemorrhagic stroke caused by the rupture of a secondary artery. (Images from American Stroke Association Brochure)

Establishing a diagnosis requires cerebral imaging

When being deprived of blood and oxygen, cells quickly start to die. It is estimated that every minute, 2 million neurons are destroyed (***Saver L et al. 2006***). After 10 hours, most cells in the infracted area of the brain are lost forever. The gimmick "time is brain" is often used to emphasize the necessity of quick medical care to limit the damages. Although ischemic and hemorrhagic stroke have opposite causes, the external symptoms are unfortunately very similar. In most cases, patients experience numbness, confusion, aphasia, motor dysfunction, headaches, and in the most severe cases, loss of consciousness or death. Because the symptoms are similar, a clear diagnosis requires cerebral imaging which delays the time to treatment.

In the case of ischemia, which is the most common cause of stroke, thrombolytic agents like recombinant tissue plasminogen activator (rtPA) (***Zivin J et al. 1985, Thiebault A et al. 2018***) better known in its commercial form Alteplase, must be injected to dissolve the clot and restore arterial function and blood supply to the cerebral tissue. They can be administered in combination of thrombectomy (***Campbell B et al. 2019, Berkhemer O et al. 2015***), a surgical procedure to remove the clot. The efficiency of both thrombolytic agents and thrombectomy decreases rapidly with time. After the onset of the stroke, treatments remain effective only during an estimated therapeutic window of 6 to 9 hours (***Campbell B et al. 2019***). The injection of thrombolytic agents should be performed as soon as possible and ideally in the ambulance. Unfortunately, in the case of hemorrhagic stroke, thrombolytic agents are contraindicated as they increase the risks of hemorrhage (***Campbell B et al. 2019, Berkhemer O et al. 2015***). Although ischemic stroke is far more common, thrombolytic treatment cannot be started in the ambulance because of the risk of the stroke being of hemorrhagic origin. In order to make the diagnosis and chose the adapted treatment, cerebral imaging must be performed before any treatment can be administered (***Birenbaum D et al. 2011, Srinivasan A et al. 2006, Wintermark M et al. 2005***). The issue of neurovascular imaging is therefore crucial for good medical care.

2. Different methods of cerebral imaging

The history of medicine relies heavily on the progress of physical sciences and in particular on the emergence of new imaging methods. The works of Robert Hook on optics and lenses lead to the construction of a microscope which enabled the first observation of cells in 1667. The work of Wilhelm Röntgen on X-rays enabled the construction of the first medical system being able to see through tissues in 1895. Later, Marie Curie further pushed this idea and developed the first mobile radiographic units. The work of Paul Langevin in acoustics enabled the construction of the first medical ultrasound system by John Wild in 1952. The work of Felix Bloch on nuclear magnetism eventually lead to the construction

of the first MRI system in 1973 (***Rinck PA et al. 2008***). Other major progress in physics, in particular, nuclear physics, nonlinear optics, fluorophore chemistry, acoustic time reversal, etc. together with drastic improvement of computational abilities now offer a wide range of ways to examine the brain. Unfortunately, no method is currently perfect and several methods are used concurrently to address different issues. In the context of stroke, the following methods are the most widely used.

As humans, using our eyes and visible light to image object is the most intuitive way to characterize objects. However, light only enables imaging within a limited depth. The propagation of light in tissues changes regime along propagation. A ballistic regime exists during the first 100 μm where the beam keeps it coherence and allows for direct microscopy. Up to 1 mm, the beam is backscattered but remains coherent and is used in confocal, multi-photon microscopy and in Optical Coherence Tomography (OCT, ***Adhi M et al, 2013***). Beyond 1 mm, the light enters a diffusive regime, loses its coherence and cannot be used for direct imaging although it can be used as a source of contrast for other imaging modalities. Moreover, light doesn't propagate far enough through the human skull to be a practical method in stroke units. In preclinical studies, however, the skull can be removed or thinned to allow light to directly penetrate in the brain. Optical methods can be used to assess the blood flow at the surface of the brain.

In Laser Doppler Flowmetry (***Swiontkowski M et al. 1991***), an optical fiber is placed over an exposed area of the brain to illuminate the MCA and produces a signal proportional to blood velocity (*Figure 3.A*). It has been used in the context of stroke to characterize arterial patency in a thromboembolic model (***Orset C et al. 2009***). In Doppler Speckle Contrast Imaging (***Boas D et al 2010***), some characterization of cerebral perfusion can be achieved though it is limited to the surface of the brain (*Figure 3.B*). Two photons microscopy (***Denk W et al, 1990***) is used to provide intra vital characterization of blood vessels with a microscopic resolution. It is at this day the most precise tool that exists to study blood flow in vivo. However, it is fairly invasive as the skull has to be removed and the field of view is limited. It has been used to describe blood flow alteration in stroke model with great precision *(**Schrandt C et al. 2015**)* but only within a depth < 1mm (*Figure 3.C*).

Photoacoustic uses light absorption in tissues as it creates a mechanical wave that can be recorded. Either with optical resolution (OR-PAM, *Figure 3.D*) but limited to 1 mm depth (***Hu D et al. 2011, Cao R et al. 2018***) or with acoustical resolution (AR-PAM, *Figure 3.E*) with greater penetration but lower resolution (***Wang L et al. 2016***). To my knowledge, no study has been performed in animal models of stroke though it could bring interesting insights on tissue oxygenation and vascularization in both the acute and the recuperation phase.

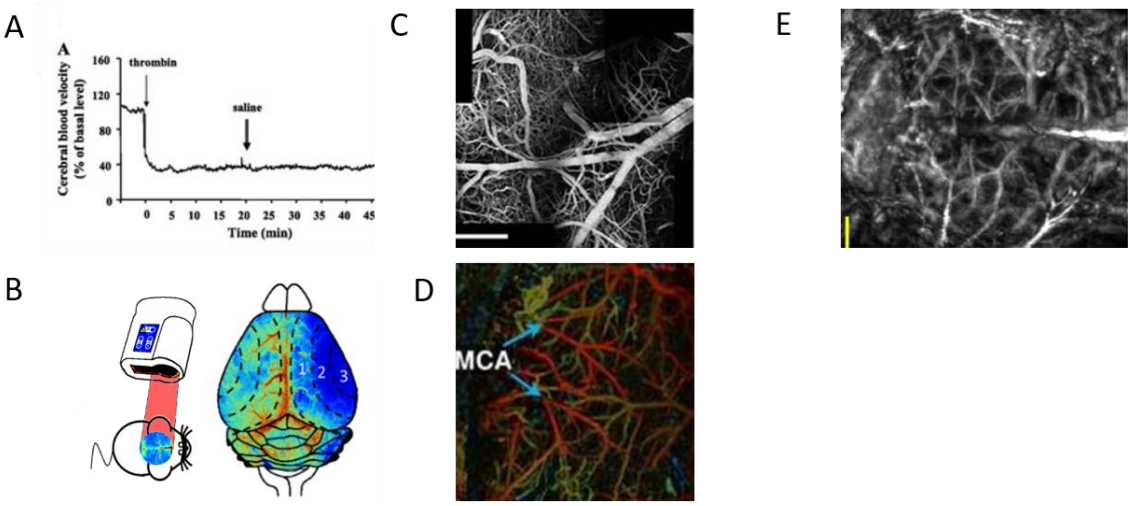

Figure 3: Optical methods for cerebral perfusion imaging in small animals

A. Laser Doppler Flowmetry (LDF) in ischemic stroke (***Orset C et al. 2009***). B. Doppler Speckle Contrast Imaging (DSCI) in ischemic stroke (***Anfray A et al. 2017***). C. Multiple photon microscopy in a stroke model (***Schrandt C et al. 2015***). D. OR-PAM to image oxygenation during stroke (***Cao R et al. 2018***). E. AR-PAM in a naïve model of mouse (***Hu s et al. 2010***).

Shear Wave Elastography (SWE) is an imaging modality sensitive to mechanical properties of tissues. The tissue is submitted to a calibrated stress and the consequent strain is observed. The most common stress is the use of shear waves. The velocity of the shear wave propagation is directly linked to the viscoelastic properties of the tissue. The propagation of the shear wave can be imaged using ultrafast ultrasound. In a rat model of stroke, it showed that the brain softens days after an infarct (***Frieman F et al. 2013, Martin A et al. 2012***). However, to perform this study, the skull of the animal had to be removed, which is a real limitation for potential use in both clinical and preclinical situations.

Near Infrared Spectroscopy (NIRS) relies on multiple near-infrared captors placed over the head of a patient. The infrared beam excites *C-H*, *O-H* and *N-H* chemical bounds. Hemoglobin (*Hb*) carries oxygen and can be found in its oxygenized form *Oxy-Hb* and its deoxygenized form *Deoxy-Hb*. Because they don't have the same number of *O-H* bounds, their infrared spectrum will vary which will give a quantification of oxygenation. In particular, the INVOS systems can be used in the context of stroke (***Nemoto E et al, 2000***). However, the oxygenation level and its link with the severity of the stroke vary drastically between patients and does not allow a better decision making than other existing techniques.

Positron Emission Tomography (PET) and Single Positron Emission Computed Tomography (SPECT) are imaging methods used to image cerebral metabolism. In Situ accumulation of radioactive tracers during metabolic activity produces the emission of γ photons that reveals the location and intensity of metabolic processes and in particular the uptake of glucose. Despite a great sensitivity, spatial and temporal resolutions of PET and SPECT are limited. Costly infrastructures are required to produce the radioactive tracers which ultimately reduce their use in case of stroke. However, it is crucial to understand how the brain suffers and recovers and remains an important tool for research on cerebrovascular diseases.

Computed Tomography (CT) is widely available for stroke evaluation (***Birenbaum D et al. 2011, Srinivasan A et al. 2006, Wintermark M et al. 2005***). Computing the absorption map of X-Rays in 3D reveals anatomical structures deep in the brain (*Figure 4.A*) and blood vessels (*Figure 4.B*). Perfusion CT (PCT) requires the injection of Iodine based contrast agents but can estimate the main cerebral perfusion parameters such as Cerebral Blood Volume (CBV), Cerebral Blood Flow (CBF) and Mean Transit Time (MTT). Xenon CT (XeCT) is another contrast method to measure diffusion efficiency in tissues. However, poor resolution and sensitivity doesn't always allow for proper reading of cerebral abnormalities, and when possible, Magnetic Resonance Imaging (MRI) is recommended.

MRI relies on coupling between nuclear spin in the atoms of the tissue and an external magnetic field. Being immersed in a static magnetic field, nuclear spins align along the field lines. A radiofrequency pulse is sent to pivot the spins orientations and the times to realignment are measured and reveal information on the environment of the atoms. Different parameters can be derived from different radiofrequency sequences and different topography of the static magnetic field like T_1, T_2, T_1* and T_2* relaxation (*Figure 4.C*). Diffusion Weighted Imaging (DWI) exploit anisotropic water diffusion to characterize the orientation of tissue fibers. Time of Flight (TOF) sequences are used to perform an MR Angiography (*Figure 4.D*). Arterial Spin Labeling (ASL) is used to assess alteration in blood flow as it is often used as a non-contrast perfusion map. In Perfusion Weighted Imaging (PWI), the injection of contrast agents enables better reading of perfusion parameters such as CBV, CBF, and MTT. Because it can measure a wide range of cerebral parameters with a good resolution, MRI is the gold standard in medical care and research units for stroke. However, its extensive cost of installation and maintenance often limits its availability, especially in poor or remote areas (***Birenbaum D et al. 2011, Srinivasan A et al. 2006, Wintermark M et al. 2005***).

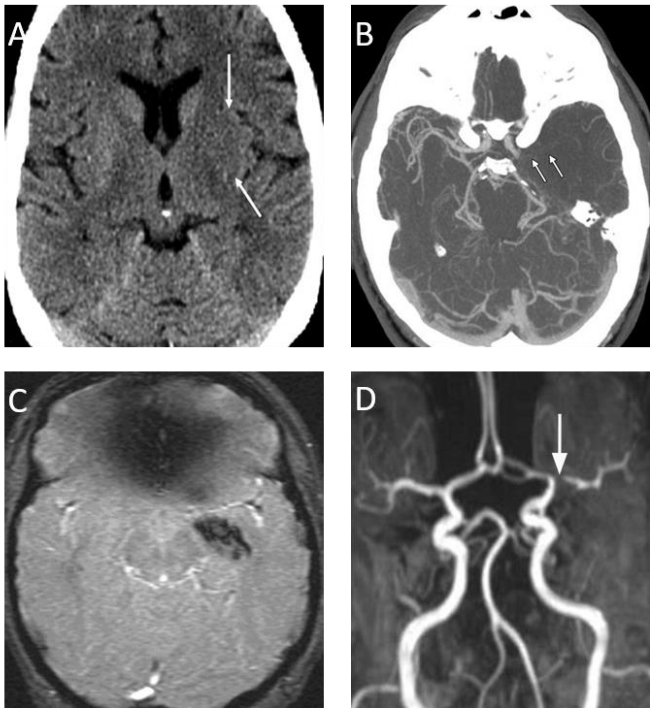

Figure 4: non contrast CT and MRI in ischemic stroke

A. Non contrast CT-scan. B. CT-scan Angiography. C. T_2 weighted MRI. D. Time Of Flight MR Angiography. (Images adapted from ***Srinivasan A et al. 2006)***.

Quick access to imaging, although vital, is often not possible. If CT-scan can be used as a replacement for MRI, they are not as efficient and the French Safety Authority (***Haute Autorité de Santé***) recommend the systematic use of MRI when possible, even if it means further delaying treatment. Unfortunately, MRI systems are costly and not always accessible for a large population. In France, only 10 MRI are available for every million people (***SFR. 2014***, ***La Croix. 2014***) with major territorial inequalities (*Figure 5*). If 9 out of 10 emergency units have access to an MRI, only half of them can provide a 24h/24h access. For stroke, only 1 in 5 patients receive an MRI in first intention, and the delay is longer than 6 hours in 40% of the cases. Moreover, most acquisition sequences in MRI last tens of minutes and the emergency doesn't allow for an exhaustive use of MRI as the acquisition time should be kept to a minimum (***Desal H.A. et al. 2008***). Because the therapeutic window for thrombolysis and thrombectomy is only of 6 to 9 hours (***Campbell B et al. 2019***), a major improvement for stroke medical care would be the development of a cheap and transportable device that would discriminate between ischemic and hemorrhagic stroke so as to start treatment as early as possible. Some prototype of transportable CT and PET exist (***Melroy, S et al 2017***), but are complex and imperfect solutions. Ideally, ultrasound could play an important role in medical care for stroke as it could be transportable and relatively cheap. However, the quality of transcranial imaging today is too limited.

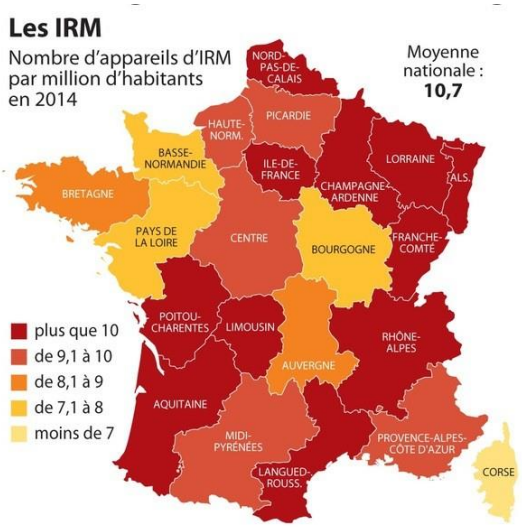

Figure 5: Repartition of MRI systems in France (La Croix, 2014)

Transcranial Doppler (TCD) is an ultrasound based method for flow assessment in major cerebral vessels (*Figure 6*). Imaging through the thinner parts of the skull allows for some form of ultrasound characterization of blood flow in the circle of Willis and in the MCA which is by far the most commonly affected artery. Because ultrasonography is a cheap and easy method, the importance of TCD increases in stroke units. Nonetheless, because of strong attenuation when propagating through the skull bone, the quality of the reading is often limited for cerebral imaging (***Blanco P et al. 2018***) even in combination with the injection of microbubbles (MB) as ultrasound contrast agents (UCA). It also requires a trained radiologist to perform the exam, so TCD suffers from its large dependency to the operator (***Birenbaum D et al. 2011***).

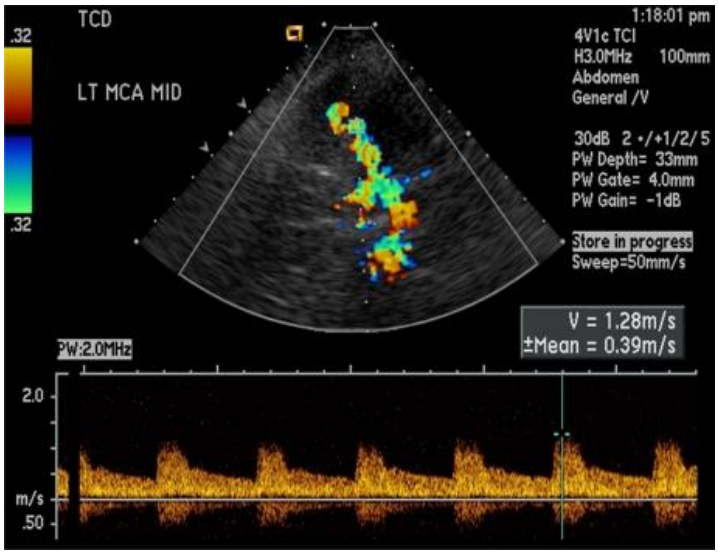

Figure 6: Transcranial Doppler in healthy patient's Middle Cerebral Artery ***(Birenbaum D et al. 2011)***

Ultrasound imaging could be the method neuroradiologists dream of

The imaging technique that neurologists and neuroradiologists would dream of should be easily available, could be bedside (as TCD), repeatable and require no toxic contrast agents (as ASL), provide quantitative measurement (as PET and XeCT) and measure multiple perfusion parameters (as PCT) (***Wintermark M et al. 2005, Essig M et al. 2013***). It should also have a limited dependency to the operator. Recent progress in ultrasound imaging could eventually lead to the development of a performant ultrasound based imaging method that could fit all these objectives. Ideally, such a device could be relatively cheap and transportable so as to be easily dispatched in ambulances and remote areas, 3D so as to limit the dependency to the operator, and repeatable so as to monitor the response to treatment during the following days. It could be used as an emergency imager that could be used earlier and more often than MRI although I foresee that the precision and richness enabled by MRI imaging will remain the optimal gold standard in stroke.

The recent progress in ultrasound imaging mainly come from a drastic improvement in frame rate. Among other things, it enabled to develop a super resolution method which overcomes the fundamental diffraction limit for spatial resolution. This thesis is about this super resolution method and will discuss how it works and how it performs in terms of spatial and temporal resolution. The following section aims at introducing some concepts of ultrasound imaging needed to understand how this super resolution method works and how it compares with other ultrasound imaging methods. It is inspired in particular by ***Imaging of Complex Media with Acoustic and Seismic Waves*** published by Matthias Fink and colleagues in 2002 and in particular the chapter *ultrasound and its modeling* written by Jorgen Jensen, and ***Foundations of biomedical ultrasound*** by Richard S. Cobbold published in 2007. I was more generally inspired by lectures in ESPCI on wave physics by Arnaud Tourin and Mathias Fink, optics by Rémi Carminati and signal processing by Emmanuel Bossy.

3. Fundamentals of ultrasound imaging

Acoustic propagation in complex medium

A wave is a field that satisfies the wave propagation equation (1). Acoustic waves can be described using the pressure field p in a point of space $\vec{r}$ and time t. The interaction between the wave and the tissues can be described as a source S which depends on the media's density ρ, compressibility χ, and absorption coefficient α and that is simplified as a field $s(\vec{r}, t)$.

$$\Delta p - \frac{1}{c^2}\frac{\partial^2 p}{\partial^2 t} = S(\phi, \delta\rho, \delta\chi, \delta\alpha) = s(\vec{r}, t) \qquad (1)$$

In particular, the solution when the source is punctual and emitting a brief signal is called the spatio temporal Green's function where δ is the Dirac peak function and $\vec{r}_0$ the position of the source.

$$g(\vec{r},t) = \frac{\delta(t - \frac{|\vec{r} - \vec{r}_0|}{c})}{4\pi|\vec{r} - \vec{r}_0|} \qquad (2)$$

In ultrasound imaging, an ultrasound transducer sends a pulse in an inhomogeneous media described as a source field $s(\overrightarrow{r_1},t)$. The pressure field $p(\overrightarrow{r_2},t)$ is then recorded by the transducer and is generally referred to as radiofrequency or RF data. $\overrightarrow{r_1}$ & $\overrightarrow{r_2}$ are spatial coordinates in the media and along the transducer respectively. The pressure field after emission and propagation is given by equation (3) using spatial and temporal convolution products (*G.E. Tupholme 1969, P.R. Stepanishenn 1971, J. A. Jensen 1992, J. A. Jensen 1997*).

$$p(\overrightarrow{r_2},t) = em(t)\otimes^t s(\overrightarrow{r_1},t)\otimes^{\vec{r}} h_e(\overrightarrow{r_1},\overrightarrow{r_2},t)\otimes^{\vec{r}} h_r(\overrightarrow{r_1},\overrightarrow{r_2},t) = s(\overrightarrow{r_1},t)\otimes h(\overrightarrow{r_1},\mathrm{t}) \quad (3)$$

$em(t)$ acounts for the emitted vibration by the transducer and the electromechanical coupling of the elements, $s(\overrightarrow{r_1},t)$ the source field that is considered static so $s(\overrightarrow{r_1},t) = s(\overrightarrow{r_1})$, and $h_e(\overrightarrow{r_1},\overrightarrow{r_2},t)$ and $h_r(\overrightarrow{r_1},\overrightarrow{r_2},t)$ correspond to the spatial impulse responses of the apertures in emission and reception and account for the shape of the beam and effects of diffraction by the transducers.

The formation of an image is the determination of the source field $(\overrightarrow{r_1})$ from the recorded pressure field $p(\overrightarrow{r_2},t)$. In the classical situation of a linear array exploring a 2D field, the coordinate system is simplified with $\overrightarrow{r_1} = (z,x)$ and $\overrightarrow{r_2} = x_0$ where x_0 is the direction along the transducer dimension. Theoretically the most precise approach would be to directly solve the inverse problem (*J. A. Jensen 1993*) for example through the estimation of the impulse responses and deconvolution methods.

However, these approaches are not that performant today, especially when the signal to noise ratio is poor and most approaches of image formation rely on a beamforming step which synthetically focus the signal back in space so that the amplitude of the beamformed signal is indicative of the real presence of a source in a specific position in space. Virtually, this mean considering the backscattered pressure field as the decomposition in spherical waves and forming an image as the amplitude of the signal scattered by single sources. This can be done using the Delay and Sum (DAS) beamforming method which decomposes the backscattered signal in a source of spherical waves emitted by punctual sources in the medium.

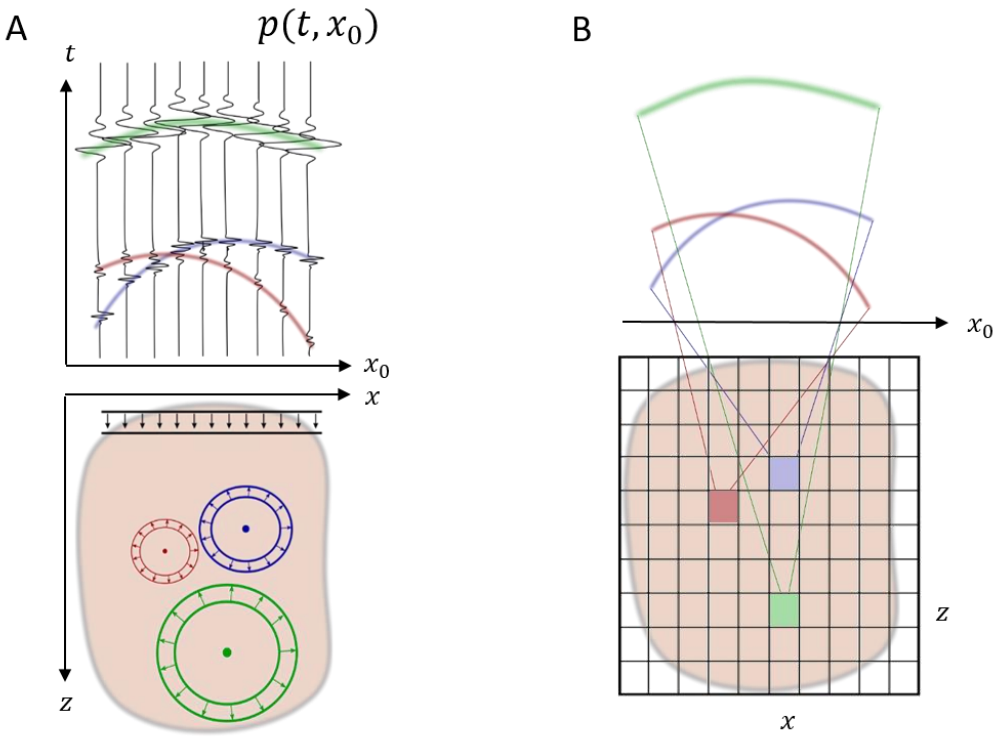

Figure 7: Principle of Delay and Sum beamforming

A. Scattering from the media is decomposed in punctual sources emitting spherical waves. B. The amplitude of the pressure wave created by a point (z, x) is determined through summing all contributions along a parabolic delay law.

The signal coming from a source in (z, x) will appear as a parabolic delay law along the transducer's dimension (*Figure 7.A*). This delay depends on the localization of the source point and is the sum of the delay from the transducer to the point τ_e and back from the point to the transducer τ_r. τ_e is the time that the wave will take to travel the distance z in the axial direction. For a spherical wave the propagation time from the source to the transducer is a parabolic delay law. The total delay is the sum of the forward and return delays and can be expressed for each element x_0 and source point (z, x).

$$\tau(x_0, z, x) = \tau_e + \tau_r = \frac{z}{c} + \frac{\sqrt{(z^2 + (x_0 - x)^2}}{c} \qquad (4)$$

To form an image, all contributions from the source are summed in the time domain along the corresponding parabolic delay (*Figure 7.B*) for a chosen set of elements D.

$$Im(z, x) = \int_D p(\tau(x_0, x, z), x_0) dx_0 \qquad (5)$$

This operation is analog as a focalization in reception as it equates to retro focusing the pressure field back in (x, z). The effects of spatial and temporal impulse responses are still present and can be gathered in a single spatial function called the point spread function (PSF) which is constitutive of the complete imaging system. It corresponds to the image of a punctual source. In practice, it is unknown and has a smoothing effect on the image. The characteristic dimension of this PSF will ultimately limit the capacity of the imaging system to separate close sources, which is the definition of the spatial resolution.

$$Im(x,z) = s(x,z) \otimes^{\vec{r}} PSF \qquad (6)$$

Pulse width and axial resolution

This representation as a spatial convolution hides the fact that what happens in the axial direction is governed mostly by temporal phenomenon whereas phenomena in the lateral direction are governed by diffraction. This implies that the resolution in the axial direction is determined by the temporal characteristics of the emitted pulse. The Rayleigh criterion states that two sources can be separated if they are closer than the full width at half maximum of the intensity repartition function. For the axial resolution, this means half the length of the pulse where n is the number of half cycles that are sent.

$$Res_{axiale} \sim c\frac{T}{2} = n\lambda \qquad (7)$$

Sending a shorter pulse improves the axial resolution. Virtually, the emission of a pulse is done by a transducer with a limited bandwidth and the shortness of the pulse will be limited to the order of one cycle. Moreover, sending short pulses reduces the overall energy that is sent in the medium and therefore reduces the contrast.

Beam width and lateral resolution

The PSF in the lateral direction is limited by the spatial impulses responses in emission and reception, in other words, by the width of the beam. The beamforming step is analog to a synthetic focalization and is submitted to the same spatial determinants. For a focused beam at a depth z, the pressure field is a function of the aperture's width D in (8).

$$p_z(x) \sim sinc(\frac{\pi x D}{\lambda z}) \qquad (8)$$

In focused ultrasound, both the emission and reception are focused beam (effective and synthetic) and the resulting PSF is a product of two $sinc$ functions and the first annulations then give the lateral resolution.

$$Res_{laterale} = \frac{\lambda z}{D} = \lambda f_{number} \quad (9)$$

In plane wave imaging, the focusing is only performed in reception as the emitted beam is a plane wave. The pressure field in emission is a constant along the lateral dimension which causes a widening of the PSF and therefore a loss of contrast and resolution. To address this issue, a synthetic focusing in emission can be done by sending and compounding a set of tilted plane waves (***Montaldo G. et al. 2009***). The resulting focalization depends on the number of plane waves sent but is at most as effective as the focused approach. Therefore, the resolution is at best the width of the beam in the case of focused ultrasound and limited to λf_{number}. The choice of the f_{number} defines the resolution that can be obtained. Usual values for the f_{number} are between 0.5 and 2. Like for the axial resolution, the lateral resolution is effectively limited to half a wavelength.

Beam attenuation and resolution tradeoff

When propagating in the media, the wave's amplitude exponentially decreases. A part of the energy of the incident wave is backscattered by the tissue. The rest of the energy is lost through viscous dissipation in the tissue. This attenuation is often modeled by an exponential decay whose coefficient depends on tissue properties and on the ultrasound wave central frequency. For example, the attenuation coefficient in water at 1 MHz is 0.002 dB.cm^{-1} whereas it is 1 dB.cm^{-1} at 50 MHz and 20 dB.cm^{-1} at 100 MHz meaning that half of the energy will be lost after 1.5m at 1 MHz, after 3 mm at 50 MHz and after 150 μm at 100 MHz. The attenuation coefficient of the skull bone at 1 MHz is around 8 dB.cm^{-1} meaning that after a round trip through a 7 mm layer of skull bone, the ultrasound wave will lose 10 dB. A measure of ultrasound wave penetration is the half energy distance, depth at which the wave will have lost half of its initial energy.

Both axial and temporal resolution are ultimately limited to half a wavelength. Smaller wavelengths (or higher central frequencies) provide better resolution but attenuate faster whereas longer wavelengths (or lower central frequencies) enable deeper imaging but at the cost of reduced resolution. This is the classical resolution/penetration tradeoff for ultrasound imaging that forces a choice of the central frequency and therefore a set of resolution and penetration for each organ to image (*Figure 8*).

Moreover, to penetrate through strongly attenuating structures, like the human skull, even lower frequencies should be used. To image the human brain, 1-2 MHz transducers are recommended, which limits the resolution to at best 1 mm. The diameter of the MCA is around 3 mm, and a resolution of 1 mm is, therefore, limiting when imaging such structures. Worst, the MCA is amongst the biggest cerebral arteries, and the downstream arteries will be smaller and therefore even harder to image in these conditions.

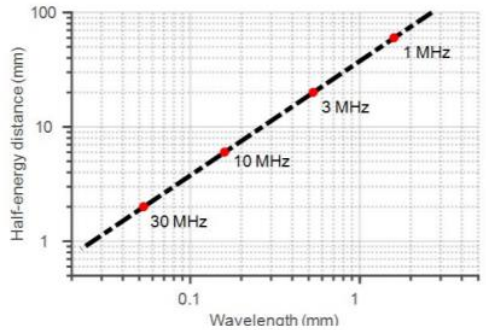

	Human brain	Human liver	Human breast	Rodent brain
f	1.5 MHz	3 MHz	8 MHz	15 MHz
λ	1 mm	0.5 mm	0.2 mm	0.1 mm
Depth	10 cm	7 cm	3 cm	1 cm

Figure 8: Resolution/Penetration tradeoff in ultrasound imaging

Half Energy Distance for different wavelength in log-log plot shows stronger attenuation with shorter wavelength. The table gives examples of the penetration/resolution tradeoff for different frequencies corresponding to usual imaging situations (***Couture O. et al. 2018***).

4. Imaging modes in medical ultrasound

Brightness mode

The most common imaging mode in ultrasound imaging is the brightness mode or B-mode. In the last section, we explained that the recorded echoes depend on the interaction between the ultrasound wave and the medium. The intensity of the backscattered signal depends on local variations of compressibility and density of the media (***Jensen J et al, 1991***). A B-mode image represents a combination of the media's density and compressibility inhomogeneities and local interference patterns that are convolved with the PSF of the imaging system resulting in a random granular pattern called speckle with a spatial variation length defined by the PSF. Organs have different speckle signatures, and appear as coherent shapes in the B-mode image which allows their detection and characterization. Among other applications, this mode is classically used for anatomical characterization, detection of abnormalities, identification of lesions, cysts and tumors, visualizing cardiac functions and guiding surgical procedures like injections or biopsies.

Pulsed Doppler

Pulsed and Color Doppler are the most common modes for blood flow imaging. When imaging moving scatterers, their velocity can be estimated using the pulsed Doppler Effect. When ultrasound pulses are regularly sent by a transducer at a moving target, the distance between the transducer and the target changes with the target's displacements which causes the echoes to be recorded with a slight delay $\Delta\tau$. The measurement of the delays allows for the measurement of the target's velocity in the axial direction using (10) where PRF is the emission pulse repetition frequency and v_z the axial velocity of the target.

$$\Delta\tau = \frac{2v_z}{cPRF} \qquad (10)$$

Methods for systematic axial displacement estimation have been developed to estimate both blood and tissue displacement (***Kasai S et al, 1985***). For IQ sampled data where two samples are acquired with a quarter period delay, the beamformed image is a complex image in which the phase can be used to estimate displacements. The axial velocity can for example be estimated using the lag-1 operator as a function of the pulse central frequency ω_0 and pulse repetition frequency ω_0.

$$\arg(IQ(z,x,k)IQ(z,x,k+1)^*) = \omega_0\Delta\tau = \omega_0\frac{2v_z(z,x)}{c\ PRF} \qquad (11)$$

This allows for tissue tracking but mostly for blood flow characterization. It is in particular useful to image large vessels and allows the diagnosis of cardiovascular pathologies, arterial and venous stenosis or thromboses, and in Transcranial Doppler where the velocity in the MCA is analyzed.

Ultrasensitive Doppler

Ultrasensitive Doppler is a method based on high pass filtering of sets of compounded plane waves. Because of the high signal to noise ratio resulting from the synthetic compounding and the improved temporal sampling of scatterers, it improves the sensitivity to blood flow by a factor 30 compared to conventional Doppler (***Bercoff J et al 2011***, ***Mace E et al 2013***). Among other things, it enabled the development of an ultrasound analog of functional MRI relying on the increased blood supply following a neural activity (***Mace E et al 2013***, ***Deffieux T et al 2018***). Functional Ultrasound (fUS) has been demonstrated in preclinical situations in healthy rodents (***Tiran E et al 2017***) and in models of stroke (***Brunner C et al 2017***) as well as in clinical situations where the skull was absent, in trepanned patients (***Imbault M et al 2017)*** and in newborns (***Demene C et al 2017)***. Ultrasensitive Doppler and fUS were also adapted in 3D (***Provost J et al 2015, Rabut C et al 2019***).

Contrast Enhanced Ultrasound (CEUS)

To enhance the sensitivity of ultrasound imaging to blood flows, microscopic gaseous microbubbles (MB) can be injected intravenously. Because those MB resonate at most medical ultrasound frequencies, their backscattered signal is brighter than other tissue and blood scatterers. In addition to pulsed and color Doppler, specific ultrasound sequences can be used to take advantage of MB nonlinear behaviors and improve the contrast to blood vessels even more (***Stride E et al, et al 2003***, ***Cosgrove D et al, 2010, Wilson S and P Burns, 2010***). MB are injected in the blood and are routinely used to provide characterization and quantification of perfusion.

Analogy with optical microscopy

A rich analogy can be made between ultrasound imaging and optical microscopy. As both methods are fundamentally driven by the same wave equation, the phenomenon in both modalities have strong similarities. In particular, the resolution limit stands for optical imaging as resolution is indeed limited to the half wavelength limit. The conventional focused mode for ultrasound imaging has a lot in common with confocal microscopy whereas plane wave illumination is analog to full field microscopy. Both methods exhibit a tradeoff between image quality and scanning time. Finally, the use of contrast agents improves the contrast in both fluorescence microscopy and CEUS. More recently, Single Molecule Localization Microscopy showed the way to overcoming the diffraction limit in optical microscopy. Shortly after, this idea was implemented in ultrasound imaging. This technique is Ultrasound Localization Microscopy and is at the core of this thesis.

5. Ultrasound Localization Microscopy: a new mode in ultrasound imaging

Single Molecule Localization Microscopy

A turning point in biomedical imaging happened with the demonstration that the diffraction limit for spatial resolution could be overcome. The technique of Stimulated Emission Depletion (STED, ***Hell SW et al, 1994***), fluorescence Photoactivated Localization Microscopy (fPALM, ***Betzig E et al. 2006***), followed by Stochastic Optical Reconstruction Microscopy (STORM, ***Rust MJ et al. 2006***) showed that images could be formed beyond the diffraction limit. The fPALM technique, followed by other methods of Single Molecule Localization Microscopy (SMLM) relies on detection and sub-wavelength localization of individual sources. The signal of an isolated source can be determined which enables its localization with a precision not bound by the diffraction limit (*Figure 9.A*) but by the signal to noise ratio of the imaging system. This technique enabled the imaging of cell membranes with a resolution more than 10 times finer than the wavelength (*Figure 9.B*).

Instead of using classical fluorescent dyes, which are all excited at the same time and emit their photon simultaneously, a new generation of fluorophores was developed with a tunable probability of excitation. When illuminated, only a fraction of the sources are excited and emit their photons before being turned off so another set of sources can be excited. The probability of excitation and concentration of sources can be chosen to separate activated sources in each frame by several wavelengths. This enables sources to not interfere with their neighbors which allows their precise localization. The accumulation of hundreds of thousands of localizations through repeated activation, localization and bleaching of different sets of sources then allows the reconstruction of an image whose resolution is more than 10 times better than the classical resolution limit.

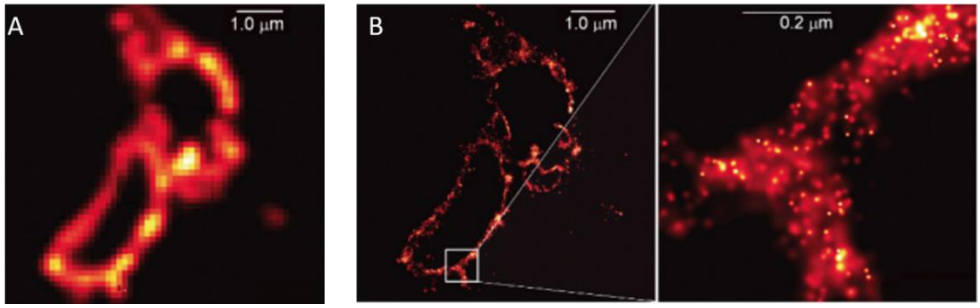

Figure 9: fluorescence Photoactivated Localization Microscopy

A. Total Internal Reflexion Fluorescence (TIRF) microscopy over a cell membrane, resolution of 200 nm. B. fPALM over the same cell membrane, localization precision of 2-25 nm (***Betzig E et al. 2006***).

Ultrasound Localization Microscopy

Earlier in this chapter, we saw that the formation of an image could be thought of as solving the inverse problem to determine the source field from the recorded pressure field. Directly solving the inverse problem would in theory be the best way to form the image. However, when imaging a complex medium, finding a stable solution for this problem is an issue because of the complexity of the problem and the noise level. For a medium composed of sparse punctual sources however, the problem is easier to solve and the position of the sources can be determined more accurately. The PSF is not exactly determined but approaching deconvolution can be done by approximating the position of the centroid of the source. This step is not limited by diffraction but by the signal to noise ratio and the methods to determine its centroid, which we will discuss in *Chapter 2*. The principle of Localization Microscopy is to introduce punctual sources in the media so as to have, at each moment, only isolated sources. Their centroid can then be localized with a precision finer than the diffraction limit and accumulated over time. This can be interpreted as a dilution of scatterers in time.

In optics, fluorophores are chemically linked to membranes and stochastically activated. In ultrasound, MB is injected in the blood circulation. The first proofs of concept (*Figure 10*) of Ultrasound Localization Microscopy (ULM) were performed in vitro (***Couture O. et al. 2011***, ***Dessailly Y et al. 2013, O'Reilly M et al. 2013, Viessmann O et al. 2013***), in hybrid in vivo models (***Christensen-Jeffries K et al. 2015***), before the first in vivo images could be performed in the rat brain (***Errico C et al. 2015***).

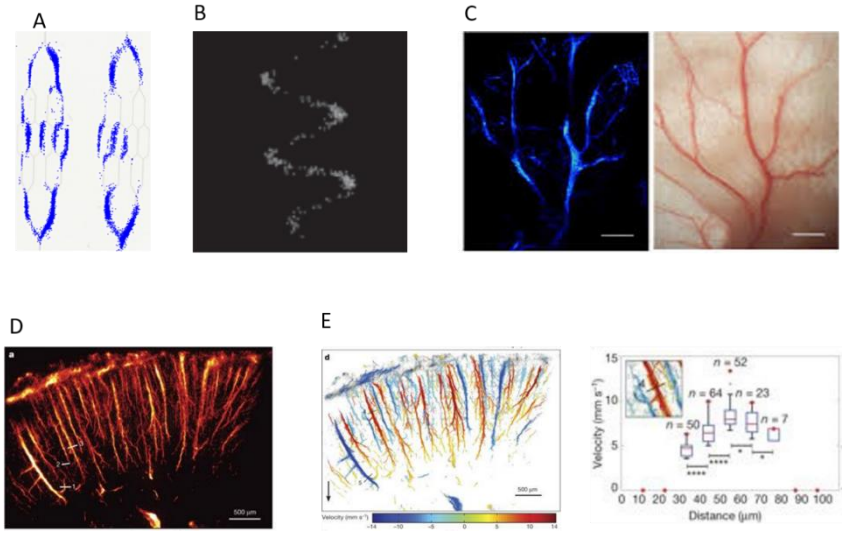

Figure 10: First Generation Ultrasound Localization Microscopy

A. ULM in a microfluidic chip (***Dessailly Y et al. 2013***). **B**. ULM through a piece of human skull (***O'Reilly M et al. 2013***). **C**. ULM in a mouse ear *(**Christensen-Jeffries K et al. 2015**). **D**.* ULM in the rat's brain cortical vasculature *(**Errico C et al. 2015**). **E**.* Velocity image *(**Errico C et al. 2015**).*

In the rat's brain, it was demonstrated that vessels as small as 8 µm could be imaged with a 100 µm wavelength. That is an improvement by more than a factor 10 in spatial resolution compared to conventional imaging. Moreover, because MB trajectories follow the blood stream, ultrafast imaging allows tracking of their velocities, and therefore precise quantification of blood velocity. In individual vessels, velocity profiles could be reconstructed, this was until then impossible in these conditions. It was also demonstrated through a human skull (***O'Reilly M et al. 2013***) which sparks great hope for future clinical applications. Especially, in the context of stroke, this may improve the sensitivity and resolution of transcranial Doppler and allow for an ultrasound based precise imaging of perfusion alteration. A factor 10 improvement in resolution could yield 100 µm resolution images with a 1 MHz transducer in humans, which would enable fine characterization of cerebral perfusion in healthy and pathological situations. However, as the resolution depends on the signal to noise ratio, reaching similar levels of performances through the skull will be challenging.

Drawbacks in Localization Microscopy

In optical Localization Microscopy, although the spatial resolution can be improved compared to conventional fluorescence microscopy, Single Molecule Localization Microscopy technique comes with a variety of drawbacks that are not often compatible with live cell imaging. Especially, it requires long exposures to high laser intensity, long acquisition times, chemical fixation of potentially toxic dyes, etc. A wide range of strategies now coexist in optical microscopy, like stochastic optical fluctuation imaging (SOFI), structured illumination microscopy (SIM), stimulated emission depletion (STED), etc. They all have different sets of resolutions, sensitivity, and biocompatibility and are used in various contexts (***Stockert J et al. 2017***). Similar considerations will have to be imagined for ULM. If the improvement in spatial resolution may be of great help in the characterization of fine vascular systems, the long acquisition times may not be adapted to other situations. Similarly to optics, imaging methods relying on fluctuation imaging or shaping the PSF may allow intermediate sets of resolution and penetration and offer a great versatility in vascular imaging in the future.

6. Objectives of the thesis

In the context of stroke, we think that ULM could change medical care for patients and improve the quality of translational research. However, ULM is a recent imaging modality invented by Olivier Couture, Mickael Tanter and Mathias Fink in 2010 (Patent/FR2011/052810), and still needs development and understanding prior to its translation, and its interest should be tested in animal models before any translation to human patients.

The first objective of my thesis is to improve the general knowledge on ULM as well as developing reliable tools for image formation. In particular, understanding the key aspects of data acquisition and reconstruction will be key for an efficient application in pathological animal models and translation to human patients. The development of a reliable and fast algorithm to form the images is also a crucial part of my work. These two objectives will be described in *Chapter 2* and are inspired by two articles I coauthored, a general review article on ULM (***Couture O et al 2018***) and a comparative of localization algorithms ***(Heiles B et al, In Prep***).

In order to properly use ULM, it is important to understand the extent and limitations of the technique, it is necessary to develop tools to quantify the spatial and temporal resolution as well as understand and model the fact that microvascular flow fundamentally drives image reconstruction. These will be described in *Chapter 3* and is inspired by a research paper I authored (***Hingot V et al 2019***).

In order to transfer ULM for clinical applications, long acquisition times will cause image quality to be affected by motion artefacts. A method for motion correction will be described in *Chapter 4* and is inspired by a research paper I authored (***Hingot V et al 2017***). In this chapter, I propose a more global method to correct most affine motions in 2D and discuss the efficiency of motion corrections strategies for ULM.

The translation of ULM to the context of stroke requires some fundamental studies to be made in preclinical models of ischemic stroke. In collaboration with a team of specialists of ischemic stroke, I applied 4D ultrasensitive Doppler and ULM to finely characterize the evolution of cerebral perfusion during a stroke and showed how early imaging methods can be predictors of outcome and response to treatments. This will be discussed in *Chapter 5* and is inspired by a research paper I authored and which is currently submitted (***Hingot V et al, Submitted***).

Finally, I was involved in other projects around the resolution limit in functional imaging and drug delivery. I will discuss these projects that are inspired by research articles I authored or coauthored (***Hingot V et al 2016, Teston E et al, 2018, Anfray A et al, 2019, Claron J et al, In Prep***) and discuss several unpublished results.

7. References

- Organisation mondiale de la santé. Global status report on noncommunicable diseases 2014: attaining the nine global noncommunicable diseases targets; a shared responsibility. (World Health Organization, 2014).
- Ministrère de la santé, des sports, de la jeunesse et de la vie associative. La prévention et la prise en charge des accidents vasculaires cérébraux en France : Rapport à la ministre de la santé et des sports. 2009.
- Cour des Comptes. L'Imagerie médicale, communication à la commission des affaires sociales du sénat. (2016).
- Société Française de Radiologie. Enquête sur les délais de rendez-vous pour un IRM en 2013. (2014).
- Saver Jeffrey L. Time Is Brain—Quantified. *Stroke* **37**, 263–266 (2006)
- Zivin, J. A., Fisher, M., DeGirolami, U., Hemenway, C. C. & Stashak, J. A. Tissue plasminogen activator reduces neurological damage after cerebral embolism. Science **230**, 1289–1292 (1985).

- Thiebaut, A. M. et al. The role of plasminogen activators in stroke treatment: fibrinolysis and beyond. The Lancet Neurology **17**, 1121–1132 (2018).
- Campbell, B. C. V. et al. Extending thrombolysis to 4·5–9 h and wake-up stroke using perfusion imaging: a systematic review and meta-analysis of individual patient data. The Lancet (2019). doi:10.1016/S0140-6736(19)31053-0
- Berkhemer, O. A. et al. A Randomized Trial of Intraarterial Treatment for Acute Ischemic Stroke. New England Journal of Medicine **372**, 11–20 (2015).
- Birenbaum, D., Bancroft, L. W. & Felsberg, G. J. Imaging in Acute Stroke. West J Emerg Med **12**, 67–76 (2011).
- Srinivasan, A., Goyal, M., Azri, F. A. & Lum, C. State-of-the-Art Imaging of Acute Stroke. RadioGraphics **26**, S75–S95 (2006).
- Wintermark Max et al. Comparative Overview of Brain Perfusion Imaging Techniques. Stroke **36**, e83–e99 (2005).
- Fassbender, K. *et al.* Streamlining of prehospital stroke management: the golden hour. *The Lancet Neurology* **12**, 585–596 (2013).
- Swiontkowski, M. F. Laser Doppler Flowmetry—Development and Clinical Application. *Iowa Orthop J* **11**, 119–126 (1991).
- Boas, D. A. & Dunn, A. K. Laser speckle contrast imaging in biomedical optics. *J Biomed Opt* **15**, (2010).
- Denk, W., Strickler, J. H. & Webb, W. W. Two-photon laser scanning fluorescence microscopy. *Science* **248**, 73–76 (1990).
- Tanter, M. & Fink, M. Ultrafast imaging in biomedical ultrasound. IEEE Transactions on Ultrasonics, Ferroelectrics, and Frequency Control **61**, 102–119 (2014).
- Deffieux, T., Demene, C., Pernot, M. & Tanter, M. Functional ultrasound neuroimaging: a review of the preclinical and clinical state of the art. Current Opinion in Neurobiology **50**, 128–135 (2018).
- Macé, E. et al. Functional ultrasound imaging of the brain. Nature Methods **8**, 662 (2011).
- Demené, C. et al. 4D microvascular imaging based on ultrafast Doppler tomography. NeuroImage **127**, 472–483 (2016).
- Tiran, E. et al. Transcranial Functional Ultrasound Imaging in Freely Moving Awake Mice and Anesthetized Young Rats without Contrast Agent. Ultrasound in Medicine & Biology **43**, 1679–1689 (2017).
- Demene, C. et al. Functional ultrasound imaging of brain activity in human newborns. Science Translational Medicine **9**, eaah6756 (2017).

- Imbault, M., Chauvet, D., Gennisson, J.-L., Capelle, L. & Tanter, M. Intraoperative Functional Ultrasound Imaging of Human Brain Activity. Scientific Reports **7**, 7304 (2017).
- Errico, C. et al. Ultrafast ultrasound localization microscopy for deep super-resolution vascular imaging. Nature **527**, 499–502 (2015).
- Couture, O., Hingot, V., Heiles, B., Muleki-Seya, P. & Tanter, M. Ultrasound Localization Microscopy and Super-Resolution: A State of the Art. IEEE Transactions on Ultrasonics, Ferroelectrics, and Frequency Control **65**, 1304–1320 (2018).
- Cobbold, R. S. C. Foundations of Biomedical Ultrasound. (Oxford University Press, 2007).
- Blanco, P. & Abdo-Cuza, A. Transcranial Doppler ultrasound in the ICU: it is not all sunshine and rainbows. *Crit Ultrasound J* **10**, (2018).
- Montaldo, G., Tanter, M., Bercoff, J., Benech, N. & Fink, M. Coherent plane-wave compounding for very high frame rate ultrasonography and transient elastography. *IEEE Transactions on Ultrasonics, Ferroelectrics, and Frequency Control* **56**, 489–506 (2009).
- Shung, K. K., Sigelmann, R. A. & Reid, J. M. Scattering of Ultrasound by Blood. *IEEE Transactions on Biomedical Engineering* **BME-23**, 460–467 (1976).
- Cloutier, G. & Qin, Z. Ultrasound backscattering from non-aggregating and aggregating erythrocytes—A review. *Biorheology* **34**, 443–470 (1997).
- Freimann, F. B. *et al.* MR elastography in a murine stroke model reveals correlation of macroscopic viscoelastic properties of the brain with neuronal density. *NMR in Biomedicine* **26**, 1534–1539 (2013).
- Martín, A. *et al.* Imaging of Perfusion, Angiogenesis, and Tissue Elasticity after Stroke. *J Cereb Blood Flow Metab* **32**, 1496–1507 (2012).
- Sakadžić, S., Lee, J., Boas, D. A. & Ayata, C. High-resolution in vivo optical imaging of stroke injury and repair. *Brain Res* **1623**, 174–192 (2015).
- Cao, R. *et al.* Photoacoustic microscopy reveals the hemodynamic basis of sphingosine 1-phosphate-induced neuroprotection against ischemic stroke. *Theranostics* **8**, 6111–6120 (2018).
- Wang, L. V. & Yao, J. A practical guide to photoacoustic tomography in the life sciences. *Nature Methods* **13**, 627–638 (2016).
- Hu, S. & Wang, L. V. Neurovascular Photoacoustic Tomography. *Front Neuroenergetics* **2**, (2010).
- Essig, M. *et al.* Perfusion MRI: The Five Most Frequently Asked Clinical Questions. *AJR Am J Roentgenol* **201**, (2013).
- Schrandt, C. J., Kazmi, S. M. S., Jones, T. A. & Dunn, A. K. Chronic monitoring of vascular progression after ischemic stroke using multiexposure speckle imaging and two-photon fluorescence microscopy. *J Cereb Blood Flow Metab* **35**, 933–942 (2015).

- Hingot, V. *et al.* Subwavelength far-field ultrasound drug-delivery. *Appl. Phys. Lett.* **109**, 194102 (2016).
- Heiles, B. *et al.* Ultrafast 3D Ultrasound Localization Microscopy using a 32×32 Matrix Array. *IEEE Transactions on Medical Imaging* 1–1 (2019). doi:10.1109/TMI.2018.2890358
- Blanco, P. & Abdo-Cuza, A. Transcranial Doppler ultrasound in the ICU: it is not all sunshine and rainbows. *Crit Ultrasound J* **10**, (2018).
- Provost, J. *et al.* 3D ultrafast ultrasound imagingin vivo. *Phys. Med. Biol.* **59**, L1–L13 (2014).
- Provost, J. *et al.* 3-D Ultrafast Doppler Imaging Applied to the Noninvasive and Quantitative Imaging of Blood Vessels in Vivo. *IEEE Trans Ultrason Ferroelectr Freq Control* **62**, 1467–1472 (2015).
- Hu, S. & Wang, L. V. Neurovascular Photoacoustic Tomography. *Front Neuroenergetics* **2**, (2010).
- Orset C *et al.* Mouse Model of In Situ Thromboembolic Stroke and Reperfusion. *Stroke* **38**, 2771–2778 (2007).
- Desal H.A. et al, Imagerie des AVC en urgence. */data/revues/01509861/00310004/327/*(2008).
- Silverman R.H. *et al*. The effect of transducer bandwidth on ultrasound image characteristics. *Retina* 15:37 – 42, 1995
- Tupholme G. E., "Generation of acoustic pulses by baffled plane pistons", *Mathematika*, vol. 16, pp. 209-224, 1969
- P. R. Stepanishen, "Transient radiation from pistons in an infinte planar baffle", *J. Acoust. Soc. Am.*, vol. 49, pp. 1629-1638, 1971
- J. A. Jensen, N. B. Svendsen, "Calculation of pressure fields from arbitrarily shaped apodized and excited ultrasound transducers", *IEEE Trans. Ultrason. Ferroelec. Freq. Contr.*, vol. 39, pp. 262-267, 1992
- J. A. Jensen, "Calculation of spatial impulse responses in ultrasound", *JASA*, 1997
- Gustav Mie, « *Beiträge zur Optik trüber Medien, speziell kolloidaler Metallösungen* », *Annalen der Physik, Leipzig*, vol. 25, 1908, p. 377–445
- Couture, O., Tanter, M., Fink, M. Patent /FR2011/052810.
- Adhi M, Duker JS. Optical coherence tomography--current and future applications. *Curr Opin Ophthalmol*. 2013;24(3):213–221. doi:10.1097/ICU.0b013e32835f8bf8
- Rinck PA (2008). *"A short history of magnetic resonance imaging"*. Spectroscopy Europe. **20** (1):
- Melroy, S.; Bauer, C.; McHugh, M.; Carden, G.; Stolin, A.; Majewski, S.; Brefczynski-Lewis, J.; Wuest, T. Development and Design of Next-Generation Head-Mounted Ambulatory Microdose Positron-Emission Tomography (AM-PET) System. *Sensors* **2017**, *17*, 1164.

Chapter 2: Maturation of Ultrasound Localization Microscopy

1. General considerations on Ultrasound Localization Microscopy

Maturing Ultrasound Localization Microscopy

As these techniques grew simultaneously in different groups across the world, the methods used for data acquisition and processing became fairly diverse. The first part of my work was to build on these proofs of concept and mature the technique. I investigated what are the key aspect of data acquisition and processing and wrote robust and effective processing algorithms with another Ph.D. student Baptiste Heiles. In parallel, several groups around the world brought new ideas to the field. I wrote this chapter with the intention to regroup recent progress in ULM, from me, my colleagues under the supervision of Olivier Couture, and other teams in the world. This chapter is organized into three parts. In the first section, I will discuss the different methods that have been used to perform ULM and their implication on image quality. I will also present the framework I developed for data acquisition and processing, justify the choice I made, and present the advances I brought to the field. A second part will discuss the different algorithms that we wrote and used for single microbubble localization, their performances and how they affect image quality. Eventually, several applications of ULM in various organs will be presented in the last section to give the reader an overview of how ULM can be used and how our imaging framework performs.

Although experiments are for the most part performed in animals, the preparation of the animal in itself isn't of particular interest for this work. The protocol for animal preparation and experiment is detailed in *Supplementary Material 1* together with the precise description of the image processing I used for the rat's brain. Briefly, animals were anesthetized and a catheter was placed in the jugular or tail vein for MB injection. For brain imaging in rats, the skull bone was removed.

Controlling microbubble injection

Unlike fluorescent proteins in optical Localization Microscopy, MB are physical objects, diluted in saline, and injected in the blood circulation. They are not equally distributed throughout the image and their refreshing rate is not driven by activation and deactivation but by blood flow. This is especially challenging to image small vessels where the blood flow is very low and MB passage rare. Moreover, they are eliminated from the body within minutes (***Schneider M et al 1999***). After adequate processing that will be discussed later, individual MB signals appear on beamformed images as spots that spread over a few half wavelengths. To ensure proper separation between MB, the dose needs to be small. However, a lower concentration means a lower rate of passage of MB in vessels, and longer acquisitions.

MB dose in intravenous injection in patients is recommended to be at most of 0.08 $ml.kg^{-1}$ although no harmful effect could be observed even at more than 50 times the recommended dose (***Bokor D et al. 2001***). In the rat brain (***Errico C et al 2015***), 0.3 $ml.kg^{-1}$ (150 μL) of MB were injected as a single bolus and almost no MB could be detected after 150 s. Injecting MB in a single bolus is simple but not necessarily adapted to ULM. Immediately after injection, the concentration is high and increases the chances to have MB signal overlap. From 30s on, MB are becoming rare and bring little supplementary information. In (***Hingot V et al. 2019***), I changed the injection pattern to maintain an appropriate and stable concentration throughout the whole acquisitions. A slow infusion of 0.8 $ml.kg^{-1}$ (400 μL) during 5 minutes stabilized MB concentration and 30 ± 5 MB were detected and in each frame.

Beamforming methods

Another specificity of ultrasound imaging compared to optics is the variety of ways to form images. In particular, conventional imaging in ultrasound is done through line by line scanning of the medium with focused beams. If this approach limits the frame rate to 50 -100 Hz, it provides better axial resolution and sensitivity than ultrafast plane wave imaging. Most proofs of concepts were done on conventional scanners with line by line scanning (***O'Reilly M et al. 2013, Viessmann O et al. 2013*** *and* ***Christensen-Jeffries K et al. 2015***). Moreover, most scanners available for clinical research use conventional imaging which enables a fast translation as no new equipment is required to pass a safety test. A clinical study is currently being performed in Germany, following preclinical results in tumors (***Opacic T et al. 2018***), and aims at providing fine characterization of the microvasculature in breast tumors.

In the beginning of ULM, only very few teams had access to programmable plane wave systems. However, compounded plane wave imaging seems to perform well for ULM (***Dessailly Y et al 2013, Errico C et al 2015, Dessailly Y et al 2017***). In all of these studies, the beamforming method was the Delay and Sum (DAS) that we described in *Chapter 1*. Since then, more advanced beamforming methods were introduced to fit special needs for ULM. A simultaneous multi-focus beamforming was proposed to simultaneously insonify two or more focal points with a single emission (***Espindola D et al. 2018***). This preserves the high frame rate while improving sensitivity to MB, especially far in depth. Another approach based on Minimum Variance beamforming showed clear improvement in lateral resolution and MB separability (***Diamantis K et al. 2019***). I didn't have time to adapt and compare these beamforming strategies but it make little doubt that it could largely improve the quality of images for in vivo acquisitions, especially in a situation with limited signal to noise ratio, in depth of through the skull bone.

Separating microbubbles from tissues

To be properly localized, a single MB signal has to be extracted from surrounding tissue echoes and noise. The behavior of MB, when insonified by ultrasound, is rich and provides different ways to discriminates them from tissues (***Stride E et al 2003***). The most effective method to extract MB's signal in daily clinical care relies on nonlinear properties of MB oscillations. At low pressures, MB oscillates in a simple compression mode. At higher pressures, nonlinearities appear and enrich the backscattered spectrum with harmonics. As incompressible tissues don't exhibit these nonlinear behaviors, the backscattered harmonics signals are purely due to MB. Multi pulses sequences like pulse inversion and amplitude modulation are standards nonlinear techniques in conventional imaging (***Cosgrove D et al, 2010, Wilson S et al, 2010***) and have been applied to plane-wave imaging (***Couture et al. 2009, 2012***). These methods have been used in ULM with conventional (***O'Reilly M et al. 2013, Viessmann O et al. 2013***) and plane wave imaging (***Foiret J et al, 2017***, ***Song P et al. 2018***). Although nonlinear imaging provides sensitive detection of MB, the intensity of harmonics suffers from low signal to noise ratio.

Spatio-temporal filters and in particular Singular Value Decomposition (SVD) filters (***Demene et al, 2015***) were able to surpass in some situations the sensitivity of nonlinear techniques for MB detection (***Dessailly Y et al 2017, Brown J et al. 2019***). A similar approach using Non Local Mean filtering (NLM) was also introduced (***Song P et al. 2018***). Unlike nonlinear techniques, spatio-temporal filters rely on MB motions to separate them from static tissues. For quasi static MB, they were shown not to perform as well as nonlinear techniques (***Brown J et al. 2019***). Moreover, MB behavior changes with the imaging central frequency. Nonlinear behaviors are especially strong close to their resonance frequency (2-4 MHz) and seem to outperform linear imaging in these conditions but not at higher frequencies (***Brown J et al. 2019***). Lastly, spatiotemporal performances are affected by tissue motions while nonlinear methods are more robust. Although registration methods can be effective to correct slow motions, as we will see in *Chapter 4*, the registration of fast motions remains challenging for MB separation.

The sensitivity of spatiotemporal filters depends mainly on the frame rate and number of frames. Data in ***Errico C et al*** (***2015***) and ***Hingot V et al.*** (***2019***), were acquired with two generations of Supersonic Aixplorer systems but using the same probe and the same acquisition parameters but different frame rates and number of frames. Both sets of frames were filtered with a combination of SVD and high pass Butterworth filters. In ***Errico C et al***, blocs of 200 compounded frames with 3 angles were acquired every second at 500 Hz whereas, in ***Hingot V et al***, I acquired blocs of 800 compounded frames with 3 angles every second at 1000 Hz. This improved the contrast between MB and remaining tissue signal after clutter filters and therefore enabled finer localization (*Figure 1*).

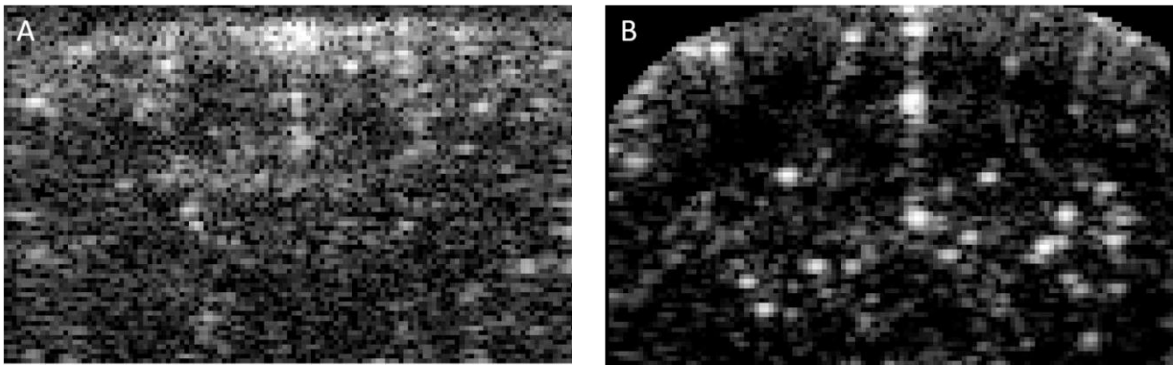

Figure 1: High frame rate improves the sensitivity of clutter filters in plane wave imaging

Two examples of MB contrast to tissue after 1s of acquisition displayed with a 30 dB range. A. After 200 compounded frames at 500 Hz as in (***Errico C et al. 2015***). B. After 800 compounded frames at 1000 Hz as in (***Hingot V et al. 2019***).

Density and Velocity image formation

In the first studies, ULM images were displayed as a scatter plot of points, or as a density map (***O'Reilly M et al. 2013, Viessmann O et al. 2013, Dessailly Y et al 2013***). A little later, approaches were proposed to track MB between frames (***Errico C et al. 2015***, ***Christensen-Jeffries K et al. 2015***). Both methods were adapted from the nearest neighbor search, which consists in pairing the closest MB in consecutive frames. However, it performed poorly in situations with close or crossing MB. Pairing objects is a classical assignment problem that has already been investigated thoroughly, and several open source codes would be found online. The one I found to work best relies on the script written by Jean-Yves Tivenez called *simpletracker*. It builds an interdistance matrix between MB in consecutive frames. The Hungarian method or Kuhn-Munkres algorithm is then used to solve this assignment problem using a set of operations on the rows and columns of the interdistance matrix. Unlike the nearest neighbor, it ensures that the total sum of distances is minimal and therefore provides a better assignation for close or crossing MB (*Figure 2)*.

I introduced its application to ULM (***Couture O et al. 2018***) shortly followed by others (***Song P et al. 2018***). For pairing MB in a very concentrated environment and with a low frame rate, another method has been proposed using a motion model (***Opacic T et al. 2018***). It assumes a linear motion for MB then calculates the a posteriori probability to belong to a track using Bayesians statistics. It looks to be efficient in high concentration/low frame rate setups but is very costly in computation time. It might be useful for ULM on conventional scanners with limited frame rates. Nonetheless, the tracking step will always benefit from higher frame rates which reduces the distances between two consecutive positions of MBs and therefore, simplify the assignment problem.

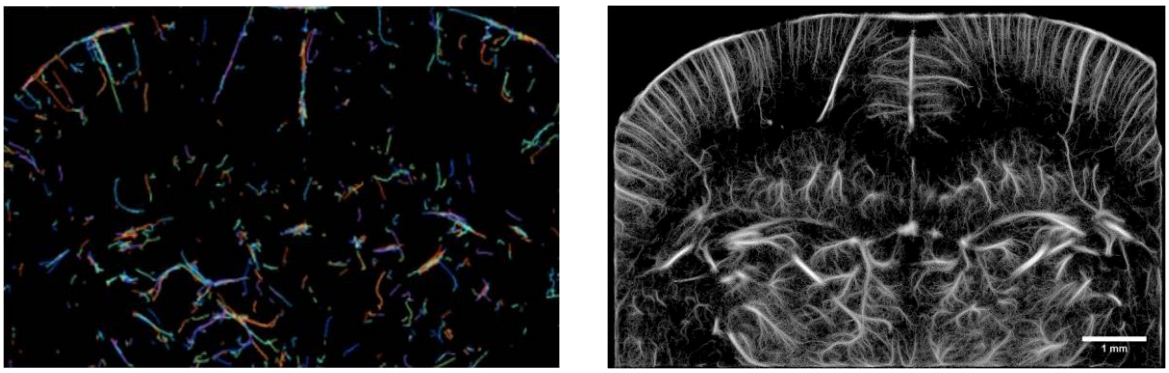

Figure 2: High frame rate improve sensitivity to MB for linear plane wave imaging

A. The Hungarian linker algorithm form tracks along MB courses, here on 800 frames. MB tracks are represented by lines of different colors. B. All MB tracks are summed to form a density image.

Overall, ULM can be summed up by the following *Figure 3*. A wide range of methods enable ULM to be performed in various conditions, at high and low frequency, either with linear or nonlinear imaging, conventional or plane wave imaging.

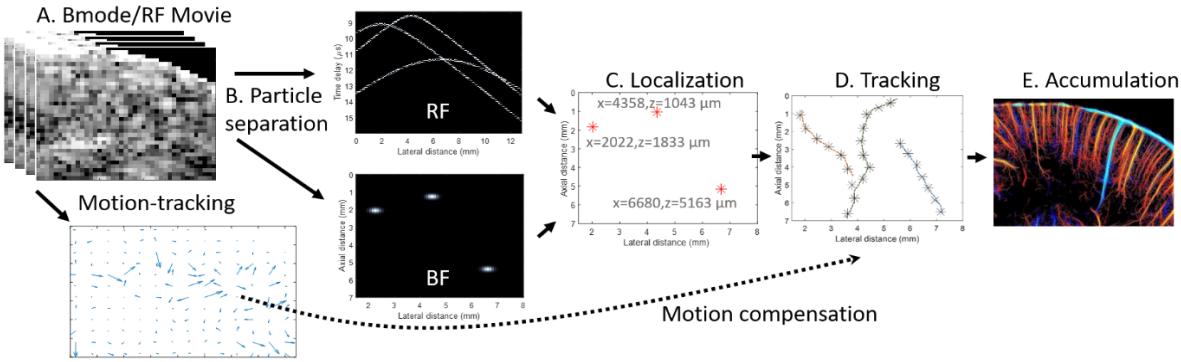

Figure 3: General framework for Ultrasound Localization Microscopy

A. Acquisition of either linear or harmonic beamformed or RF data. B. Particle separation for linear data, either as individual parabolas on RF data or PSF's on beamformed data. C. Localization step either through parabola fitting on RF data or through centroid localization of beamformed data. D. Nearest neighbor tracking step. E. Accumulation and image formation *(Couture O et al. 2018)*

Mean and instantaneous velocity for each track can be reconstructed through the tracking step. For each track, a value for the velocity is associated with each position. All MB tracks can be summed to form a mean velocity field. In the cortex of the brain, arteries are mostly going down and veins up (*Figure 4*). To have a sense of this organization, we chose a red colormap for negative axial velocities (going down) and blue for positive axial velocities (going up).

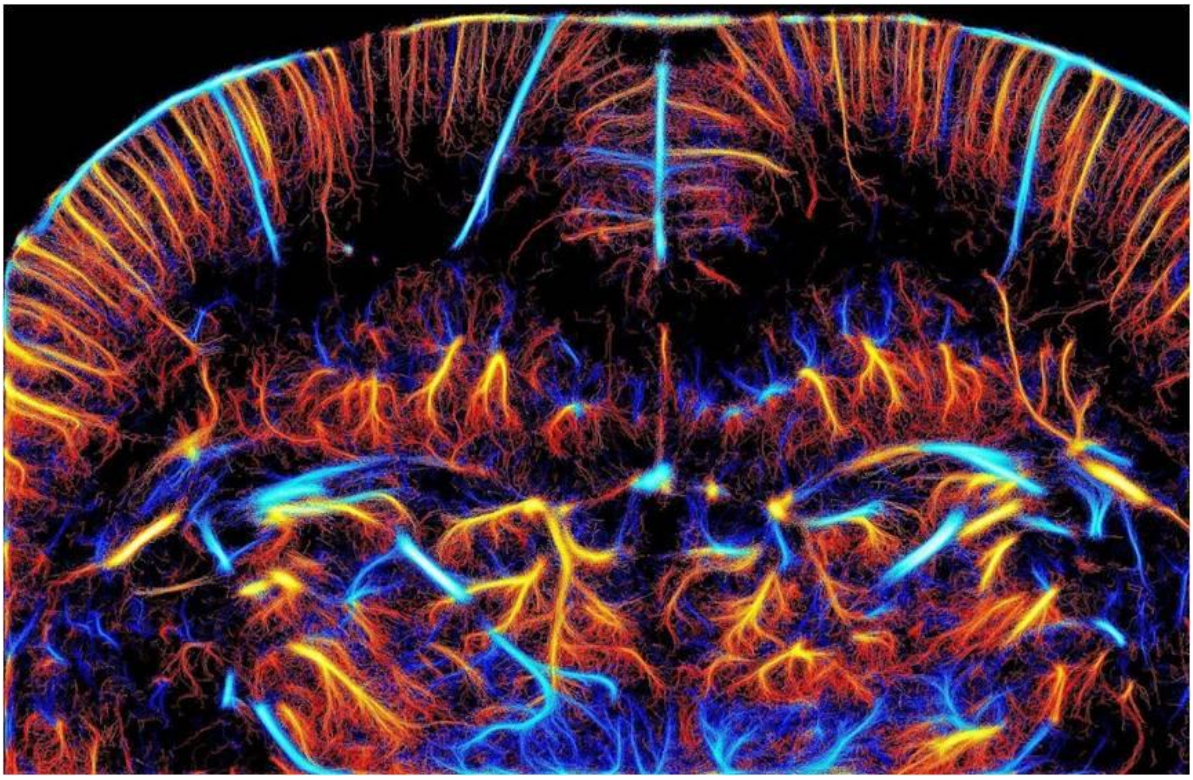

Figure 4: Ultrasound Localization Microscopy Velocity image (Couture O et al. 2018), cover for July 2018 edition of IEEE TUFFC.

2. Localization algorithms for Ultrasound Localization Microscopy

One crucial step in ULM is the determination of the MB positions. By definition, the image of a single MB is the PSF of the system, centered in the position of the MB. As for conventional image formation, the best method, in theory, would be the deconvolution but requires a precise knowledge of the effective of the PSF system. Effectively, approaching methods to localize the MB were therefore developed.

Historically, the first method used the non beamformed data (***Dessailly Y et al. 2013, Dessailly Y et al. 2015***). As we saw in *Chapter 1*, the echo backscattered by a punctual source appears as a parabolic delay law in the temporal received data. By fitting a parabola on the delay in the received temporal data, it is possible to estimate the position of the source using the delay equation. However, the signal to noise ratio on these data is often limited, and because parabolas spread across the transducer dimension, overlaps are common. Therefore, more precise localization methods were developed on beamformed data. Moreover, as beamformed data are similar to optical images, existing methods in fPALM for centroid localization can easily be adapted to ULM for MB centroid localization.

To localize MB on beamformed data, the most widely used techniques relies on the interpolation of images (***Couture O et al 2018***). This means constructing new data points, calculated from the existing image using a relation between new points and real points. Various interpolation schemes can be used, mainly polynomial interpolation using Lagrange polynoms, splines interpolations using piecewise polynomial interpolation, and Lanczos interpolation, using *sinc* functions as an interpolation kernel. The localization is performed as a local maximum search on the interpolated image. The performance of interpolation methods depend on the choice of the interpolation method. The most used are polynomial, spline and Lanczos interpolation. They are costly in terms of computation time as they increase the quantity of data. In particular, they are not adapted for 3D localization. Other methods exploited the shape of the PSF to estimate the localization of the centroid. Because the image of a single source is centered on the source, a simple idea is to measure the localization as a weighted average of the intensity in a vertical and a horizontal line with adapted weights. Algorithms based on radial symmetry were introduced in optics (***Parthasarathy R et al. 2012***) and proved to be most reliable as they use not only the axial and lateral symmetries of the PSF but the radial symmetry, using more information to perform the localization estimation.

To compare these algorithms, my colleagues Baptiste Heiles, Arthur Chavignon and I first simulated a dataset of beamformed images with moving punctual sources with similar level of contrast than in our dataset in the rat's brain. We used this dataset as a ground truth to test the performances of 6 algorithms: Bilinear, Cubic, Spline and Lanczos interpolation, weighted average and radial symmetry. Comparison with real positions of the simulated MB, we used classical metrics to estimate the performances of the algorithms. The Jaccard index is a measure of the detection abilities of the algorithms. The higher the Jaccard index, the better is the algorithm. Precision is another detection index corresponding to the proportion of detections that are actually MB. The localization error can also be estimated as the root mean square error between the true position and the detected positions. The choice of a non-adapted localization method will generate aliasing also called quantization error that has already been studied for interpolation and fitting schemes (***Song P et al 2018***). It is an artefact producing a gridding effect on the final images. To account for it, we estimated the relative height of the corresponding frequency content in the Fourier space to create an aliasing metric. Finally, the computation time of all the algorithm were measured and expressed as a function of the fastest, the weighted average. On our computer and with our implementation, it runs in 3 minutes. Among all the different methods, the more precise, more effective is the radial symmetry. It is almost as fast as the weighted average method but provide more precise data (*Figure 5*). Nonetheless, it still has a mean error around 10 μm.

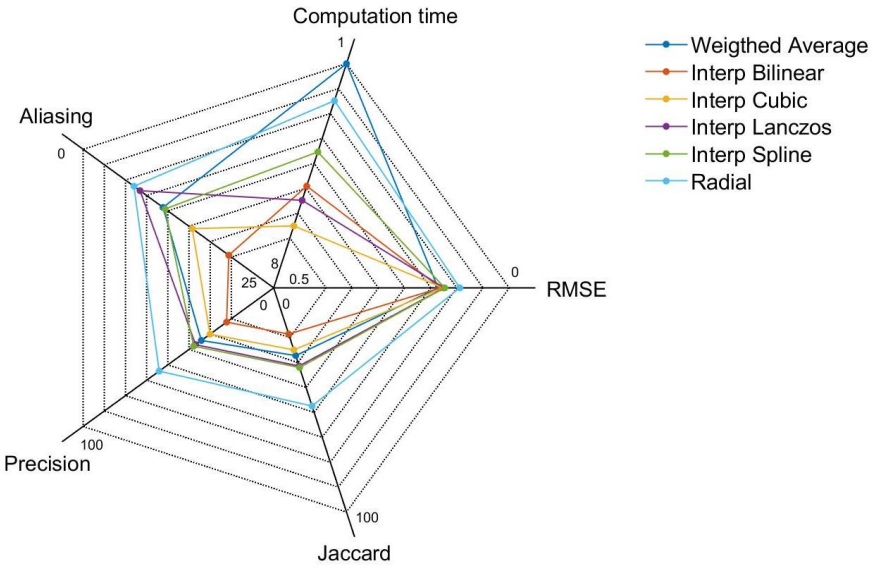

Figure 5: Radar chart comparing different localization algorithms

3. Applications

ULM reveals chaotic and tortuous organization in tumoral microvasculature

The main health related questions of the century are cancers, cardiovascular diseases, neuro-vascular diseases and diabetes (***WHO, 2014***). In all those pathologies, the microvasculature is deeply affected and people started investigating how ULM could improve characterization of the vasculature in various models. In particular, it was used to measure various metrics in tumor models to characterize the microvasculature, in 2D (***Opacic T et al. 2018***) and 3D (***Lin F et al. 2017***). I also performed ULM in tumors with our imaging systems and processing methods in an attempt to characterize the effect of ultrasound triggered drug delivery in mouse models (*Figure 7*). This will be discussed further in *Chapter 5*. All my images are displayed in full size in *Annex 2*.

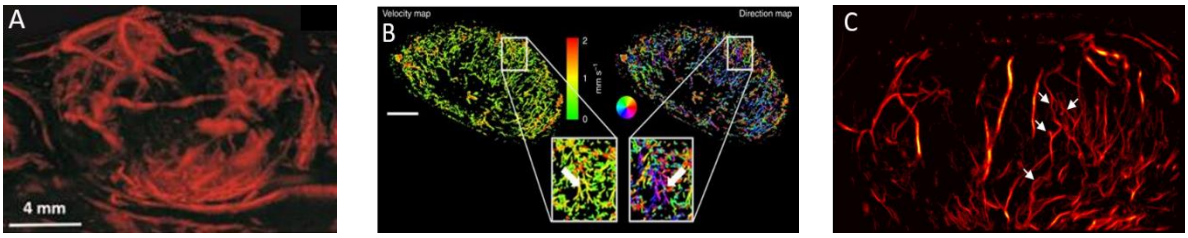

Figure 7: ULM enables microvascular imaging in sub-cutaneous tumors in mice

A. 3D scanning ULM in tumors (***Lin F et al. 2017***). **B**. Characterization of vascular parameters in different tumor models using ULM (***Opacic T et al. 2018***). **C**. ULM in a mouse tumor reveals chaotic architecture, micro aneurisms, tortuosity and by-passes (***Teston E et al, In prep***).

ULM reveals the repetitive organization of the kidney's cortex microvasculature

In patients with diabetes, the microvasculature is deeply impacted, in particular in the kidneys. ULM images of the kidney were made by other groups (***Foiret J et al 2017, Song P et al. 2018),*** and me *(**Couture O et al. 2018***) and showed the regular organization of the cortex of the kidney with a great level of details (*Figure 8*). To reconstruct these images, motion artefacts were present and therefore had to be corrected. The method for motion estimation and registration is discussed in *Chapter 4*.

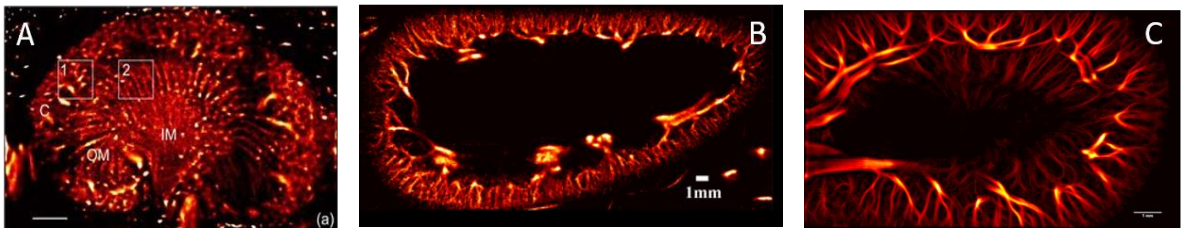

Figure 8: ULM in kidney's

A. ULM in a rabbit's kidney (***Foiret J et al 2017***). **B**. ULM in another rabbit's kidney (***Song P et al. 2018***). **C**. ULM in a rat's kidney (***Couture O et al. 2018)***.

ULM in the spinal cord reveal the organization and allows measurements of velocity

Imaging the spinal cord is also a major question in medicine as it is the gateway to the nervous system. In a study on spinal cord injury, a team used a deep learning method to perform ULM in a rat model of the injured spinal cord (*Figure 9.A*). In our team, Sophie Pezet and Julien Claron showed that spinal cord was also summited to vascular coupling induced by pain. To complete the study, we performed ULM in the spinal cord to describe the vascular organization and to measure the velocities where functional activation was observed (*Figure 9.B*). I will discuss these results further in *Chapter 6*.

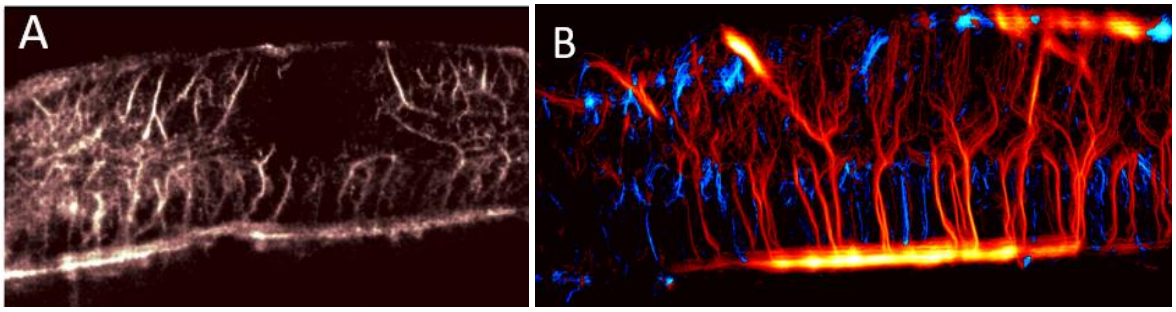

Figure 9: ULM in the spinal cord

A. ULM in a rat model of spinal cord injury (***Van Vloun RGJ et al. 2019)***. **B**. ULM to measure microvascular parameters for functional and anatomic exploration (***Claron J et al. In Prep***).

Evolutions of ULM in the Rat's brain

Finally, in the rat's brain (***Couture O et al. 2018, Hingot V et al. 2019***) advances in data acquisition and processing allow for an even finer mapping of the brain microvasculature compared to previous results (***Errico C et al. 2015***). These improvements are mainly due to better sampling of data and acquisition of more frames, steadier injections of MB and improvements in data processing algorithms and in particular the use of radial symmetry rather than interpolation methods (*Figure 10*).

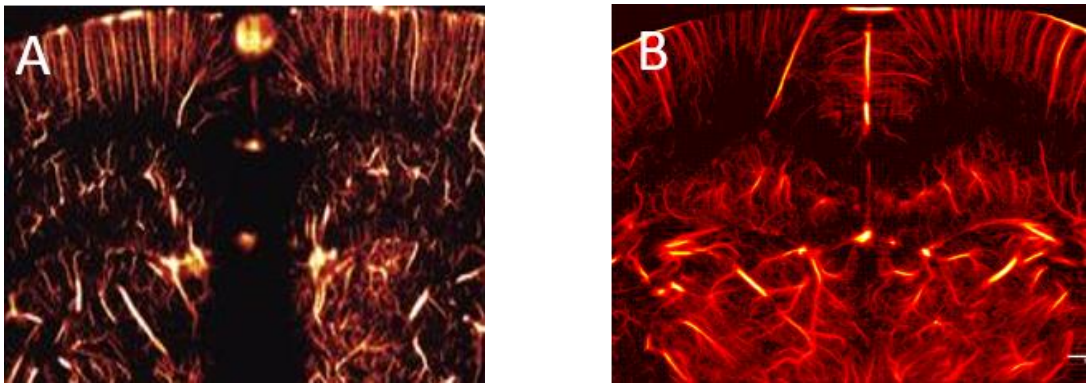

Figure 10: Evolution of ULM in the rat's brain

Similar colormap and crops for comparison of ULM in similar coronal planes over the rat's brain in similar physiological and display conditions. A. *Errico C et al. 2015*. B. *Hingot V et al. 2019.*

4. Conclusion

In this Chapter, we discussed the effect of several key parameters of ULM, mainly MB dose and injection pattern, frame rate, clutter filters and nonlinear imaging, beamforming, and MB tracking. If a high frame rate looks to improve the quality of imaging, the issue of MB separation to tissue remains an open question. At low imaging frequency, it might be more adapted to have nonlinear sequences whereas, at higher frequencies, spatio temporal clutter filter, and linear acquisition might be more performant. I would say that injecting MB in a steady manner is more appropriate for ULM although it might not be appropriate for all clinical situations. Finally, advanced beamforming strategies might eventually replace delay and sum as the standard beamforming technique for ULM as they can improve contrast, sensitivity and resolution for MB signals. Different localization algorithms were written and systematic comparison in both simulation and in vivo showed that the radial symmetry localization worked the best and in reasonable computing time. Nonetheless, a mean error of 10 μm was estimated as the best all algorithm could do in realistic in vivo conditions of contrast to noise ratio. The implication on the resolution of the technique will be discussed in *Chapter 3*.

Eventually, we developed a framework in animals based on a steady injection of MB, high frame rate imaging and high pass clutter filter, radial symmetry localization, Hungarian linker tracking, and density and velocity imaging. I demonstrated that it could be applied to produce images in various animal models, in tumors, kidney, spinal cord and brain. It shows the versatility of ULM and how it could be a useful tool in biomedical imaging. The detailed protocol in the rat's brain in available in *Annex 1*.

5. References

- Betzig, E. et al. Imaging intracellular fluorescent proteins at nanometer resolution. Science 313, 1642–1645 (2006).
- Stockert, J. C. & Blázquez-Castro, A. Fluorescence Microscopy in Life Sciences. (2017).
- Tanter, M. & Fink, M. Ultrafast imaging in biomedical ultrasound. IEEE Transactions on Ultrasonics, Ferroelectrics, and Frequency Control 61, 102–119 (2014).
- Couture, O., Fink, M. & Tanter, M. Ultrasound contrast plane wave imaging. IEEE Transactions on Ultrasonics, Ferroelectrics, and Frequency Control 59, 2676–2683 (2012).
- Desailly, Y., Couture, O., Fink, M. & Tanter, M. Sono-activated ultrasound localization microscopy. Appl. Phys. Lett. 103, 174107 (2013).
- O'Reilly, M. A. & Hynynen, K. A super-resolution ultrasound method for brain vascular mapping. Med Phys 40, 110701 (2013).
- Viessmann, O. M., Eckersley, R. J., Christensen-Jeffries, K., Tang, M. X. & Dunsby, C. Acoustic super-resolution with ultrasound and microbubbles. Phys Med Biol 58, 6447–6458 (2013).
- Christensen-Jeffries, K., Browning, R. J., Tang, M.-X., Dunsby, C. & Eckersley, R. J. In vivo acoustic super-resolution and super-resolved velocity mapping using microbubbles. IEEE Trans Med Imaging 34, 433–440 (2015).
- Errico, C. et al. Ultrafast ultrasound localization microscopy for deep super-resolution vascular imaging. Nature 527, 499–502 (2015).
- Opacic, T. et al. Motion model ultrasound localization microscopy for preclinical and clinical multiparametric tumor characterization. Nature Communications 9, 1527 (2018).
- Lin, F. et al. 3-D Ultrasound Localization Microscopy for Identifying Microvascular Morphology Features of Tumor Angiogenesis at a Resolution Beyond the Diffraction Limit of Conventional Ultrasound. Theranostics 7, 196–204 (2017).
- Foiret, J. et al. Ultrasound localization microscopy to image and assess microvasculature in a rat kidney. Scientific Reports 7, (2017).

- Song, P. et al. Improved Super-Resolution Ultrasound Microvessel Imaging with Spatiotemporal Nonlocal Means Filtering and Bipartite Graph-Based Microbubble Tracking. IEEE Trans Ultrason Ferroelectr Freq Control 65, 149–167 (2018).
- Couture, O., Hingot, V., Heiles, B., Muleki-Seya, P. & Tanter, M. Ultrasound Localization Microscopy and Super-Resolution: A State of the Art. IEEE Transactions on Ultrasonics, Ferroelectrics, and Frequency Control 65, 1304–1320 (2018).
- Hingot, V. *et al.* Microvascular flow dictates the compromise between spatial resolution and acquisition time in Ultrasound Localization Microscopy. *Scientific Reports* **9**, (2019).
- Bokor, D. *et al.* Clinical Safety of SonoVue™, a New Contrast Agent for Ultrasound Imaging, in Healthy Volunteers and in Patients with Chronic Obstructive Pulmonary Disease. *Investigative Radiology* **36**, 104 (2001).
- Stride, E. & Saffari, N. Microbubble ultrasound contrast agents: A review. Proceedings of the Institution of Mechanical Engineers, Part H: Journal of Engineering in Medicine 217, 429–447 (2003).
- Demené, C. et al. Spatiotemporal Clutter Filtering of Ultrafast Ultrasound Data Highly Increases Doppler and fUltrasound Sensitivity. IEEE Transactions on Medical Imaging 34, 2271–2285 (2015).
- Desailly, Y. *et al.* Contrast enhanced ultrasound by real-time spatiotemporal filtering of ultrafast images. *Physics in Medicine and Biology* **62**, 31–42 (2017).
- Brown, J. et al. Investigation of Microbubble Detection Methods for Super-Resolution Imaging of Microvasculature. IEEE Trans Ultrason Ferroelectr Freq Control 66, 676–691 (2019).
- Espíndola, D., Lin, F., Soulioti, D. E., Dayton, P. A. & Pinton, G. F. Adaptive Multifocus Beamforming for Contrast-Enhanced-Super-Resolution Ultrasound Imaging in Deep Tissue. IEEE Transactions on Ultrasonics, Ferroelectrics, and Frequency Control 65, 2255–2263 (2018).
- Diamantis, K. et al. Resolving Ultrasound Contrast Microbubbles Using Minimum Variance Beamforming. IEEE Transactions on Medical Imaging 38, 194–204 (2019).
- Soulioti, D. E., Espíndola, D., Dayton, P. A. & Pinton, G. Super resolution imaging through the human skull. arXiv:1811.10653 [cond-mat, physics:physics] (2018).
- Christensen-Jeffries, K. *et al.* Microbubble Axial Localization Errors in Ultrasound Super-Resolution Imaging. *IEEE Trans Ultrason Ferroelectr Freq Control* **64**, 1644–1654 (2017).
- Song, P., Manduca, A., Trzasko, J. D., Daigle, R. E. & Chen, S. On the Effects of Spatial Sampling Quantization in Super-Resolution Ultrasound Microvessel Imaging. *IEEE Transactions on Ultrasonics, Ferroelectrics, and Frequency Control* **65**, 2264–2276 (2018).
- Parthasarathy, R. Rapid, accurate particle tracking by calculation of radial symmetry centers. *Nature Methods* **9**, 724–726 (2012).

- Kuhn, H. W. The Hungarian Method for the Assignment Problem. in *50 Years of Integer Programming 1958-2008: From the Early Years to the State-of-the-Art* (eds. Jünger, M. et al.) 29–47 (Springer Berlin Heidelberg, 2010).
- Jean-Yves Tinevez (2019). simpletracker (https://www.github.com/tinevez/simpletracker), GitHub. Retrieved July 15, 2019.
- Ilovitsh, T., Ilovitsh, A., Foiret, J., Fite, B. Z. & Ferrara, K. W. Acoustical structured illumination for super-resolution ultrasound imaging. *Communications Biology* **1**, (2018).
- Bar-Zion, A., Tremblay-Darveau, C., Solomon, O., Adam, D. & Eldar, Y. C. Fast Vascular Ultrasound Imaging With Enhanced Spatial Resolution and Background Rejection. *IEEE Trans Med Imaging* **36**, 169–180 (2017).
- Sheeran, P. S. *et al.* Decafluorobutane as a phase-change contrast agent for low-energy extravascular ultrasonic imaging. *Ultrasound Med Biol* **37**, 1518–1530 (2011).
- Zhang, G. *et al.* Acoustic wave sparsely activated localization microscopy (AWSALM): Super-resolution ultrasound imaging using acoustic activation and deactivation of nanodroplets. *Appl. Phys. Lett.* **113**, 014101 (2018).
- Hingot, V. *et al.* Subwavelength far-field ultrasound drug-delivery. *Appl. Phys. Lett.* **109**, 194102 (2016).
- Provost, J. *et al.* 3D ultrafast ultrasound imagingin vivo. *Phys. Med. Biol.* **59**, L1–L13 (2014).
- Heiles, B. *et al.* Ultrafast 3D Ultrasound Localization Microscopy using a 32×32 Matrix Array. *IEEE Transactions on Medical Imaging* 1–1 (2019).
- Zhu, J. *et al.* 3D Super-Resolution US Imaging of Rabbit Lymph Node Vasculature in Vivo by Using Microbubbles. *Radiology* **291**, 642–650 (2019).
- M. Fink, “Ultrasound imaging,” Rev. Phys. Appl., vol. 18, no. 9, pp. 527–556, 1983.
- M. Fink, D. Cassereau, A. Derode, C. Prada, P. Roux, M. Tanter, J.-L. Thomas, and F. Wu, “Time-reversed acoustics,” Rep. Prog. Phys., vol. 63, no. 12, pp. 1933–1995, 2000.
- L. Sandrin, S. Catheline, M. Tanter, X. Hennequin, and M. Fink, “Time-resolved pulsed elastography with ultrafast ultrasonic imaging,” Ultrason. Imaging, vol. 21, no. 4, pp. 259–272, 1999.
- M. Tanter, J. Bercoff, L. Sandrin, and M. Fink, “Ultrafast compound imaging for 2-D motion vector estimation: Application to transient elastography,” IEEE Trans. Ultrason
- L. Sandrin, M. Tanter, S. Catheline, and M. Fink, “Shear modulus imaging with 2-D transient elastography,” IEEE Trans. Ultrason. Ferroelectr. Freq. Control, vol. 49, no. 4, pp. 426–435, 2002
- Schneider M (1999) Characteristics of SonoVue™. *Echocardiography* 16(s1):743–746. doi: 10.1111/j.1540-8175.1999.tb00144.x

- Cosgrove D & Lassau N, Imaging of perfusion using ultrasound, European Journal of Nuclear Medicine and Molecular Imaging August 2010, Volume 37, Supplement 1, pp 65–85
- Stephanie Wilson & Peter Burns, Microbubble enhanced US in body imaging: What role? Vol. 257, No. 1, 20
- Edwin Nemoto;Howard Yonas;Amin Kassam, Clinical experience with cerebral oximetry in stroke and cardiac arrest Critical Care Medicine. 28(4):1052–1054, APRIL 2000

Chapter 3: Characterization of spatial and temporal resolutions

1. Need for fine characterization of Ultrasound Localization Microscopy

The spatial resolution in conventional ultrasound is limited by the choice of the wavelength as we explained in *Chapter 1*. In conventional imaging, the temporal resolution is limited to about 50-100 Hz to let the probe scan over the whole image. In plane wave imaging, it can be increased to 20 kHz. To compensate for the loss in image quality, a set of tilted plane wave can be sent to form compounded images, reducing the frame rate depending on the desired efficiency of the synthetic focusing (***Montaldo G. et al. 2009***). The same limitation stands for conventional and ultrasensitive Doppler (***Bercoff J. et al. 2011***, ***Mace E et al 2013***). To overcome variability due to cardiac pulsatility, imaging is often performed over two cardiac cycles to make one Ultrasensitive Doppler image (***Demene C. et al. 2014, Demene C. et al. 2016***), which reduce the temporal resolution to the order of the second depending on the imaged subject. In these conditions, ultrasensitive Doppler has been shown to improve the sensitivity by a factor 30 compared to conventional pulsed Doppler (***Mace E et al 2013***).

The output data in ULM is not an image but a list of points. They can be represented as scatter plots of points (*Figure 1.A*) or tracks (*Figure 1.B*), or after projection on a grid, as a density image (*Figure 1.C, 1.E*), or a velocity vectorial field (*Figure 1.D*). Therefore, the Rayleigh criterion doesn't apply to define the spatial resolution. As MB flow in the vasculature, reconstruction is limited not only by the ultrasound system but by the physiology of the vasculature and MB concentration. The question of the minimum acquisition time to form an image has to be addressed. In this chapter, I will discuss definitions and estimations of spatial and temporal resolutions in ULM.

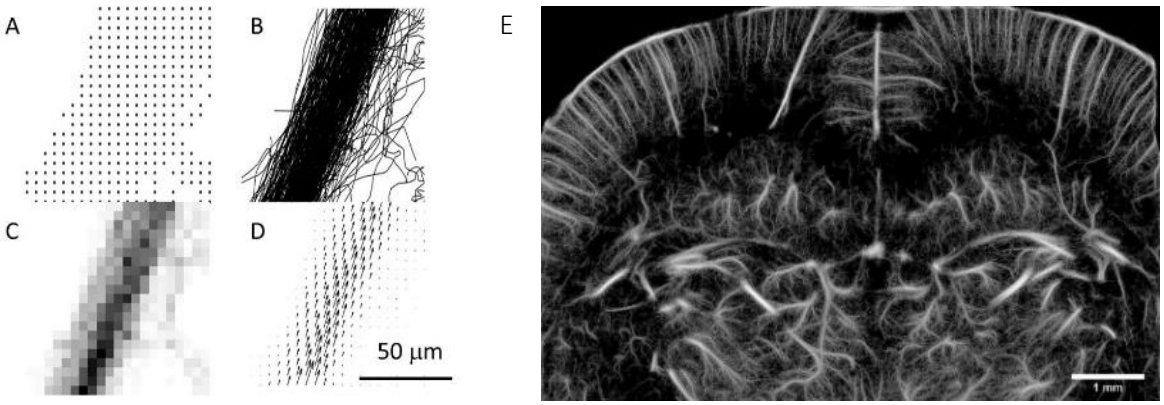

Figure 1: Data representation in ULM in the rat's brain

A. Scatter plot of points. **B**. Scatter plot of tracks. **C**. Density of MB's positions on a 5 µm grid. **D**. Mean vectorial velocity field on a µm grid size. **E**. Complete ULM in the rat's brain on a µm grid size

2. Spatial resolution in Ultrasound Localization Microscopy

Spatial resolution is not the precision of microbubble localization

When representing a density or velocity image, a grid size on which the data are represented have to be chosen. The choice of this grid will create an image with a pixel size that is an arbitrary choice, not a measure of the spatial resolution. The maximum theoretical precision for MB localization has been studied and a model was proposed (***Desailly Y et al. 2015***). This model estimates the variance on the time of arrival of the echo coming from a punctual source. This model claims that the maximum localization precision would be 5 μm for the rat's brain imaging conditions. However, MB localization in real data is necessarily less precise. Separation between MB and tissues is never perfect and localization is strongly affected by the contrast between MB signal and the remaining signal of tissue and noise. In *Chapter 2*, we saw that the localization precision also depends on the localization algorithm. A simulation study has been done to estimate the error made by various localization algorithms on a simulated dataset with similar conditions for MB signals than in the rat's brain experiment. The most performant localization algorithm had a mean localization error of 10 μm. This means that the resolution is at best 10 μm. The resolution is the minimum distance at which two structures can be separated. As no standard measure of resolution exist for Localization Microscopy data, an estimation can be done using the spatial frequency content in the dataset.

Fourier Shell Correlation as a spatial frequency criterion for image resolution

The Fourier Shell Correlation (FSC) is a measure of spatial frequency content classically used in optical localization microscopy that I adapted to ULM. First, the original dataset (*Figure 2.A*) has to be split in two. Before image reconstruction, tracks are listed in a cell structure by order of appearance and detection. The dataset is randomly split in two by selecting even and odd tracks. From there, two images are reconstructed from the two sub-datasets on a 5 μm grid (*Figure 2.B*). The cross correlation between the two images is calculated in the Fourier space (*Figure 2.C*). The value of the FSC (1) is calculated along a ring of radius r corresponding to iso-spatial frequency lines (*Figure 2.D*). It can be calculated using the Fourier transform of the two sub images F_1 & F_2. The FSC curve is plotted for continuous values of r.

$$FSC(r) = \frac{\sum_{shell} F_1(r_i) F_2(r_i)^*}{\sqrt{\sum_{shell} |F_1(r_i)|^2 \sum_{shell} |F_2(r_i)|^2}} \quad (1)$$

This curve usually display a slow decay before dropping drastically when the frequencies are no longer consequential in the dataset (*Figure 2.E*). The measure of the spatial resolution is usually done using a threshold at 0.5 and give 10 μm in the rat's brain. However, the choice of the 0.5 threshold is arbitrary and the 10 μm value not a definitive measure of resolution but an indication of the finest structures that are coherent in the dataset.

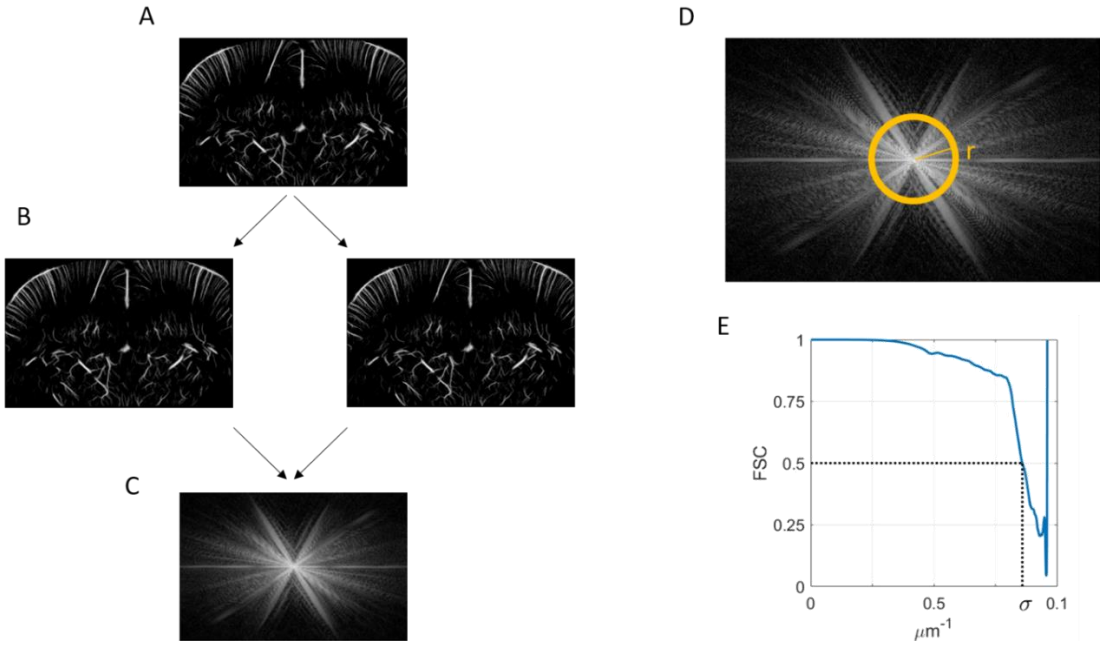

Figure 2: Fourier Shell Correlation for spatial resolution estimation

A. Original dataset. B. Separation in two sub-dataset and formation of two images. C. Cross correlation spectrum. D. Integration over a ring. E. Evolution of the FSC for increasing value of spatial frequencies. Determination of the spatial resolution at the 0.5 threshold.

ULM requires both spatial and temporal characterization

In the case of the rat's brain, the FSC criteria indicates that information is reliable until 10 μm. Still, it doesn't a priori mean that all vessels are accurately reconstructed with a 10 μm precision. More than that, we know the localization done by the algorithms is also estimated to be 10 μm. But those two information describe two different phenomena. The localization error describes the smoothing induced by the processing step. It is a mean error and cover various situations. For close MB (in big vessels), the error is large whereas for single MB (in smaller vessels), the error is reduced. The FSC describes the spatial frequency limit at which information is still relevant but relies on an arbitrary threshold. None of these two values can be used as a definitive measure of the resolution but as both are of around 10 μm, it gives an idea of the structures that can accurately be imaged in ULM.

The issue of spatial resolution, together with the precision of the localization algorithm will be adapted in a research article that is currently in preparation (***Heiles et al, In Prep***). Moreover, all vessels don't have the same probability to be explored by MB and in ULM, the spatial resolution alone isn't enough to characterize the image quality. A complete characterization relies on the duality between spatial and acquisition time. To complete the measure of temporal resolution, I introduced a method to characterize image completion together with a simple blood flow model. The following section is adapted from a research article I wrote (***Hingot et al, 2019***).

3. Temporal resolution in Ultrasound Localization Microscopy

Microvascular flow drives microbubble passage in vessels

Blood flow in the microvasculature displays various complex behaviors (***Herman I. 2016***), mainly pulsatility in small arteries (≈ 1 mm in diameter), the contractility of lean muscles in the arterioles (20-200 μm), and rheology in capillaries (a few μm). However, blood flow in most vessels Q follows an overall Poiseuille law (2) with L corresponding to vessel's length, η to the blood viscosity and $\Delta\mathrm{P}$ to the continuous pressure drop between small arteries (90mmHg) and big veins (10mmHg). The most important parameter, however, is the diameter d as suggested by the exponent 4. ULM can accurately measure vessels' sizes and average velocities but lacks dynamic information on pulsatility, contractility, and rheology. A reductionist approach using only measurable ULM parameters is to set vessel's diameter as the main variable even though it misses a lot of hemodynamics effects and poorly describes blood flow.

$$Q = \frac{\pi d^4}{128\eta}\frac{\Delta \mathrm{P}}{L} \sim Q(d) \quad (2)$$

Because MB are smaller than red blood cells (1-5 μm), we hypothesize that they are evenly distributed in the blood circulation. Therefore, the average MB number *N* crossing a section of a vessel of diameter d after time T_{acq} while having a general vascular concentration C_{MB} is given by equation (3).

$$N = Q(d) * C_{MB} * T_{acq} \quad (3)$$

In most vessels, blood flows mainly in only one preferential direction. Continuous imaging with high frame rates allows accurate tracking of MB for several tens of milliseconds. Therefore, a continuous trace can be reconstructed from one individual MB and not a single point reducing the dimensionality of the problem by an order of magnitude.

The number of pixels N necessary to reconstruct a vessel of diameter d with pixels of size l_{pix} is given by equation (4).

$$N = \frac{d}{l_{pix}} \quad (4)$$

Therefore, considering than the reconstruction of a single vessel requires to reach at least one MB detection per pixel leads to the equality between equations (3) and (4). The resulting equation (5) determines the minimum acquisition time T_{rec} needed to reconstruct a vessel of diameter d with a pixel size l_{pix} and a vascular concentration of MB C_{MB}.

$$T_{rec}(d) = \frac{1}{\frac{Q(d)}{d} C_{MB} l_{pix}} \quad (5)$$

I used the rat's brain as a model of vasculature as it offers a large and multiscale distribution of vessels and kept the vascular MB concentration constant. I introduce a general approach to study the influence of acquisition time of the pixel size that can be used to reconstruct the image. I then use a local approach to explain how the acquisition time affects the reconstruction of vessels according to their size. I finally describe the effect of acquisition time on the determination of velocity profiles.

Global approach: Influence of acquisition time on the reconstruction pixel size

To study the tradeoff between spatial and temporal resolution, we reconstructed images with different pixel sizes (between 5 µm and 100 µm) and after different accumulation times (between 1 s and 240 s). Reconstructed pixels were saturated after the accumulation of a single MB to make binary images as shown in *Figure 3.A*. Saturation curves in *Figure 3.B* show the temporal behavior of image reconstruction. After a rapid increase phase, the reconstruction slows down as MB are filling the microvascular bed. If for the images with 100 µm pixels the saturation curve reached a plateau within the time of the experiment, the corresponding 5 µm pixel image did not reach saturation. However, we postulate that a reasonable image quality is reached at 90 % of final saturation, with a good sampling of micro vessels being displayed in the image. From the saturation curve with 100 µm pixels, which is fully saturated, we see that 90% saturation is reached after about 3 times the characteristic time. We extrapolate this behavior to estimate a reconstruction time as 3 times the characteristic time. Consequently, an image with 100 µm pixels would be reconstructed within 10 s. This time increases to 60 s for 20 µm pixels and gets close to 4 minutes for 5 µm pixels. Overall, *Figure 3.C* shows how the reconstruction time behaves as an inverse function of pixel size.

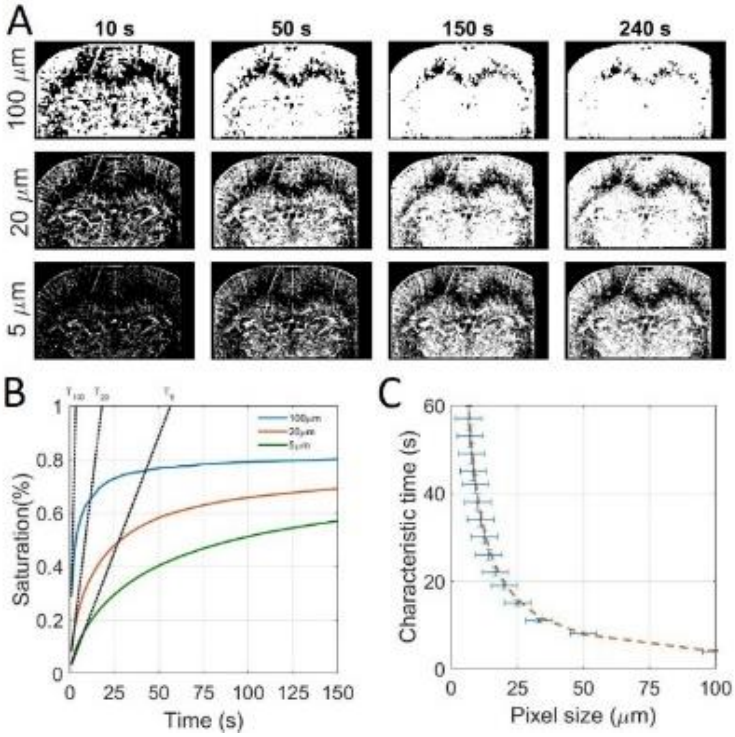

Figure 3: Global approach shows that acquisition time is inversely proportional to pixel size

Global approach using whole image saturation and determination of the influence of the acquisition time on reconstruction pixel size. **A**. Saturated Images for different pixel sizes and after different acquisition times. **B**. Corresponding saturating curves with the tangent at origin intersecting the 100% saturation line to determine the saturation time. **C**. Experimental time constants as a function of the pixel size and inverse fit $y = p_1 \frac{1}{x}$ with p_1=384s. µm^{-1}, R^2=0.99.

Local approach: Influence of acquisition time on the vessel reconstruction

However, this approach only gives general information on image reconstruction and misses the fact that the smallest vessels are the one that take a long time. Indeed, MB supply should decrease as vessels get smaller and the flow rate decreases. To highlight the time for reconstruction of single vessels, we isolated 150 vessels with sizes between 5 µm and 100 µm (*Figure 4.A*). It is important to note that a 5 µm is not properly a 5 µm vessel but a single track formed by one MB. On a 5 µm grid, this creates a 5 µm line but it doesn't imply that the surrounding vessels is indeed 5 µm. For each vessel, we counted the total number of MB passing through a given cross section in time (*Figure 4.B*). Typically, a vessel of 100 µm sees a dozen MB every second whereas a vessel of 20 µm only sees one MB every 10 s. For smaller vessels, we expect to see at most one MB during the 4 minutes of the course of the experiment. For different sizes of vessels, we see that the passage of MB in the vessels is overall linear with time, which is consistent given that the vascular concentration of MB is constant.

The flow rate's behavior with the vessel sizes can be estimated by plotting the total number of MB detected in 240 s through the cross sections as a function of the vessels diameters (*Figure 4.C*). The log-log plot exhibits a global power law for the MB flow with the diameter. The exponent 3.7 is slightly lower than 4 which would theoretically be the Poiseuille power law (2). On the same vessels, we can report the mean velocity as a function of the diameter (*Figure 4.D*). In this case, the log-log plot shows an overall power law with an exponent close to 2 which would once again correspond to the perfect Poiseuille power law. In *Figure 4.C* and *Figure 4.D*, the trends follow the model we defined but with poor determination coefficients. This confirms that choosing the diameter as the determinant is relevant for a first order estimation but hides a lot of finer effects and is not a good model for blood flow like the effects of pulsatility, contractility and rheology.

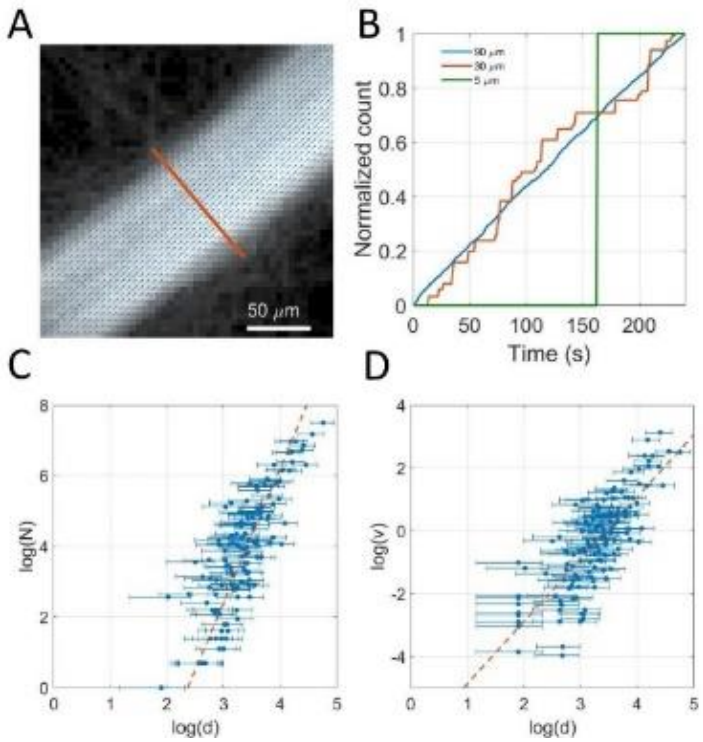

Figure 4: Ultrasound Localization Microscopy allows fine microvascular measurements

Local approach using 150 individualized vessels. **A**. Example of a selected vessel's section superimposed on density image with velocity field. **B**. Example of time dependency of microbubbles count in three vessels of 80 µm, 20 µm and 5 µm. **C**. Dependency of the bubble rate with vessel's diameter measured on a 150 vessels sample, fit $y = p_1 x + p_2$ with p_1 = 3.7, p_2 = −8.2, R^2 = 0.70. **D**. Dependency of maximum velocity with vessel's diameter measured on a 150 vessels sample fit $y = p_1 x + p_2$ with p_1 = 1.9, p_2 = −6, R^2 = 0.60.

To investigate the link between acquisition time and vessel diameter in (5), we introduce the variable h defined in (6) that can be calculated with d and $N(d)$. Therefore, we can represent the influence of the diameter using only h. Effectively, h can be calculated as $(6')$ using (3) for every individual vessel.

$$h(d) = \frac{Q(d)}{d} C_{MB} \quad (6) \qquad \& \qquad h(d) = \frac{N(d)}{dT_{acq}} \quad (6')$$

The saturation curves in *Figure 5.A* captures the time necessary for different vessels to be completely reconstructed (e.g. saturation reaches 100%). For every vessel, the reconstruction time T_{rec} is measured as the time it takes until all the pixels of the section are reconstructed. Using h, the expression of the acquisition time in (5) can then be simplified in (7).

$$T_{rec}(d) = \frac{1}{h(d).\, l_{pix}} \quad (7)$$

For all vessels, T_{rec} and h are calculated and are displayed in *Figure 5.B*. Equivalence between h and the underlying vessel diameter is displayed on the top axis for more clarity.

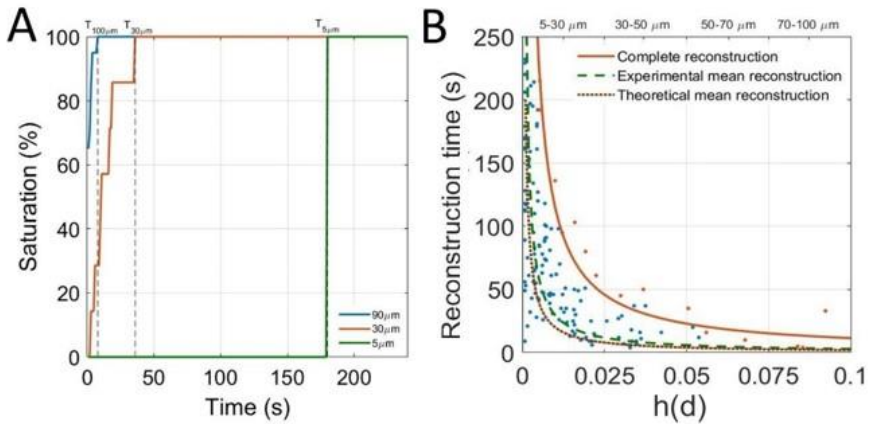

Figure 5: Local approach shows that acquisition time decreases with vessel size

Determination of the influence of the acquisition time on vessel reconstruction. **A**. Determination of reconstruction times for vessels of $90\mu m$, $30\mu m$ and $5\mu m$. **B**. Scatter plot of saturation times of vessels by size. Complete reconstruction curve (orange line) $y = p_1 \frac{1}{x}$ with p_1=1.14 µm^{-1}, R^2=0.97, Experimental mean reconstruction curve (green dashed line) $y = p_1 \frac{1}{x}$ with p_1=0.29 µm^{-1}, R^2=0.72. Theoretical mean reconstruction curve (brown dashed line) $y = p_1 \frac{1}{x}$with p_1=0.2 µm^{-1}.

The experimental mean reconstruction curve (dashed green line) is determined through an inverse linear regression on these points and represents the average reconstruction time for a given size of vessels. The model equation (7) is used to predict a theoretical mean reconstruction curve (dashed brown line) which seems to be in accordance with the experimental mean reconstruction curve. A family of vessels is reconstructed when all corresponding vessels are reconstructed. The time to reconstruct a family of vessels is limited by vessels with the slowest reconstruction (singled out in orange). Inverse fitting on these points form the complete reconstruction curve (orange line) that set the time for vessels of a given size to be reconstructed. According to these results, 70 μm vessels would be reconstructed in 30 s, 30 μm vessels in 1 min and 10 μm vessels in 5 minutes. For smaller vessels however, it is not clear whether they are explored at all by MB or if the transit time is just too long for MB to pass within a reasonable time frame. In any case, as the localization precision is around 10 μm, it is unclear how ULM actually perform at these microscopic scales.

Local quantifications of blood flow to estimate MB vascular concentration

Further quantification can be done using two different ways to estimate blood flows. A mesoscopic approach consists in counting MB passing through a given cross section and relate it to blood flow (8). A microscopic approach consists in measuring microbubbles velocities and the vessel diameter. The flow can then be estimated using the average velocity (8′).

$$Q(d) = \frac{N(d)}{C_{MB} T_{acq}} \quad (8) \qquad \& \qquad Q(d) = v_{mean}(d)\pi d^2 \quad (8')$$

Using the two estimations of the blood flow (8) & (8′) we can average these measures on the 150 vessels individually segmented and estimate the actual concentration in the blood (9).

$$C_{MB} = mean\left(\frac{N(d)}{v(d)\pi d^2 T_{acq}}\right) \sim 2.10^5\ MB.ml^{-1} \quad (9)$$

Considering an injected dose of 400 μL of a MB solution concentrated at 10^8 MB.ml^{-1}, in around 40 ml of the rat's blood, if injected in one bolus, we should expect an initial concentration of 10^6 MB.ml^{-1}. However, since we injected in a continuous fashion, this doesn't allow proper comparison. We can, however, the value of 2.10^5 MB.ml^{-1} is far from absurd as we diluted the total dose over 5 minutes. The quantification of MB concentration would be very hard to estimate using other methods and might help a better quantification of perfusion estimations.

Influence of acquisition time on the reconstruction of velocity profiles

If the detection of one MB is a necessary condition to reconstruct a pixel, it might not be sufficient to have a good contrast or to estimate velocities. Indeed, because of the absence of elevation resolution, all the MB passing through a vessel can have different velocities inside a vessel because of their position in elevation and the orientation of the vessel. Therefore, averaging over several MB is needed to converge on an underestimated but stable velocity profile. It can be showed that the normal projection of a cylindrical in a 2D plane result in another parabolic profile but underestimated by a factor 2/3. Moreover, the velocity of a vessel that does not flow within the imaging plane will also be underestimated. Therefore, when measuring velocities in 2D ULM, there should always be an uncertainty on the actual velocity as it is in most cases underestimated. In all cases, 3D ULM will allow real measurements of velocities as no projection will be performed in elevation and MB would be tracked in all directions which would allow velocity estimation in all three dimensions.

Nevertheless, as we increase the dimensionality, we foresee that the acquisition time will also be increased compared with a single coronal plane reconstruction. It is fair to say however that it will be considerably faster than repeating 2D scans to reach the same level of resolution. We can adapt equation (4) in $(4')$ and adapt (5) to determine the acquisition time $(5')$ for a 3D ULM acquisition.

$$N_{3D} = \frac{d^2}{{l_{pix}}^2} \quad (4') \qquad \& \qquad T_{acq,3D} = \frac{1}{\frac{Q(d)}{d^2} C_{bubbles} {l_{pix}}^2} \quad (5')$$

To estimate the time required to reach a stable velocity profile in a vessel, we measured a velocity profile along the cross sections of the vessels we segmented (*Figure 6.A*). The correlation between the profiles reconstructed after different times with the profile obtained at the end of the total acquisition time provides a measure of how fast the profiles are reconstructed (*Figure 6.B*). The reconstruction time is set as the time to reach a correlation of 0.9. Similarly to *Figure 5.B*, the reconstruction times for the 150 vessels are reported as the blue points on the scatter plot in *Figure 6.C*. In *Figure 6.C* the slowest vessel to reconstruct are singled out (orange points) and the complete reconstruction curve (orange line) was calculated with an inverse fit. The two inverse laws for complete reconstructions exhibit a factor 4 meaning that for a given size of vessel, it would take 4 times longer to reach a stable velocity profile than it takes to reconstruct the vessel. However, this might not be true in the smallest vessels in which the velocity does not vary so much between the sides and center of the vessel. In the smallest vessels, the question of how well does MB velocity represent blood velocity is also not a trivial question and will merit to be answered in the future.

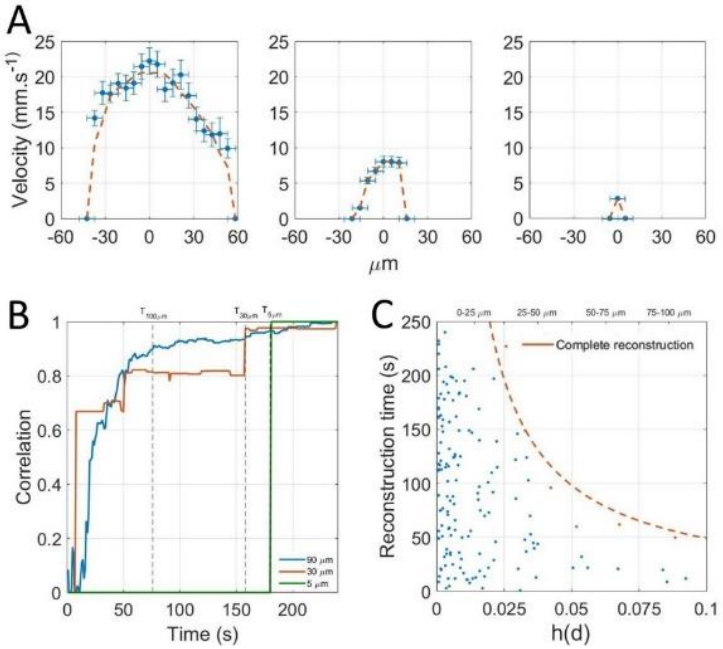

Figure 6: Local approach shows that acquisition time are even longer for velocity estimates

Determination of the influence of the acquisition time on velocity profiles reconstruction. **A**. Velocity profiles for three vessels of $100\mu m$, $30\mu m$ and $5\mu m$. **B**. Correlation with complete profile to determine reconstruction time. **C**. Scatter plot of reconstruction times of vessels by size. Complete reconstruction curve (orange line) $y = p_1 \frac{1}{x}$ with p_1 =4.9 μm^{-1}, R^2=0.96.

Discussion on the temporal resolution

As it stands, ULM could provide images of the complete capillary network with a10 µm accuracy in about 5 minutes with total or partial removal of the skull. We show that larger vessels of 100 µm are fully reconstructed within tens of seconds, but that detecting all the smallest vessels, would take minutes to tens of minutes for the smallest capillaries. The reconstruction of velocity profiles can take up to 4 times longer as compared to the MB distribution mapping since it requires a greater number of MB tracks. Compared to other existing techniques used to image the microvasculature, ULM offers a different set of advantages and drawbacks. For preclinical and clinical study of the vasculature, in depth imaging is only possible with a spatial resolution up to 100 µm with contrast MRI (*Lin C-Y et al. 2009*) or with ultrafast Doppler (*Bercoff J et al. 2009*) although higher frequency probes may allow imaging with finer resolution. Using two photon microscopy, imaging of vessels can be done through a cranial window with a resolution below 1 µm but with a depth limited to under a millimeter *(Svoboda K et al. 2006).* ULM provides a compromise between optical microscopy and in depth imaging methods at the cost of several minutes of temporal resolution. As velocities can be measured, it may be used as a quantitative tool to measure blood flow in depth and at the scale of individual vessels.

In both cases, the model we introduced can be helpful to design ULM acquisitions. We foresee that ULM could be a relevant imaging modality in two main situations. First, ULM is a unique imaging modality to study the microvasculature. We showed that in this situation, acquisition time is limited by low blood flow in the smallest vessels even with high microbubble concentrations. In this study, with a steady microbubbles infusion of 0.8 $ml.kg^{-1}$ we expect complete capillary reconstruction in about ten minutes. With microbubbles concentrations within clinical recommendations, we expect the reconstruction time to be longer by roughly an order of magnitude. However, the clinical safety of SonoVue microbubbles has been evaluated for doses between 0.003 and 0.12 $ml.kg^{-1}$ *(**Bianconi E et al. 2013***) and concluded that even high doses of microbubbles appeared safe and well tolerated by patients. Therefore, it could be possible to increase microbubble dose to reduce reconstruction time, but it could only be increased to the point where microbubbles stop being individualized. This comes as a fundamental limit for capillary imaging where the acquisition time is necessarily of several minutes.

Secondly, ULM would be relevant to image sub-millimeter vessels but deep into organs or through the skull. In bigger vessels, for MB to be individualized, the concentration should be lowered, eventually extending the acquisition time. Thus, even with a lower emphasize on capillary structures and low blood flows, the acquisition time should remain relatively long as compared to conventional ultrasound Doppler.

4. Conclusion

Characterization for ULM spatial and temporal resolution

This study demonstrates that ULM performances in terms of spatial resolution come at the cost of extension of the acquisition time. As MB behavior follows the physiology of the vasculature, we propose that image reconstruction in ULM is above all driven by blood flow. MB concentration have to be adapted to the vessels under investigations, it should be lowered to image sub-millimeter vessels and increased for capillaries. In all cases, as the key to super resolution is having isolated MB, it imposes a fundamental limitation to only see tens of MB in each frame. Therefore, acquisition time is bound to be several minutes to image the capillary bed and the slowest vessels. Compared to the drawbacks of other comparable imaging modalities, several minutes of acquisition times doesn't appear so limiting as ULM could provide a clear window to capillaries and deep vascular structures in animal and humans. A window that could help us understand and diagnose many diseases where the microvasculature plays an important role such as cancer, stroke, diabetes, and arteriosclerosis.

Still some fundamental question unanswered

However, for accurate quantification, at least two questions should be addressed. Firstly, how does the lack of resolution in elevation affect the ability of ULM to clearly quantify velocities and blood flow? The thickness of the image is still in the order of magnitude of λ and all vessels are projected in one plane. Secondly, how do MB behave in the blood, especially in the smallest vessels? We hypothesized that MB follow blood flow but the notion of blood flow becomes irrelevant when the size of the vessel approaches the size of MB and red blood cells. To address these questions, a comparison with a ground truth will be needed. In particular, I foresee that chicken embryo will be an appropriate model as it offers the possibility to perform concurrent ultrasound and optical imaging. In this task, I assisted Walid Assaini, an intern, to develop an experimental setup to perform concurrent optic and ULM. He was able to produce a first set of images. Although this is still preliminary work, it opens the way for a much finer understanding of MB flow, image reconstruction, and fidelity of ULM to the underlying vasculature.

5. References

- Errico C, et al. (2015) Ultrafast ultrasound localization microscopy for deep super-resolution vascular imaging. *Nature* 527(7579):499–502. doi: 10.1038/nature16066
- Couture O, et al. (2011) Microbubble ultrasound super-localization imaging (MUSLI), p. 1285-1287
- Christensen-Jeffries, K. *et al.* Microbubble Axial Localization Errors in Ultrasound Super-Resolution Imaging. *IEEE Trans Ultrason Ferroelectr Freq Control* **64**, 1644–1654 (2017).
- Desailly Y, Pierre J, Couture O, Tanter M (2015) Resolution limits of ultrafast ultrasound localization microscopy. *Physics in Medicine and Biology* 60(22):8723–8740. doi: 10.1088/0031-9155/60/22/8723
- Betzig E, et al. (2006) Imaging Intracellular Fluorescent Proteins at Nanometer Resolution. *Science* 313(5793):1642–1645. doi: 10.1126/science.1127344
- O'Reilly MA, Hynynen K (2013) A super-resolution ultrasound method for brain vascular mapping. *Med Phys* 40(11). doi:10.1118/1.4823762.
- Viessmann OM, Eckersley RJ, Christensen-Jeffries K, Tang MX, Dunsby C (2013) Acoustic super-resolution with ultrasound and microbubbles. *Physics in Medicine and Biology* 58(18):6447–6458. doi: 10.1088/0031-9155/58/18/6447
- Christensen-Jeffries K, Browning RJ, Tang MX, Dunsby C, Eckersley RJ (2015) In Vivo Acoustic Super-Resolution and Super-Resolved Velocity Mapping Using Microbubbles. *IEEE Transactions on Medical Imaging* 34(2):433–440. doi: 10.1109/TMI.2014.2359650

- Foiret J, et al. (2017) Ultrasound localization microscopy to image and assess microvasculature in a rat kidney. *Scientific Reports* 7(1). doi:10.1038/s41598-017-13676-7.
- Lin F, et al. (2017) 3-D Ultrasound Localization Microscopy for Identifying Microvascular Morphology Features of Tumor Angiogenesis at a Resolution Beyond the Diffraction Limit of Conventional Ultrasound. *Theranostics* 7(1):196–204. doi: 10.7150/thno.16899
- Song P, et al. (2018) Improved Super-Resolution Ultrasound Microvessel Imaging with Spatiotemporal Nonlocal Means Filtering and Bipartite Graph-Based Microbubble Tracking. *IEEE Trans Ultrason Ferroelectr Freq Control* 65(2):149–167. doi: 10.1109/TUFFC.2017.2778941
- Desailly Y, et al. (2017) Contrast enhanced ultrasound by real-time spatiotemporal filtering of ultrafast images. *Physics in Medicine and Biology* 62(1):31–42. doi: 10.1088/1361-6560/62/1/31
- Hingot V, Errico C, Tanter M, Couture O (2017) Subwavelength motion-correction for ultrafast ultrasound localization microscopy. *Ultrasonics* 77:17–21. doi: 10.1016/j.ultras.2017.01.008
- Schneider M (1999) Characteristics of SonoVue™. *Echocardiography* 16(s1):743–746. doi: 10.1111/j.1540-8175.1999.tb00144.x
- Bianconi E, et al. (2013) *An estimation of the number of cells in the human body* doi:10.3109/03014460.2013.807878.
- Ivanov KP, Kalinina MK, Levkovich YI (1981) Blood flow velocity in capillaries of brain and muscles and its physiological significance. *Microvascular Research* 22(2):143–155. doi: 10.1016/0026-2862(81)90084-4
- Herman IP (2016) Fluid Pressure, Fluid Flow in the Body, and Motion in Fluids. *Physics of the Human Body* (Springer), pp 491–531.
- Demené C, et al. (2015) Spatiotemporal Clutter Filtering of Ultrafast Ultrasound Data Highly Increases Doppler and fUltrasound Sensitivity. *IEEE Transactions on Medical Imaging* 34(11):2271–2285. doi: 10.1109/TMI.2015.2428634
- Bercoff J, et al. (2011) Ultrafast compound doppler imaging: providing full blood flow characterization. *IEEE Transactions on Ultrasonics, Ferroelectrics, and Frequency Control* 58(1):134–147. doi: 10.1109/TUFFC.2011.1780
- Henriques R, et al. (2010) QuickPALM: 3D real-time photoactivation nanoscopy image processing in ImageJ. *Nature Methods* 7(5):339–340. doi: 10.1038/nmeth0510-339
- Heiles et al. Volumetric ultrafast ultrasound localization microscopy using a 32x32 matric array.
- Kuhn HW (2010) The Hungarian Method for the Assignment Problem. *50 Years of Integer Programming 1958-2008*, eds Jünger M, et al. (Springer Berlin Heidelberg, Berlin, Heidelberg), pp 29–47. doi: 10.1007/978-3-540-68279-0_2

- Walker, W. F. & Trahey, G. E. A fundamental limit on delay estimation using partially correlated speckle signals. *IEEE Trans. Ultrason., Ferroelect., Freq. Contr.* **42**, 301–308 (1995).
- Lin, C.-Y. *et al*. *In vivo* cerebromicrovasculatural visualization using 3D DeltaR2-based microscopy of magnetic resonance angiography (3DDeltaR2-mMRA). *Neuroimage* **45**, 824–831 (2009)
- Svoboda, K. & Yasuda, R. Principles of Two-Photon Excitation Microscopy and Its Applications to Neuroscience. *Neuron* **50**, 823–839 (2006).

Chapter 4: Motion correction for Ultrasound Localization Microscopy

1. General problem of motion in Ultrasound Localization Microscopy

Motions in ultrasound imaging

Ultrasonography is one of the most common medical imaging tool and is widely used around the world. An exam usually sees a physician hold the probe with his hand and go over the patient body to explore. As the patient breathes and moves, together with the hand of the physician, tissue motion strongly affect the image. In abdominal organs, respiration motions can displace organs relatively to the probe as far as 20 mm in one breath (***Song R et al. 2011***). Because the spatial resolution of ULM is in the tens of μm and its temporal resolution of a few minutes, motion artefacts dramatically affects imaging performances.

Fixing the probe and the patients can be a viable solution when imaging the brain, where stereotaxic frames are common are relatively painless. However, it is hardly a viable option for internal organs like kidneys, pancreas, etc. Gating the respiration is sometime a solution but cannot be precise enough to correct motions at microscopic scales. Because acquisition times can be of several minutes, asking patients to hold their breath is also out of question. In some studies, the issue of motion was answered in ULM by discarding the images affected by motions. This meant discarding up to 30% of the images (***Lin F et al 2017, Opacic T et al 2018***). Therefore, robust methods for motion estimation and compensation need to be developed to correct images.

The field of motion estimation in ultrasound is already very rich as estimating blood flow, tissue displacements and compensating for tissue motions have been a major preoccupation in ultrasound imaging and therapy (***Trahey G, E et al 1987***, ***Bohs L. N. et al 1991***, ***Loupas T et al, 1995***, ***Tanter M et al. 2002, Pernot M et al. 2004, Pinton G et al 2006, Denarie B et al 2013***, ***Pinton G et al 2014***). The estimation can be very precise, much more than the ultrasound wavelength (***Tanter M et al. 2002, Pinton G et al 2006***), and down to the micrometric scale. Most methods rely on the estimation of time delays and require the saving of the non beamformed data and the acquisition of relatively large sets of compounding angles to perform well in both directions. For ULM, I chose to not save the non beamformed data in order to increase the number of frames that could be acquired every second and therefore chose to develop a compensation method based on beamformed data. These were limits imposed by the acquisition system we had at that time and may not be relevant in the near future as data transfer and saving are getting faster on the latest generations of ultrafast scanners which enables the saving of the non beamformed data within ULM compatible acquisition sequences.

The approach I will have in this chapter relies not on direct motion estimation but on image registration to realign images (***Golemati S et al, 2003***, ***Goshtasby A et al, 2012***, ***Chengqian C. et al 2017***). The objective of this chapter is to discuss some different methods for image registration and their relevance and efficiency for motion correction in ULM. I will first set a theoretical frame to define what is a motion in imaging, before addressing two situations with different methods for motion estimation and correction. In the case of rigid motions, the estimation can be done directly on the images using 2D cross correlation techniques. In the case of affine motion, more advanced estimation technique can be used. A general method for motion estimation can then be defined. In particular, the issue of correction in the case of rigid motions was published to show how simple methods can be used to correct motion in ULM (***Hingot V et al 2017***). As there exist several methods with different sets of advantages and drawbacks, this Chapter doesn't aim to be an extensive review of motions estimation methods and only provide one satisfactory method for our data in ULM.

Theoretical frame for motion correction

To describe the motions, we define a displacement field D_k that affect to a point (z, x) a new set of coordinates $D_k(z, x)$. D_k is a continuous 2 variable function in which the image I_{k+1} can be written as a function of I_k and D_k.

$$I_{k+1}(z, x) = Im_k(D_k(z, x)) \quad (1)$$

In the plane, there exist an infinity of different motions. We separate them into two categories: affine and elastic. Affine deformations preserve straight lines in 2D and planes in 3D whereas elastic deformations don't. Elastic transformations can in most cases be approached by local affine transformations. Therefore, in the following considerations, we focus only on affine registration. The base of all motion correction schemes is to estimate the displacement field D_k and then apply the inverse displacement field ${D_k}^{-1}$ to realign images. In a 2D plane, affine transformations are translations, rotations, shears and scalings. The displacements field D_k can be written as 3x3 matrix.

$$D_k : (z, x) \longmapsto (z', x') = D_k \begin{pmatrix} z \\ x \\ 1 \end{pmatrix} \quad (2)$$

Translation	Rotation	Scaling	Shear	General affine
$\begin{pmatrix} 1 & 0 & \Delta Z \\ 0 & 1 & \Delta X \\ 0 & 0 & 1 \end{pmatrix}$	$\begin{pmatrix} \cos\theta & -\sin\theta & 0 \\ \sin\theta & \cos\theta & 0 \\ 0 & 0 & 1 \end{pmatrix}$	$\begin{pmatrix} S_z & 0 & 0 \\ 0 & S_x & 0 \\ 0 & 0 & 0 \end{pmatrix}$	$\begin{pmatrix} 1 & \tau_x & 0 \\ \tau_z & 1 & 0 \\ 0 & 0 & 1 \end{pmatrix}$	$\begin{pmatrix} d_{11} & d_{12} & d_{13} \\ d_{21} & d_{22} & d_{23} \\ 0 & 0 & d_{33} \end{pmatrix}$

2. Motion estimation in ultrasound: a spatial approach

Registration problem

The classical problem of image registration is to estimate the displacement between two images to realign them. There are multiple ways to estimate the displacement but there exist two main categories: feature based and intensity based. Feature based method relies on identification of punctual features of the images. A point is identified by the repartition of intensity and its derivatives around it. If the point is singular enough, it is easy to identify it in another image. The method relies on the identification of a set of reference point to register the image and is therefore very fast to compute. It is widely used in optics and photographs. However, if the features on the images are smooth and unclear, this method tends to not be very efficient. Moreover, it doesn't always allow precise sub-pixel registration. In ultrasound, tissues produce speckle patterns with weak features. Intensity based approaches are more appropriate. All affine transformation except shear can be directly measured using direct 2D correlation (***Reddy B et al. 1996***) with a precision depending only on the SNR of the images. The shear and elastic transformation can be estimated using iterative algorithms. In all cases, those methods exist to register images with sub-pixel accuracy. Direct methods will be less costly to compute but might not correct eventual shear whereas iterative method might approach the real deformations but its precision greatly depends on the parameterization of the algorithm and is quite heavy to compute.

Direct estimation of translations using 2D cross correlation

In the case that the motion is a translation $(\Delta Z_k, \Delta X_k)$, the shift can be easily written in the Fourier domain as a phase shifting. If $\mathrm{F_k}$ and $\mathrm{F_{k+1}}$ are the 2D Fourier transform of the images Im_k and Im_{k+1}, the translation can be expressed a constant phase shift φ_k in the unitary Fourier base (u, v) where L_z, L_x are the size of the image (*Figure 1.A*).

$$F_{k+1}(u,v) = F_k(u,v)e^{-2i\pi\varphi_k} \quad with \quad \varphi_k = \frac{u\Delta Z_k}{L_z} + \frac{v\Delta X_k}{L_x}$$

For this type of motions, the cross correlation is a simple Dirac function whose coordinates are $(\Delta Z_k \Delta X_k)$. Finding the position of the maximum of the cross correlation can be done with sub-pixel precision and enables the estimation of the translation (*Figure 2.B*).

$$C_k = F^{-1}\left(\frac{F_k {F_{k+1}}^*}{|F_k {F_{k+1}}^*|}\right) = \delta(\Delta Z_k, \Delta X_k)$$

The precision depends only on the Signal to Noise ratio and the localization estimator and can be much more precise than the original grid size. The maximum can be localized using the weighted average function for localization for MB. From there, it is easy to realign images using the estimated translation (*Figure 1.C*). It is important to say that the precision of the estimation of the displacement only depends on the Signal to Noise Ratio of the images. It is therefore very susceptible to noise and parasite artefacts that can be present in the images.

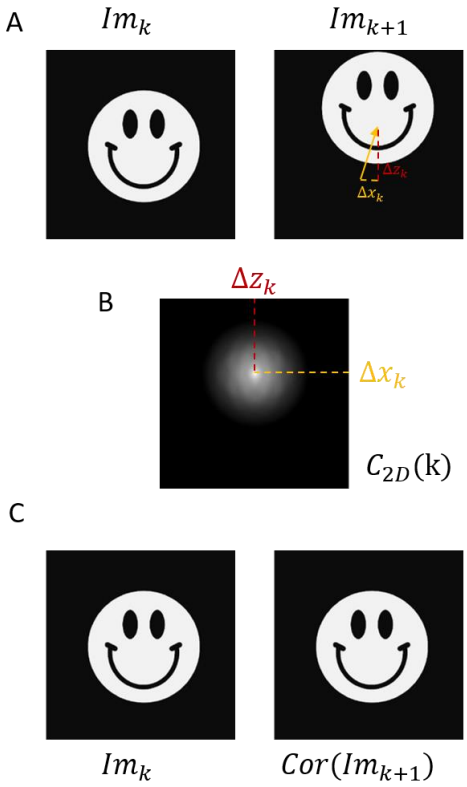

Figure 1: Translation estimation using 2D Cross correlation

A. Original and translated images **B**. Search of the translation coordinates as the maximum of the cross correlation. **C**. Correction of the translated image by applying the measured translation.

Case of rotational and scaling motions

In the case that there is also a rotation and scaling (*Figure 2.A*), cross correlation can also estimate the scaling factor and the rotation independently of a potential translation by using a polar transform on the magnitude spectrum (*Figure 2.B*). This operation is also called Fourier Mellin transform and uses the fact that Fourier transform separates translation and rotations/scaling in the magnitude and phase of the spectrum. With a log-polar transform in the Fourier domain (*Figure 2.C*), the scaling and rotation are a constant phase shift on the magnitudes and can be easily estimated using 2D cross correlation.

Therefore, we can independently estimate the translation, rotation and scaling simply by the computation of the 2D Fourier transforms (*Figure 2.D*).

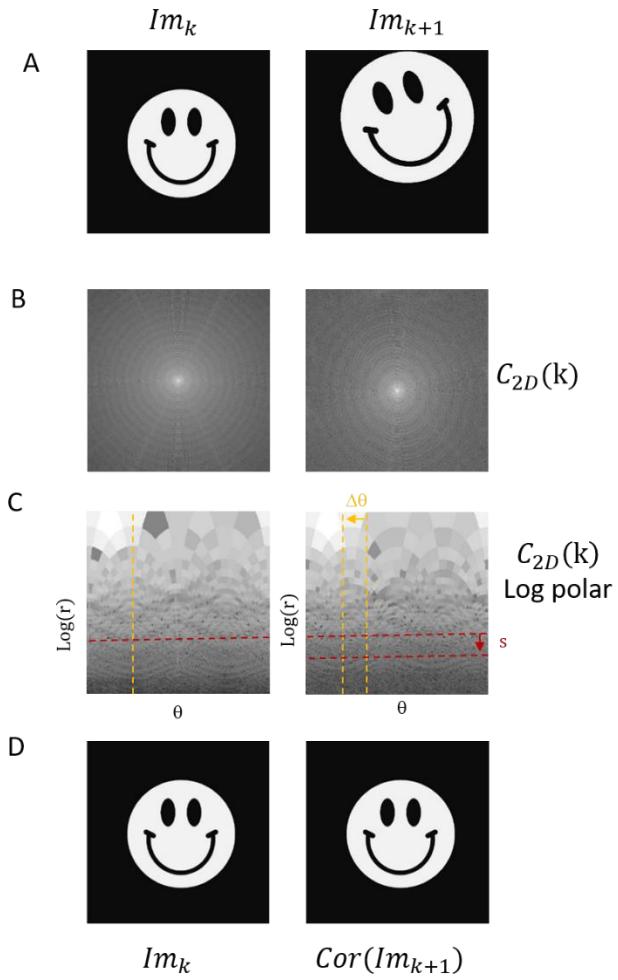

Figure 2: Rotation and scaling estimation using 2D Cross correlation methods

A. Original and modified images B. 2D Fourier transform of original and modified images. C. Log polar transformation of the 2D Fourier transform magnitude. D. Correction of the translated image by applying the inverse of the measured transformation.

General case of affine transformations

In the case of a general affine transformation, shears cannot be estimated with direct cross correlation. Algorithms exist to estimate the general transformation matrix (*imregister & imregtform*) for all affine transformation. They are based on an iterative algorithm who estimates a multi variable gradient of a similarity function between images to register and eventually converge on a set on a transformation matrix. The quality of the final transformation, in particular for sub-pixel motions is however hard to estimate.

3. Application to motion correction for Ultrasound Localization Microscopy

Translation estimation in the rat's brain

The first model of simple motion we had was a set of data where the rat's head wasn't fixed in a stereotactic frame and rested directly on a heating pad. Motions were small and rigid. It is a fairly simple model of motion that are only rigid. It is however relevant of some real applications, mainly for imaging of the brain where the probe cannot be fixed. For example, imaging of freely moving animals where the probe can slightly move or during a hand held exam. In this case, direct motion estimation could be done using the estimation of the phase on 2D cross correlation with a reference frame. A major point of the study was to point at the necessity to filter MB before estimating the motions to limit errors. Singular Value Decomposition filters were used to separate tissue MB signals to form 2 sets of frames, one with mostly tissue signals, one with mostly MB signal. For the tissue signal dataset, each frame (*Figure 3.A*) was compared with a reference frame, chosen as the central frame of the acquisition (*Figure 3.B*). The cross correlation was performed for each frame (*Figure 3.C*).

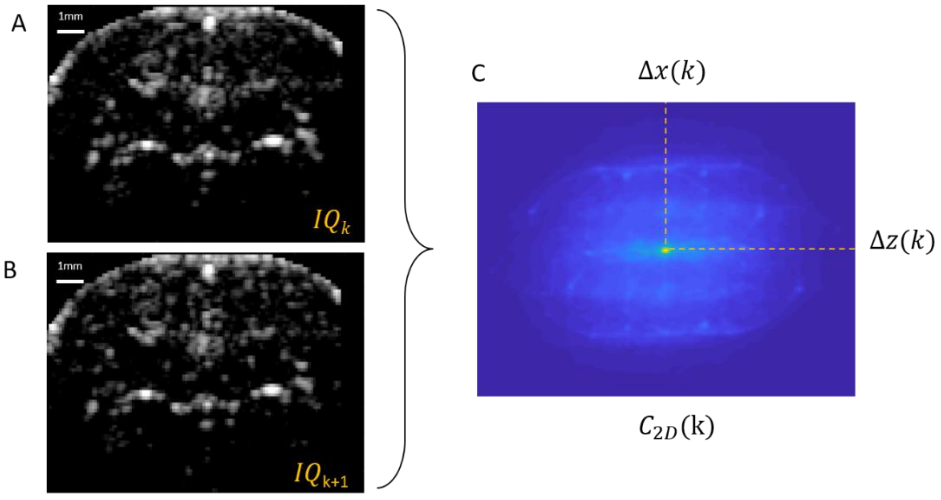

Figure 3: Cross correlation in the rat's brain

A. Reference frame **B**. Displaced frame. **C**. Cross correlation between the two images reveal a pic.

The localization of the peak was done with the same localization algorithm as what was used for MB localization, which is interpolation with a Lanczos kernel in the first versions, then using the more advanced weighted average algorithm. It was the most adapted tool we had to estimate the sub-pixel position of the maximum and executed with the best computation time. Each image was then translated back to realign them with the reference frame. The usual ULM processing steps were then performed. Comparison between original (*Figure 4.A*) and corrected images (*Figure 4.B*) show the effectiveness of the registration process.

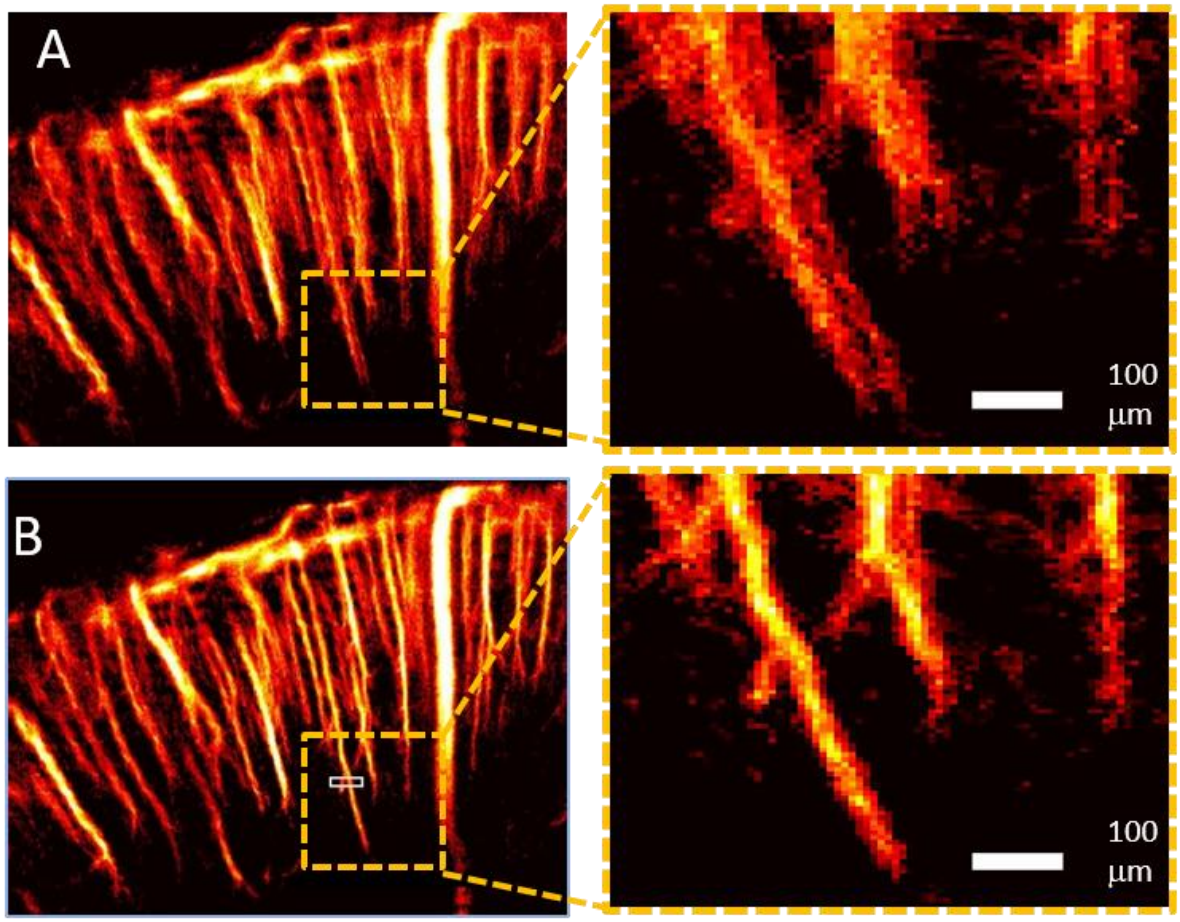

Figure 4: Translation correction in the rat's brain

A. ULM without correction. B. ULM after rigid correction (*Hingot V et al 2017*).

The same process was performed without having separated MB from tissues before performing the displacement estimation. This lead to a loss of contrast for the cross correlation peak and an overall error of 30 µm compared to the dataset with previous filtering and therefore a less effective registration. The same framework can then be adapted to the general case of affine registration where the motion estimation is not based on 2D cross correlation but on an iterative search.

General framework

The original dataset (*Figure 5.A*) has first to be low pass filtered (*Figure 5.B*) to remove MB motions contribution. From there, motions are estimated on the filtered dataset (*Figure 5.C*). The motion correction can be done on MB positions or on the original dataset before the complete ULM algorithm can be executed on a corrected dataset. The efficiency and relevance of those two approach depend on the type and extent of motion present in the dataset.

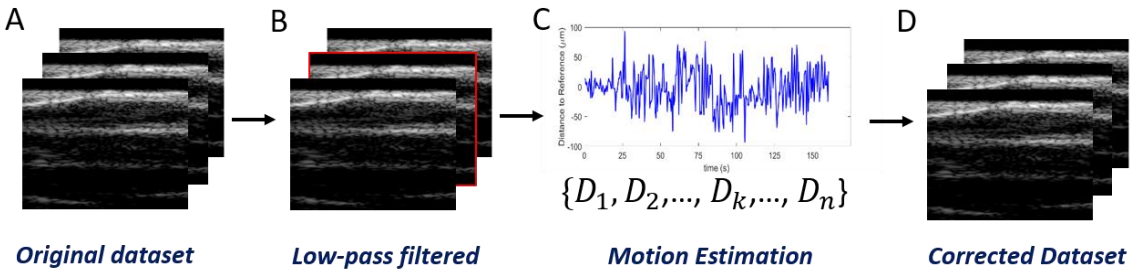

Figure 5: Motion correction framework in ULM

A. Original dataset B. Low pass filtering to remove MB signal C. Motion estimation step using cross correlation or iterative search D. Correction of the dataset before application of the regular ULM framework.

It is worth noting that for nonlinear imaging separation of tissues and MB, the registration could be performed on the linear image instead of using low pass filter. Here, two examples of affine correction in the rat's spinal cord and in the cortex of a rat's kidney. For non-rigid motions, the displacements were estimated using the affine registration estimation provide by Matlab (*imregister*) instead of the cross correlation method. Here, we demonstrate in a rat's spinal cord the efficiency of these approach. In *Figure 6.A* is the original image of over a coronal plane of a rat's spinal cord prior to motion correction whereas in *Figure 6.B*, the same image can be corrected and reveal finer vessel edges, a better definition of vessels and a better contrast.

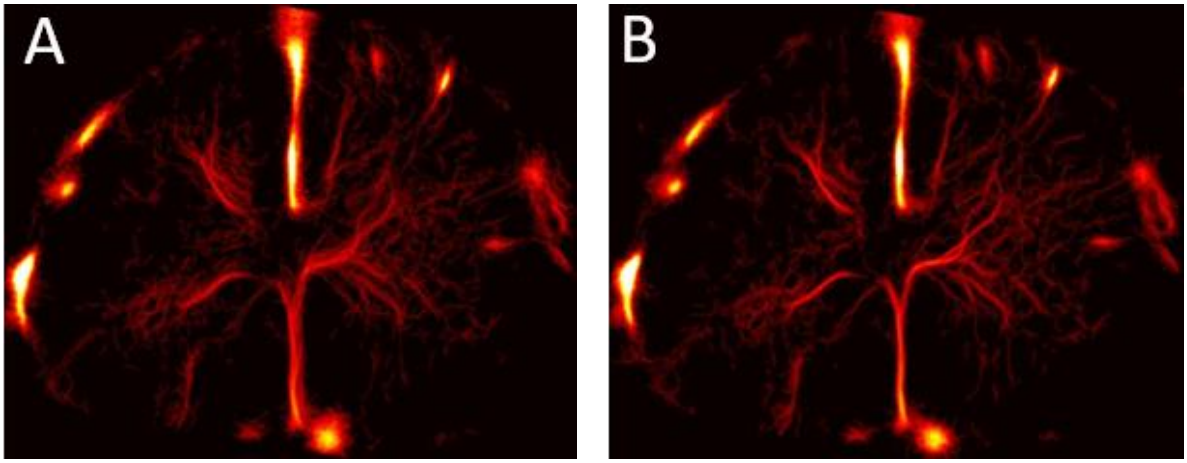

Figure 6: General affine correction in the rat's spinal cord

A. ULM without correction. B. ULM after affine correction.

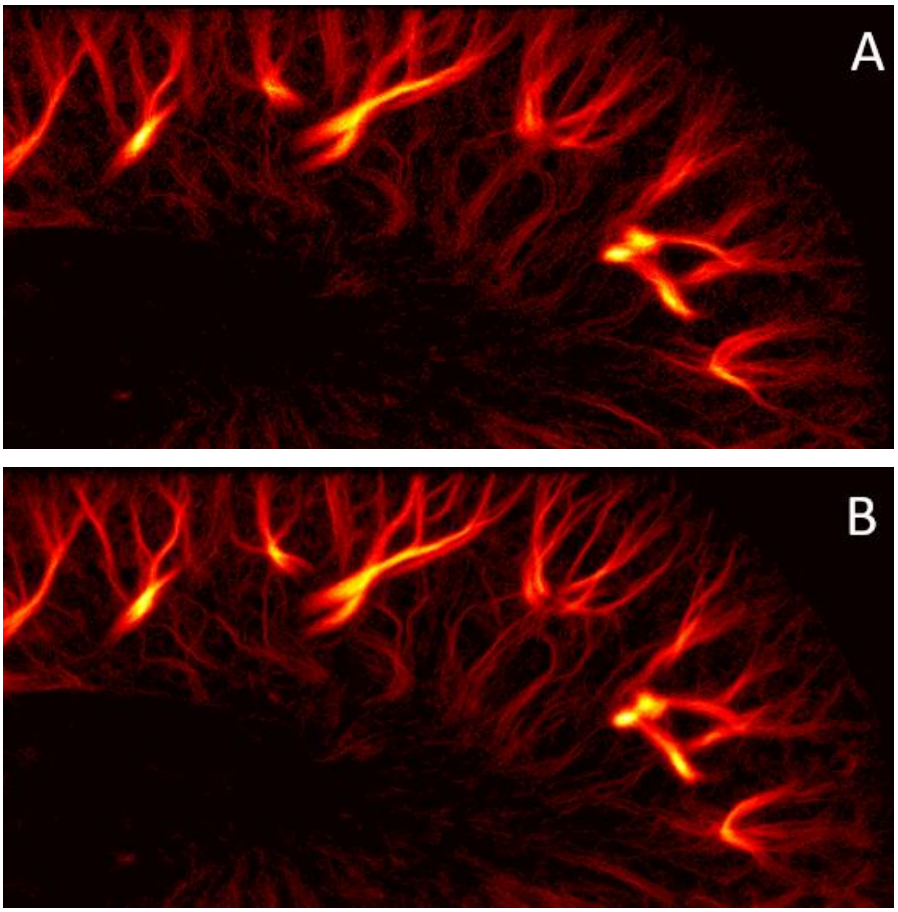

Figure 7: General affine correction in the cortex of a rat's kidney

A. ULM without correction. B. ULM after affine correction.

4. Conclusion

This chapter shows that registration methods could be effective for motion correction in ULM. Direct estimation of translations was demonstrated in the case of the rat's brain, and iterative estimation of affine motions was demonstrated in the rat's spinal cord and kidney. The most obvious drawback of those methods is that in some extreme cases, affine transformations are not effective and elastic registration should be performed instead. Though some methods are already available, they are very sensitive to noise and are not necessarily adapted for ULM where the accuracy of registration should be precise at the tenth of a pixel. The sensitivity to noise is a classical drawback associated with all registration methods based on intensity matching or correlation. In exposed and shallow organs like the kidney of exposed spinal cord or brain, the signal to noise ratio was barely a problem. However, for real clinical practice, organs will be deeper or surrounded by layers of bone or fat and signal to noise ratio will definitely be an issue.

Lastly, when the motions can only be corrected in the imaging plane. When the organ moves in and out of the imaging plane, there is no way to estimate and correct them with a 2D probe. However, recent progress made showed that ULM could be performed in 3D (***Heiles B et al 2019***). In these conditions, we can imagine that motions would eventually be tracked in all directions which would make for a more robust correction. However, computation time is already long in 2D. For 2D affine correction, in my setup, it takes 5 hours to register a set of 150.000 images of 78x128 pixels. For 3D correction with this method, the computation time might be multiplied by the number of pixels in the elevation direction, and it might take a week to compute the motion correction.

5. References

- Tanter, M. & Fink, M. Ultrafast imaging in biomedical ultrasound. IEEE Transactions on Ultrasonics, Ferroelectrics, and Frequency Control 61, 102–119 (2014).
- Tanter, M. & Fink, M. Ultrafast imaging in biomedical ultrasound. *IEEE Transactions on Ultrasonics, Ferroelectrics, and Frequency Control* **61**, 102–119 (2014).
- Tanter, M., Bercoff, J., Sandrin, L. & Fink, M. Ultrafast compound imaging for 2-D motion vector estimation: application to transient elastography. *IEEE Transactions on Ultrasonics, Ferroelectrics, and Frequency Control* **49**, 1363–1374 (2002).
- Song, R., Tipirneni, A., Johnson, P., Loeffler, R. B. & Hillenbrand, C. M. Evaluation of respiratory liver and kidney movements for MRI navigator gating. *Journal of Magnetic Resonance Imaging* **33**, 143–148 (2011).
- Reddy, B. S. & Chatterji, B. N. An FFT-based technique for translation, rotation, and scale-invariant image registration. *IEEE Transactions on Image Processing* **5**, 1266–1271 (1996).
- Pernot, M., Tanter, M. & Fink, M. 3-D real-time motion correction in high-intensity focused ultrasound therapy. *Ultrasound in Medicine & Biology* **30**, 1239–1249 (2004).
- Goshtasby A, Image Registration, 2012
- Harput S, Two-Stage Motion Correction for Super-Resolution Ultrasound Imaging in Human Lower Limb IEEE Transactions on Ultrasonics, Ferroelectrics, and Frequency Control (Volume: 65 , Issue: 5 , May 2018)
- Desailly, Y., Couture, O., Fink, M. & Tanter, M. Sono-activated ultrasound localization microscopy. Appl. Phys. Lett. 103, 174107 (2013).
- Errico, C. et al. Ultrafast ultrasound localization microscopy for deep super-resolution vascular imaging. Nature 527, 499–502 (2015).

- Couture, O., Hingot, V., Heiles, B., Muleki-Seya, P. & Tanter, M. Ultrasound Localization Microscopy and Super-Resolution: A State of the Art. IEEE Transactions on Ultrasonics, Ferroelectrics, and Frequency Control 65, 1304–1320 (2018).
- Hingot, V. *et al.* Microvascular flow dictates the compromise between spatial resolution and acquisition time in Ultrasound Localization Microscopy. *Scientific Reports* **9**, (2019).
- Desailly, Y. *et al.* Contrast enhanced ultrasound by real-time spatiotemporal filtering of ultrafast images. *Physics in Medicine and Biology* **62**, 31–42 (2017).
- Brown, J. et al. Investigation of Microbubble Detection Methods for Super-Resolution Imaging of Microvasculature. IEEE Trans Ultrason Ferroelectr Freq Control 66, 676–691 (2019).
- Provost, J. *et al.* 3D ultrafast ultrasound imagingin vivo. *Phys. Med. Biol.* **59**, L1–L13 (2014).
- Heiles, B. *et al.* Ultrafast 3D Ultrasound Localization Microscopy using a 32×32 Matrix Array. *IEEE Transactions on Medical Imaging* 1–1 (2019).
- M. Tanter, J. Bercoff, L. Sandrin, and M. Fink, “Ultrafast compound imaging for 2-D motion vector estimation: Application to transient elastography,” IEEE Trans. Ultrason
- L. N. Bohs and G. E. Trahey, "A novel method for angle independent ultrasonic imaging of blood flow and tissue motion," in *IEEE Transactions on Biomedical Engineering*, vol. 38, no. 3, pp. 280-286, March 1991.
- G. E. Trahey, J. W. Allison, O. T. V. Ramm, "Angle independent ultrasonic detection of blood flow", *IEEE Trans. Biomed. Eng.*, vol. 34, pp. 965-967, Dec. 1987
- Denarie B, Tangen TA, Ekroll IK, Rolim N, Torp H, Bjastad T. et al. Coherent plane wave compounding for very high frame rate ultrasonography of rapidly moving targets. IEEE transactions on medical imaging. 2013;32:1265–76.
- G. Pinton, J. Gennisson, M. Tanter and F. Coulouvrat, "Adaptive motion estimation of shear shock waves in soft solids and tissue with ultrasound," in *IEEE Transactions on Ultrasonics, Ferroelectrics, and Frequency Control*, vol. 61, no. 9, pp. 1489-1503, Sept. 2014
- T. Loupas, J. T. Powers and R. W. Gill, "An axial velocity estimator for ultrasound blood flow imaging, based on a full evaluation of the Doppler equation by means of a two-dimensional autocorrelation approach," in *IEEE Transactions on Ultrasonics, Ferroelectrics, and Frequency Control*, vol. 42, no. 4, pp. 672-688, July 1995.
- Golemati, Spyretta et al. Carotid artery wall motion estimated from b-mode ultrasound using region tracking and block matching Ultrasound in Medicine and Biology, Volume 29, Issue 3, 387 – 399
- Chengqian Che, Tejas Sudharshan Mathai, John Galeotti,Ultrasound registration: A review, Methods, Volume 115, 2017, Pages 128-143, ISSN 1046-2023,

Chapter 5: Early ultrasound imaging predicts outcome in ischemic stroke

1. Introduction

In the context of stroke, the question of imaging is key. For clinical medical care, imaging the state of cerebral perfusion is crucial in the early phase of the pathology as the diagnostic and therefore proper treatment cannot be done prior to imaging. It also enables the monitoring of the response to treatment after thrombolysis or thrombectomy. As seen in *Chapter 1*, the limited access to effective imaging tools doesn't allow for systematic and early imaging and has a negative impact on patient prognosis. Moreover, translational research in the context of stroke also suffer from the lack of performant imaging method. A major limitation to translate the results in animals to human patients is the lack of relevant animal models and the lack of imaging tools to understand the physiological mechanisms. As stroke is a complex pathology, good animal models are required to effectively represent the pathology as it is in clinical care. Even when considering the translation of imaging modalities, the question of the animal model should be a central concern. A recent model was developed in Caen in the team of Cyrille Orset and Denis Vivien in which a real fibrin clot is formed in the MCA (***Orset C et al 2007***). After a retrospective study over different research teams and various studies, the model is now considered relevant to the physiology of ischemic stroke (***Orset et al 2016***). This work is a collaboration between specialist of ischemic stroke (Denis Vivien and Cyrille Orset) and specialist of ultrasound imaging (Olivier Couture, Thomas Deffieux and Mickael Tanter) that I did with Camille Brodin, Ph.D. student in Caen. My contribution is combining those two expertise and develop an ultrasound based imaging setup which will benefit preclinical research and prepare the translation to human patients.

The aim of the present chapter is to demonstrate how Ultrafast Ultrasound can be a relevant imaging modality in the context of thromboembolic stroke using two imaging modalities: 4D Ultrasensitive Doppler based on tomography (***Demene C et al. 2015, Deffieux T et al. 2018***) and Ultrasound Localization Microscopy (***Couture O. et al. 2018***). This work demonstrates that 4D Ultrasensitive Doppler can provide longitudinal characterization of cerebral perfusion over the whole mouse brain during an ischemic episode and the follow-up. It also demonstrates that ULM can bring more sensitivity and contrast to vascular imaging in the brain and therefore a finer characterization of alteration and restoration of blood flow during ischemic stroke. This work contributes to the understanding of how ischemic lesions evolve with time after stroke onset and how early reperfusion can save brain tissue. More importantly, this study leads to the proof of concept that Ultrafast Ultrasound imaging can be used early after stroke onset to predict outcome and response to treatment, as a pre requirement prior to translation to the clinic.

2. Material and Methods

Animal preparation

Swiss male mice (35-40 g; Janvier Labs, France) aged 8-10 weeks old were used. All experiments were performed in accordance with the French ethical law (Decree 2013-118) and the European Communities Council guidelines (2010/63/EU) and were approved by institutional review board (French ministry of Research) and by the local ethical committee of Normandy (CENOMEXA) registered under the reference CENOMEXA-C2EA – 54 and received the agreement number #13412. All applicable international, national, and/or institutional guidelines for the care and use of animals were followed.

Surgical procedures

Mice were anesthetized with isoflurane (induction at 5% and maintenance at 2%) in a gas mixture of $N0_2/O_2$ (70/30%). Once placed in the stereotactic frame, a catheter was placed in the tail vein of mice, to allow intravenous injection. The skin above the skull was opened and pushed to the sides of the head. Internal mice's temperature was maintained at 37°C using a rectal probe and a heating pad. A 1 cm skin incision between the ear and eye was performed. The masseter muscle was retracted, a local craniotomy was done on the temporal side of the skull to expose the middle cerebral artery (MCA) and the dura was removed locally in preparation for MCA occlusion. Ultrasound gel was placed on the mouse skull. The probe was moved near the skull in order to carry out the acquisitions. After 2 hours of ultrasound imaging, the skin was stitched and sprayed liberally with lidocaïne. 24 hours later, mice were anesthetized, placed on the stereotactic frame, catheterized, and their skin opened before another session of ultrasound imaging after what they were sacrificed.

Middle Cerebral Artery occlusion in the thromboembolic model

A micropipette was filled with 1µL of purified murine alpha thrombin (1UI ; 0.05 mg ; Stago BNL). The pipette was introduced in the lumen of the MCA and the microliter of murine thrombin was slowly injected to form a fibrin clot. The micropipette was let in place for 10 minutes to let the clot stabilize.

Tissue-Type Plasminogen Activator induced thrombolysis

To induce thrombolysis, 10 mice received intravenous injection of 200 µL of tPA (10 mg/kg, Actilyse), 10% as a bolus and the remaining 90% as an infusion for 40 minutes. A control group of 10 mice was injected with saline under the same conditions.

Middle Cerebral Artery occlusion in the electrocoagulation model

The electrosurgical coagulator (AESCULAP Typ TB 50 Electrosurgical Unit Bipolar Coagulator) was used. The bipolar mode was selected at 8W. The artery was coagulated under MCA bifurcation between its posterior and anterior branches (distal occlusion) with the forceps and was cut transversely to ensure the success of the permanent occlusion surgery.

Ultrafast Ultrasound Imaging

Ultrafast ultrasound imaging was performed on a research ultrafast scanner (128 channels, 62.5 MHz sampling rate) and Neuroscan live acquisition software (ART Inserm U1273, Paris, France & Iconeus, Paris, France) with a custom ultrasound probe (15 MHz, 0.11 mm pitch, Vermon, France) which enables à 110 µm x 100 µm in plane resolution with a depth of 10 mm. The probe was mounted on 4 motors (3 translation + 1 rotation, Pi, Germany). As both the stereotactic frame and the motorization system were fixed to the table, a common coordinate system was determined and remained so each animal could be imaged at 24 hours in the same configuration. In all this study, the coordinate system is (*z,x,y*) with *z* the axial axis, *x* the lateral axis and *y* the elevation axis as shown in *Figure 1*.

Ultrasensitive Doppler

For each ultrafast Doppler image, 200 compounded frames (11 angles between -10° : 10°) were acquired at 500 Hz. Singular Value Decomposition clutter filters were used and the 60 first singular values were removed to separate blood signal from tissues. The energy in each pixel is calculated to form a Power Doppler image. Between two images, a 1.2 s pause was added to let the motor move to the next slice. 24 successive coronal planes were imaged every 0.3 mm to reconstruct a 10 mm x 12.8 mm x 8 mm volume between β+2mm and β-6mm with a spatial resolution of 80 µm x 100 µm x 300 µm and temporal resolution of 40 seconds.

Power Doppler imaging processing (MCA territory identification)

Lesion segmentation was performed using Singular Value Decomposition. The 4D Doppler matrix was reshaped into a 2D matrix with one dimension for space and one dimension for time. SVD was performed on this matrix and combination of singular values were formed on the basis of similarities on the temporal vectors. Spatial vectors were reshaped to a 3D volume highlighting the regions exhibiting the corresponding temporal behavior. Delimitation of the areas was done using the *watershed* technique (Mathworks) for morphological segmentation. Temporal profiles were computed as the average intensity in the segmented region of interest. When image quality was not good enough to ensure proper automatic segmentation and the region of interests were segmented manually.

Ultrasound Localization Microscopy

For each ULM image, 100 µL of Sonovue microbubbles were injected through a catheter placed in the tail vein. 180 blocks of 800 compounded frames (3 angles at -5° 0° 5°) at 1000 Hz were acquired every second. A combination of Butterworth high pass filter (second order, 20 Hz) and Singular Value Decomposition filter (removal of the 10 first singular values) were used to separate microbubbles echoes from tissues. Microbubbles centroid positions were localized with a 10 µm precision using a weighted average on the intensity in neighboring pixels. Microbubbles were tracked through consecutive frames using *simpletracker* (Mathworks), a tracking algorithm based on the Hungarian method for assignment. Tracks were interpolated and smoothed using a sliding window of 5 points and cleaned from redundant positions. All tracks were rounded to fit an 8 µm x 10 µm grid and a density image was reconstructed by counting the number of tracks in each pixel of the grid.

Magnetic Resonance Imaging

MRI acquisitions were performed on a 7T Brucker system. T2-weighted images were acquired using a multislice multiecho sequence: TE/TR 33 ms/2500 ms. Lesion volumes were reconstructed with a 0.7 mm x 0.7 mm x 0.5 mm resolution. Lesions were manually segmented on T2 acquisitions. MRI and ultrafast ultrasound volumes were registered on anatomical similarities using *imregister* (Mathworks), an intensity-based function for multimodal registration.

Data processing and Correction factors

To account for tissue swelling due to the edema, a first correction factor has to be calculated for every mouse. On T_2 MRI images, the distance between the skull and the corpus callosum was measured on both hemispheres of the mouse brain. Because skull thickness increases at the front of the head, ultrasound imaging in the most anterior parts of the head heavy wave attenuation. Consequentially, the contrast and sensitivity to the vasculature are strongly impaired and meaningful analysis could not be performed reliably after β+1.5 mm. As lesions spread up to β+3 mm, the parts between β+1.5 mm and β+3 mm were not included in lesion quantifications in the analysis in *Figure 6*.

Ultrasound based Thrombolysis In Cerebral Ischemia (TICI) score

The TICI score is often used to describe the state of perfusion during an occlusion and is most often evaluated on MR or CT Angiography. Grade 0: No recanalization whatsoever. Grade 1: Recanalization of the artery but no reperfusion of tissue. Grade 2: Recanalization and partial reperfusion (2A: Reperfusion in less than half of the hypoperfused volume, 2B: Reperfusion of most of the hypoperfused volume but with slower flow). Grade 3: Complete reperfusion. Here, it was estimated on ultrasensitive Doppler.

3. Results

Transcranial Ultrafast Ultrasound monitors brain hypoperfusion following thromboembolic stroke

In this study, Ultrafast Ultrasound is introduced as a tool to monitor cerebral perfusion during thromboembolic stroke in mice and following rtPA treatment (*Figure 1.A*). A small high-frequency probe mounted on motorized support and connected to an Ultrafast Ultrasound system enables accurate spatial positioning and fast scanning over the intact mouse brain and skull. A series of compounded plane waves are transmitted at a high frame rate and the echoes are recorded and beamformed to create a set of grayscale images of the cerebral tissues. After spatio-temporal filtering, a Doppler image is reconstructed, whose intensity is proportional to the number of flowing red blood cells within the ultrasound probe's focal spot (***Shung K. K. et al. 1976, Cloutier G. et al. 1997***). Transcranial ultrasensitive Doppler images can be repeated rapidly allowing for a 3D mapping over the whole mouse brain to be quickly achieved through 2 dimensions scanning and repeated for several hours. Every 40 s, a complete volume of 10 mm x 14 mm x 8 mm can be reconstructed with a spatial resolution of 0.1 mm x 0.11 mm x 0.3 mm.

On ultrasensitive Doppler (*Figure 1.B*), the body of the middle cerebral artery (MCA) can be observed on a coronal slice over 1 mm. Directly after occlusion of the MCA (see methods section), blood flow in the artery is completely blocked and the appearance of a large hypoperfused area can be observed in the ipsilateral cortex to the occluded MCA and spreading between -3 mm and -4 mm. In the lateral part of the cortex, fed by the MCA, the blood supply is completely stopped. The most central part of the cortex, fed by the Anterior Cerebral Artery (ACA) is sometimes subjected to small and rapid changes in cerebral blood flow (CBV). During the 2 hours following occlusion and rtPA treatment, restoration of perfusion can be assessed. At 24 hours post-stroke onset and treatment, T_2 weighted MRI reveals areas with high water content corresponding to the ischemic lesion (*Figure 1.C*).

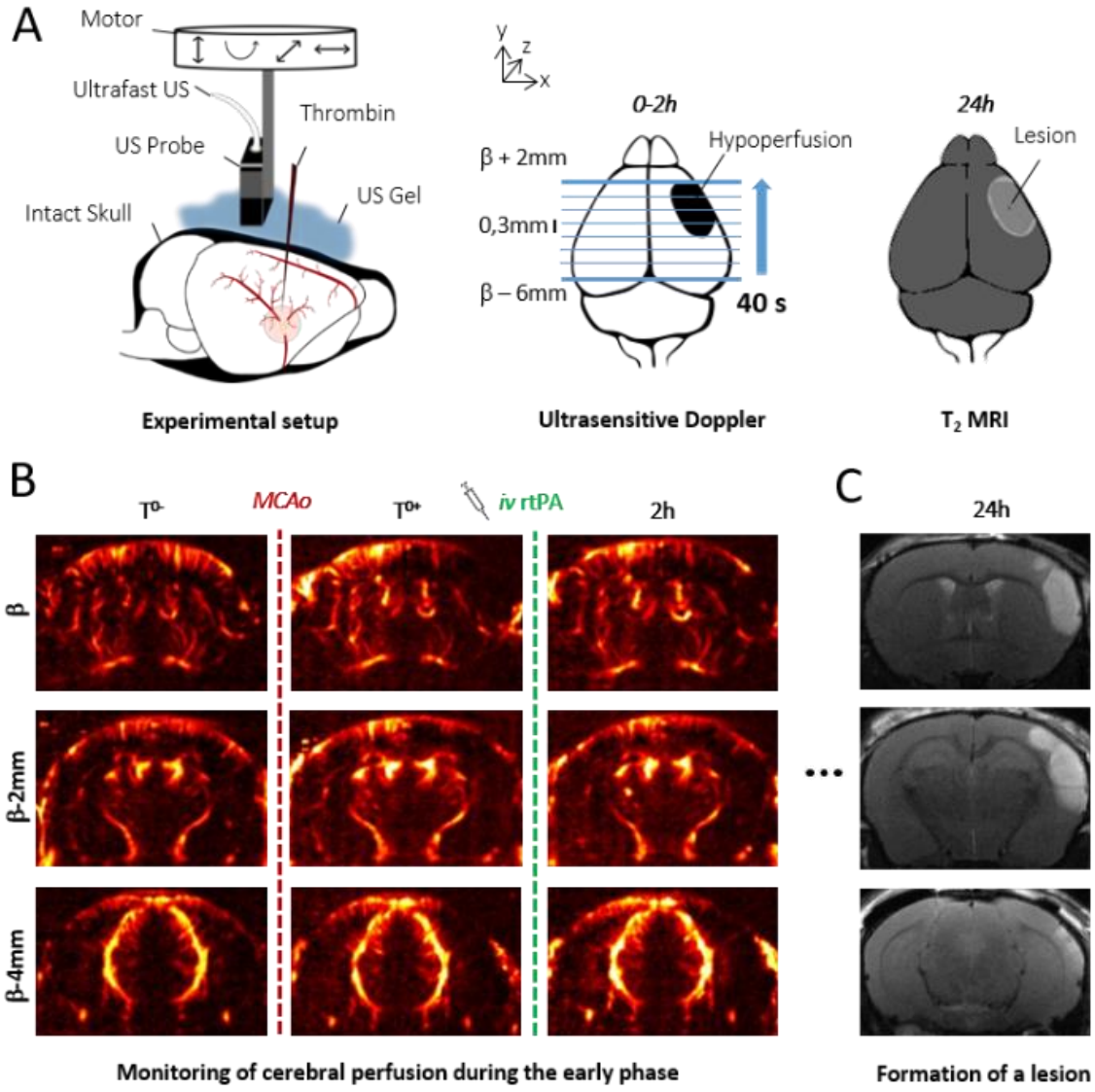

Figure 1. 4D Transcranial ultrasensitive Doppler imaging to monitor cerebral perfusion before, during and after ischemic stroke and comparison with T2 weighted MRI

A. Experimental setup with an ultrasound probe connected to an ultrafast ultrasound acquisition system (Inserm Accelerator of Technological Research) and mounted on a 4 axis-motor for 3D scanning over the whole mice brain by steps of 0.3mm. A volume over the whole brain is reconstructed every 40 seconds. Ultrafast Ultrasound monitors cerebral perfusion during the early phase of the ischemic episode, before, during and after onset, including treatment with the gold standard recombinant-tPA (rtPA). At 24h MRI reveals the final ischemic lesion. B. Ultrasensitive Doppler reveals hypoperfusion in the ipsilateral cortices subjected to thrombin injection (clot formation) in the middle cerebral artery (MCA) and reperfusion of the corresponding territory after injection of the thrombolytic, rtPA. C. Registration and comparison with MRI reveal tight relationships between cerebral perfusion at the early phase of stroke and the final lesion volume.

The ischemic lesion is the hypoperfused volume measured upon stroke onset using ultrafast ultrasound

In the control group, 10 mice were injected with saline 20 minutes after occlusion of the MCA, corresponding to the sham of the rtPA-treated group. Variations in Power Doppler images before and after occlusion exhibit the hypoperfusion in the corresponding ipsilateral cortices (*Figure 2.A*). Additionally, differences in Power Doppler between post-occlusion time and 2 hours after the stroke onset is displayed in *Figure 2.B* and reveal the absence of any reperfusion. 24 h after occlusion, a large lesion can be observed in MRI (*Figure 2.C*).

In 6 animals out of 10, no recanalization whatsoever was detected. Some slight spontaneous recanalization was observed in 4 mice though the artery never allows for blood signal to rise back to pre-clotting levels (*Figure 2.D*). Deep in the tissues fed by the MCA, no reperfusion was observed (*Figure 2.E*). The volumes at risk in ultrasensitive Doppler are defined as the hypoperfused volumes just after the occlusion. On each coronal plane, the hypoperfused areas are manually segmented. Profiles can be reconstructed and reveal a peak around β-1 mm and spreading between β-4 mm and further than β+3 mm (*Figure 2.F*). As the skull gets thicker after β+1 mm, imaging abilities of ultrasound are reduced and image quality does not always allow for accurate segmentation leading to a slight underestimation of hypoperfused volumes.

Total measured volumes at risk are 16 mm^3 ± 3 mm^3. Infarct areas on T_2 weighted MRI reveal lesion spreading between β-5 mm and β+3 mm with a peak also around β-1 mm and co-localization with the hypoperfused areas (*Figure 2.G*). To account for late edema and ultrasound blindness between β+1 mm and β+3 mm, two corrections were made to the volume of lesions with adjusted volumes of 17 mm^3 ± 3 mm^3 (24 mm^3 ± 5 mm^3 without correction). In these conditions, the lesions measured by MRI at 24 hours appear to be the totality of the hypoperfused volumes measured by Ultrasensitive Doppler at 2 hours post stroke onset.

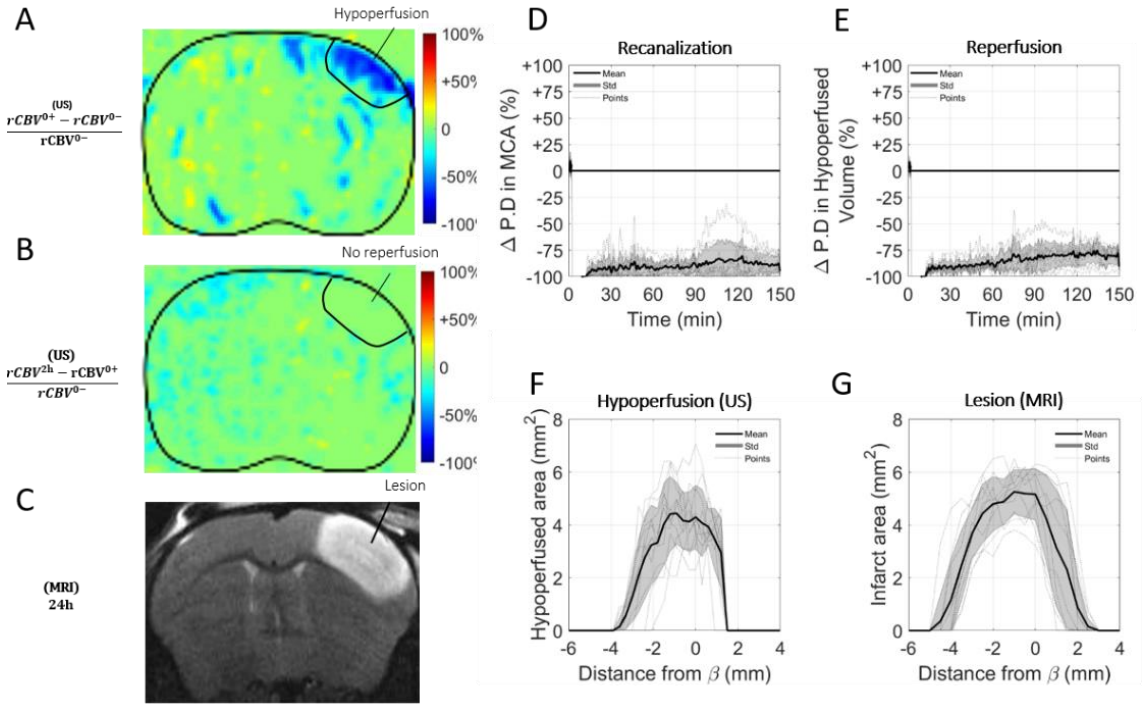

Figure 2. In the absence of treatment, no recanalization nor reperfusion is observed and the final volume of lesion corresponds to the early hypoperfused area.

A. Differences between ultrasensitive Doppler imaging performed before and after MCAo reveal hypoperfusion in the cortex. B. Differences between ultrasensitive Doppler imaging just after MCAo and 2 hours later show no sign of reperfusion. C. Corresponding MRI reveals the final ischemic lesions. D. Monitoring of blood flow in the MCA on ultrasensitive Doppler images over β+1mm show permanent occlusion. E. Monitoring of cerebral perfusion in the hypoperfused areas shows no sign of reperfusion. F. Pattern of hypoperfusion directly after MCAo revealed by ultrasensitive Doppler. G. Final ischemic lesions measured at 24 hours after MCAo revealed by MRI.

Validation on a group with permanent occlusion through electrocoagulation

This hypothesis was validated in a supplementary group of 5 mice in which the MCA has been permanently occluded through electrocoagulation thus allowing neither recanalization nor reperfusion of the tissue to happen at any time (*Figure 3*). As expected, no reperfusion was observed, and similar hypoperfused volumes were observed in Ultrasensitive Doppler imaging together with similar ischemic lesions on T_2 weighted MRI. The volumes at risk are 19 mm^3 ± 3 mm^3 while the volumes of lesion are 18 mm^3 ± 5 mm^3 (24 mm^3 ± 7 mm^3 before adjustments).

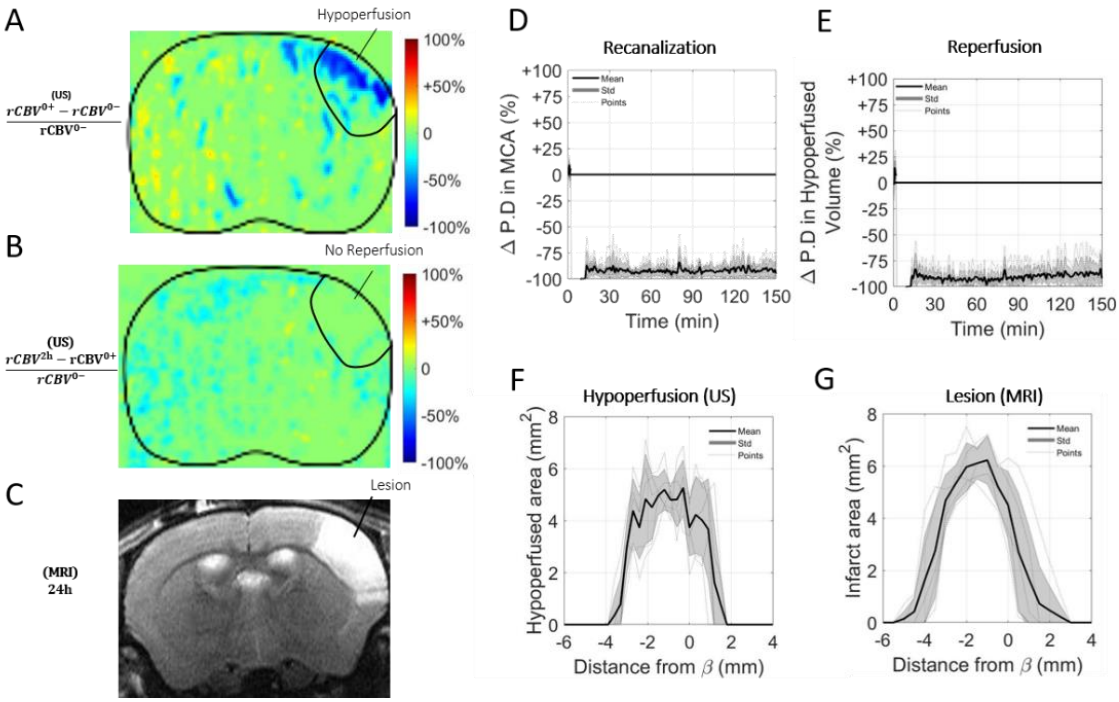

Figure 3. In a model of stroke induced by a permanent MCAo caused by electrocoagulation, no reperfusion is observed and the final volume of lesion corresponds to the early hypoperfused area.

A. Differences between ultrasensitive Doppler imaging performed before and after occlusion of the middle cerebral artery (MCAo) reveal hypoperfusion in the corresponding ipsilateral cortices. B. Differences between ultrasensitive Doppler imaging just after MCAo and 2 hours later show no sign of reperfusion in the corresponding ipsilateral cortices. C. Corresponding MRIs reveal the final ischemic lesions. D. Monitoring of blood flow in the MCA on Ultrafast Ultrasound images over β+1mm show permanent occlusion. E. Monitoring of cerebral perfusion in the hypoperfused areas shows no sign of reperfusion. F. Pattern of hypoperfusion directly after MCAo revealed by Transcranial Ultrafast Ultrasound imaging. G. Pattern of the final ischemic lesions measured at 24 hours after MCAo revealed by MRI.

rtPA induced recanalization and reperfusion can be monitored with Transcranial Ultrafast Ultrasound

In a group of 10 mice, the gold standard fibrinolytic treatment, rtPA was injected intravenously 20 minutes after occlusion of the MCA (10 % in bolus and 90% in infusion as in clinic). The differences of power Doppler images from before and after occlusion exhibit the hypoperfusion in the ipsilateral cortices (Figure 4.A) whereas the differences between just after occlusion and 2 hours after this time display the reperfused areas (Figure 4.B). The monitoring of the recanalization of the body of the MCA reveals an overall improvement in arterial recanalization (Figure 4.C). Although tissue reperfusion can be observed, it does not appear as effective as arterial recanalization (Figure 4.D).

The areas at risk in ultrasensitive Doppler were measured as previously (sham control group, Figure 2) directly after occlusion (before rtPA treatment) and reveal the same behaviors, a peak around β-1 mm and spreading between β-4 mm and further than β+1 mm with total hypoperfused volumes of 17 mm^3 ± 3 mm^3 (**Figure 4.E**). However, in agreement with an efficient recanalization-reperfusion of the ischemic brain tissue, revealed by a rescue of the CBV, the final infarct areas on T_2 weighted MRI at 24 hours are 11 mm^3 ± 3 mm^3 (14 mm^3 ± 11 mm^3 before adjustment); i.e. a reduction of about 30 % of the lesion volumes compared to the initially identified areas at risk measured just after rtPA treatment by using ultrafast ultrasound imaging (**Figure 4.F**).

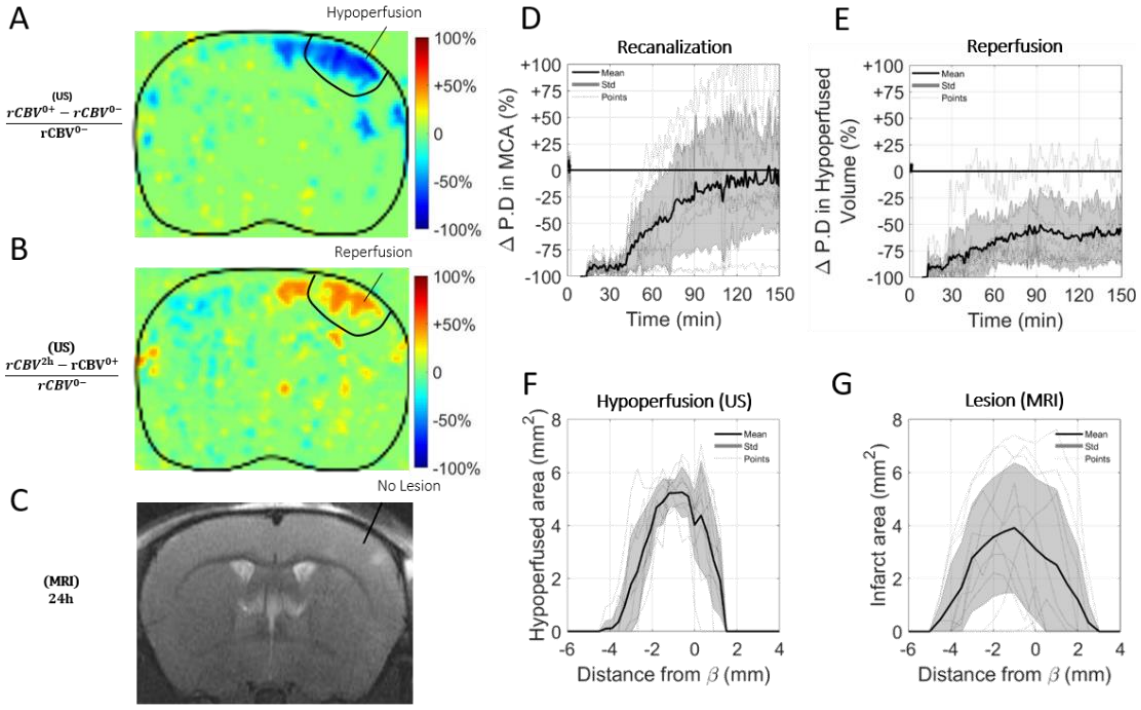

Figure 4. Injection of rtPA causes arterial recanalization, tissue reperfusion and reduces the lesion.

A. Differences between ultrasensitive Doppler before and after MCAo reveal hypoperfusion in the cortex. **B**. Differences between ultrasensitive Doppler just after MCAo and 2 hours later show reperfusion. **C**. Corresponding MRIs reveal the formation of smaller lesions. **D**. Monitoring of flow in the MCA on Ultrafast Ultrasound images over β+1mm shows rapid and effective recanalization. **E**. Monitoring of cerebral perfusion in the hypoperfused volumes show some tissue reperfusion. **F**. Pattern of hypoperfusions directly after MCAo revealed by Ultrafast Ultrasound imaging. **G**. Pattern of the ischemic lesions 24 hours after MCAo revealed by MRI in rtPA treated animals.

Ultrasensitive Doppler allows fine monitoring of blood flow after stroke and treatment

Analysis of individual animals, of the rtPA treated group, unmask fine correspondence between reperfusion patterns and volumes of lesion. In two animals, arterial recanalization was observed without any tissue reperfusion. In two other animals, complete tissue reperfusions were achieved. In the other animals, recanalization was followed by some form of incomplete reperfusions. Reperfusion profiles were reconstructed in three different coronal planes to explore spatial temporal differences in reperfusion. The mice for which arterial recanalization without reperfusion were observed exhibited similar lesions as the saline treated control mice, spreading over the whole hypoperfused volumes. In three mice, some reperfusions were achieved in the whole injured brain though the blood volumes did not come back to pre-occlusion levels (*Figure 5.A*). Corresponding lesions were reduced at the margins. For two mice, one branch of the MCA was completely reperfused while the other was not (*Figure 5.B*). It can be seen as the reperfusion in the plane β (in blue) happens in less than one hour whereas it takes one hour and half over β-2 mm (in red) and a little less than two hours over β-4 mm (in yellow). No lesion was observed in the reperfused tissues as opposed to the ones in the non reperfused tissues. In the mice with complete reperfusion, the entire cerebral perfusion was restored in the whole injured brains in less than 2 hours and almost no sign of lesion can be observed in T_2 weighted MRI (*Figure 5.C*).

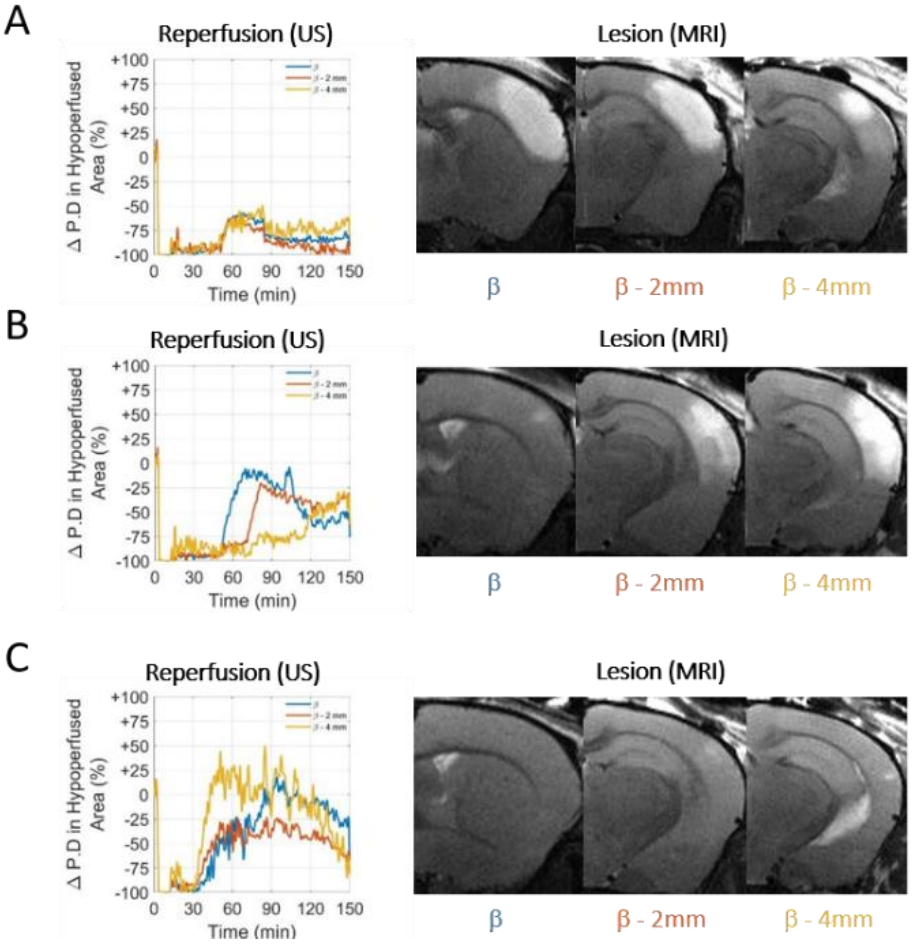

Figure 5. Differences in reperfusion revealed by ultrasensitive Doppler over three coronal planes (β in blue, β-2mm in red & β–4 mm in yellow) are correlated with lesions revealed by T_2 MRI at 24h.

A. Limited reperfusion in tissue is ineffective to save tissues. B. Effective reperfusion over the most anterior part of the lesion (blue) but not in the posterior part (yellow) causes a lesion only in the posterior part. C. Effective reperfusion prevents the formation of lesions throughout the brain.

Ultrasensitive Doppler predicts response to thrombolytic treatment and final outcome following stroke

Predicting the outcome of stroke and the resulting cognitive impairment based on early imaging would probably change medical care in stroke units. In this study, imaging hypoperfusion during the early phase of stroke and comparison with the resulting lesions indicates a match between hypoperfused areas and final lesions. The adjusted volumes of lesion can be plotted as a function of the hypoperfusion directly after the occlusion of the MCA (Figure 6.A). For the control group, the outcome of the stroke can be predicted since after adjustments all points align along the diagonal. This means that when no early reperfusion is observed, the volumes of lesion are the whole volumes at risk measured just after stroke onset. For animals receiving rtPA, the volumes of lesion are reduced, meaning that tissue areas were effectively saved. The size of the lesion depends on two factors: the initial size of the hypoperfused

zone and the efficiency of the reperfusion. When plotting the adjusted volumes of lesion as a function of the hypoperfusion at 2h after stroke onset (Figure 6.B), all points align around the diagonal. In both cases, the volumes of lesion are the hypoperfused volumes measured at 2 hours.

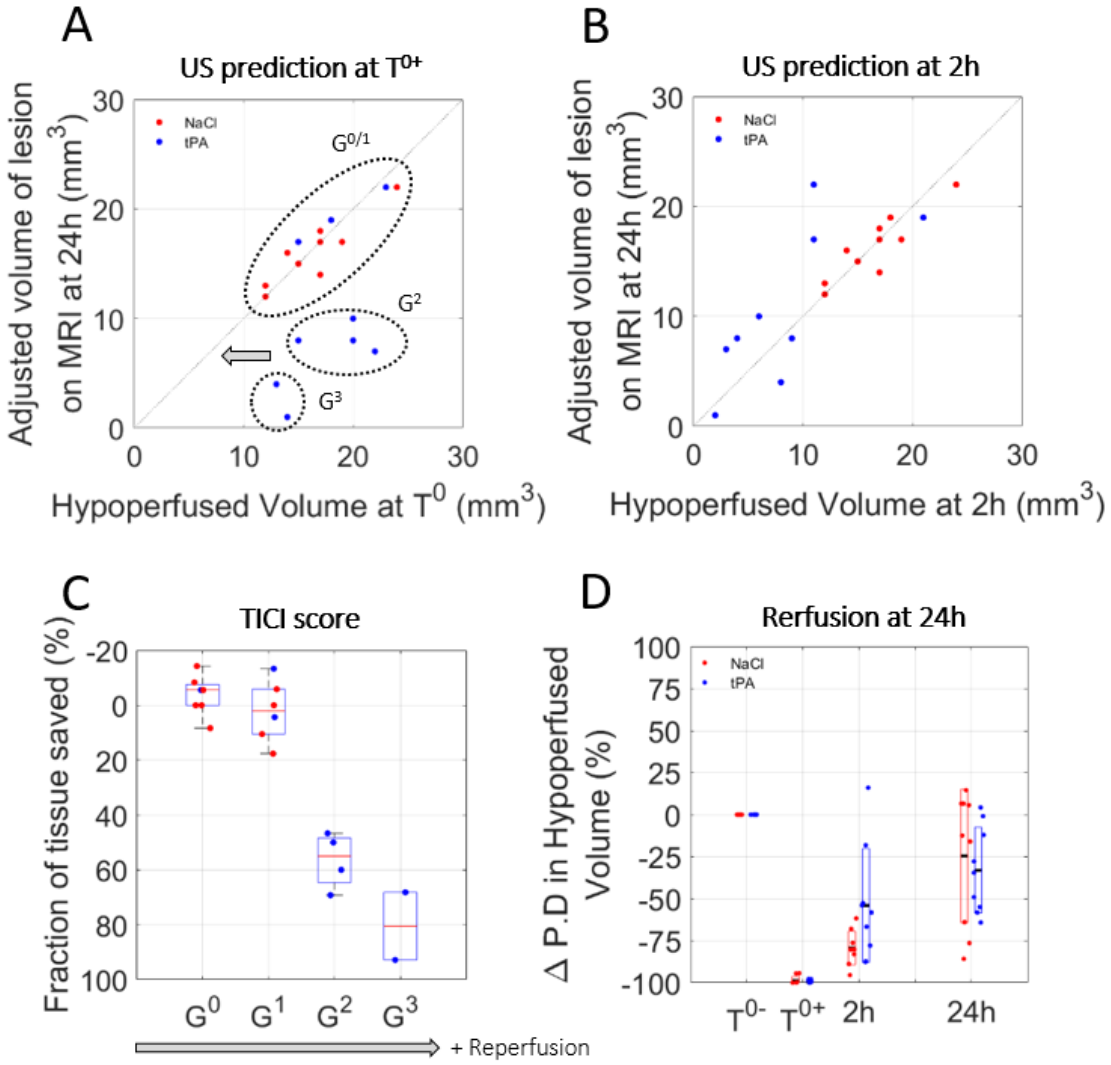

Figure 6. Prediction of lesions and responses to treatment based on early ultrasensitive Doppler

A. After MCAo, hypoperfused volume predicts final lesion volumes. For the NaCl group (red), the lesions are the hypoperfused volumes. For the rtPA group (blue), the lesions are reduced. **B**. At 2h, the remaining hypoperfused volumes are predictive of the final lesion volumes. **C**. Prediction of lesions based on the Ultrasound TICI score. **D**. Evolutions of perfusions in the volumes at risk at the early time after stroke onset (2 hours) and at 24 hours show that after a therapeutic window of 2 hours, perfusion is no longer predictive of lesion.

However, this representation does not take into account the quality of the reperfusion in saving tissues. To standardize the analysis of reperfusion, a grading system similar to the clinical Thrombolysis In Cerebral Ischemia (TICI) grading system (***Zaidat O et al 2012***) from 0 to 3 was used to describe the reperfusion, 0 being no recanalization, 1 recanalization but no reperfusion, 2 a partial reperfusion and 3 a complete reperfusion. The scoring was performed based on the ultrasensitive Doppler images. All mice in the control group are attributed to a TICI score of 0 or 1, meaning that no reperfusion was ever observed. Four mice in the rtPA treated group were attributed TICI scores of 0 or 1 meaning that thrombolysis was not effective enough to reperfuse the tissues. In these conditions, the prognostic of lesions is similar to the control saline group. Six mice in the rtPA group were attributed TICI scores of 2 or 3, meaning that reperfusions were achieved. In these conditions, the lesions were reduced compared to the volumes at risk and compared to the control group, implying that the better the reperfusion is, the more tissues are saved.

Using the Ultrafast Doppler based TICI grading system, we can represent how much tissue was effectively saved by an early and effective reperfusion compared to the initial areas at risk measured by CBV (*Figure 5.C*). It is no surprise that for grades 0 and 1, no tissue is saved. As the tissue remains hypoperfused for more than 2 hours, tissue suffering is too important to be recovered. On the contrary, major improvements can be observed for mice with grades 2 and 3 with the preservation of more than half of the tissue. All animals, whether they received saline of rtPA, show some reperfusion at 2 and 24 hours after the onset of the stroke, with an improved reperfusion for the rtPA treated animals when measured at 2 hours (*Figure 5.D*). However, this representation shows that only the reperfusion during the first 2 hours can have some positive impact on the lesion. This echoes previous finding in mice, where the restoration of blood flow only have a positive impact if it happens during the first hours after the onset of stroke (***Orset C et al 2016***). This is the analog of the therapeutic window in human patients during which thrombolysis may have a positive impact on the outcome.

Ultrasound Localization Microscopy (ULM) enhances spatial resolution to predict the ischemic lesion

Because of strong attenuation in the skull, imaging the brain with ultrasound has always been a challenge. In mice, although the skull is relatively thin, strong shadowing hinders the sensitivity and contrast. In these conditions, the distinction between reperfusion grades and sometimes identification of hypoperfused areas can be complicated. For both humans and animals, microbubbles have commonly been used as an ultrasound contrast agent for decades. More recently, ULM has been demonstrated in animals and patients and showed that microbubbles could also be used to enhance the spatial resolution (***Couture O. et al. 2018, Hingot V. et al. 2019, Heiles B. et al. 2019***).

In four mice in each group, ULM was performed in a single coronal plane at particular times, just before and after occlusion of the MCA, 1 and 2 hours later and again after 24 hours. On the given examples in *Figure 7*, although there is still strong shadowing by the skull, ULM can be performed and reveal the vasculature with enhanced spatial resolution and sensitivity. ULM reveal the localization and extent of the hypoperfusion in the NaCl group. 24 hours after the onset of the stroke, we can compare the lesions seen in T_2 weighted MRI with the hypoperfused areas.

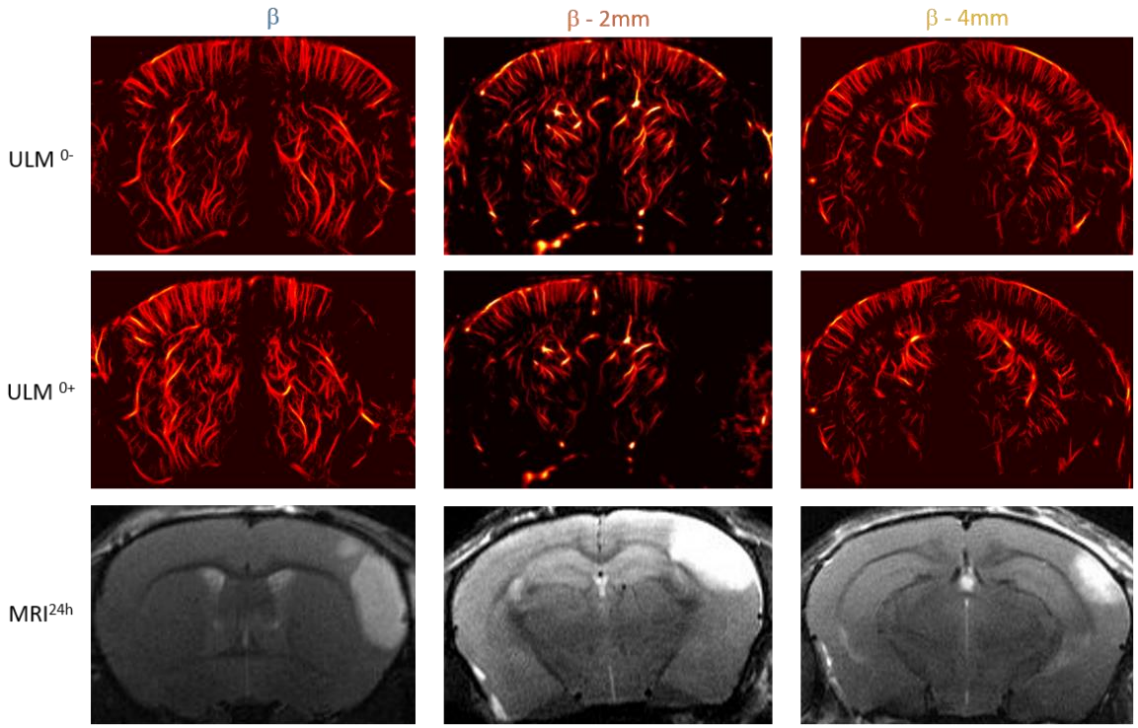

Figure 7. ULM before and after ischemia in three different NaCl treated mice revealing the areas at risk over different coronal planes (β in blue, β-2mm in red & β–4 mm in yellow) and corresponding T_2 MRI to compare with the formation of lesions.

The given example in *Figure 8.A* shows the formation of a big lesion. The hypoperfused area is large and the injection of NaCl doesn't induce efficient reperfusion. 2 hours after the onset of the ischemia, only a small area is reperfused, which we can easily identify as saved on the corresponding T_2 image. The given example in *Figure 8.B*, shows the formation of a very small lesion. The hypoperfused area is small and rtPA causes fast reperfusion. Almost no damage can be observed on the corresponding T_2 image. These two examples give an idea of how ULM could be used to predict the hypoperfused area and monitor the response to treatment and generally predict the outcome of the stroke.

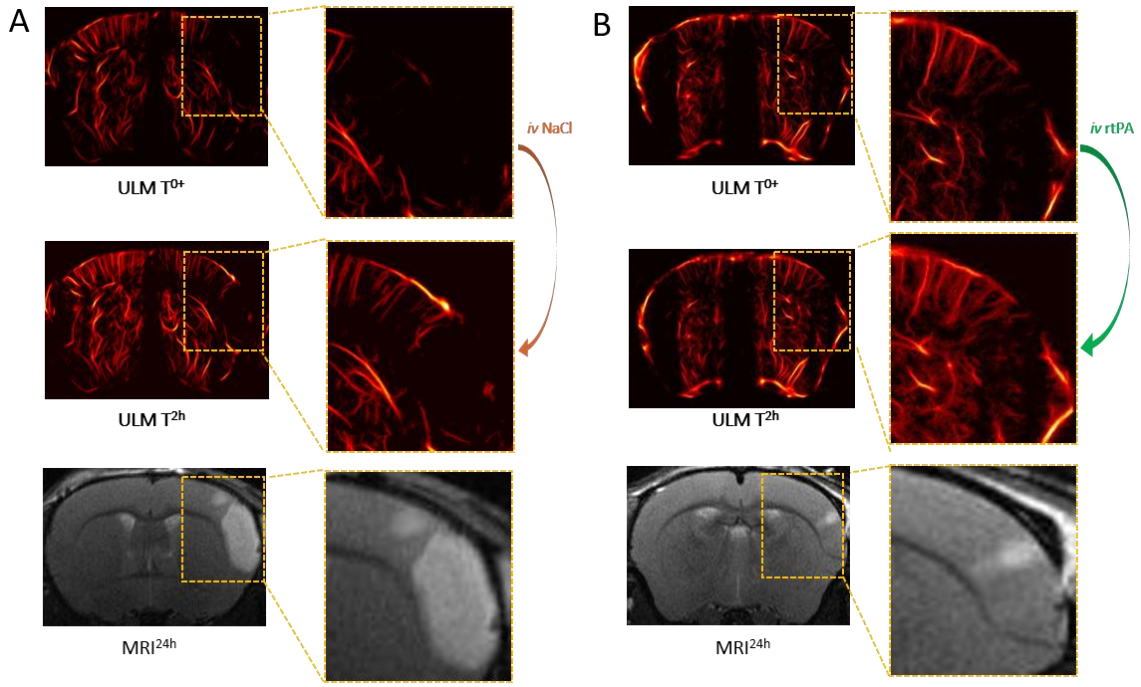

Figure 8. Predicting the outcome and evaluating response to treatment with transcranial ULM.

A. ULM on a mice treated with NaCl. A large lesion can be seen in ULM just after ischemia and very little reperfusion can be observed 2 hours after the onset. MRI. **B**. ULM on a mice treated with rtPA. A small lesion can be seen in ULM just after ischemia and is completely reperfused 2 hours after the onset. MRI reveals a small lesion.

4. Discussion

Stroke is a major healthcare problem with a high mortality rate and around 50% of survivors with long-term disability. The disease occurs when blood flow supply to an area of the brain is dramatically diminished, leading to a set of events including excitotoxic neuronal death, apoptosis and inflammatory processes. The treating physician needs to make his decision or adapt it, as rapidly as possible, based on the vascular imaging (whether or not angiography shows a large vessel occlusion), assessment of the penumbra (based on CT or MR perfusion imaging), time of stroke onset, visible clinical factors and previous history of the patient *(Zerna C. et al. 2018)*. To date, our ability to cure stroke-induced brain injuries remains limited. Everybody agrees that an important goal to improve stroke therapy is to identify not only the location but also how the lesion will extend with time after stroke onset, whether the patient will respond to treatment and ultimately to predict the functional outcome. To address these important questions, neurologists and neuroradiologists use a combination of prediction tools to try to answer, with the severity of stroke, its location into the brain, age, previous risk factors and comorbid disease (such as high blood pressure, diabetes ….) as key factors.

Despite all these criteria, their answer remains most often very evasive and is usually postponed until the evolution of permanent neurological deficits during the following 48 hours. An early blood-based biomarker to accurately identify salvageable tissues and predict functional outcome after stroke is, therefore, mandatory *(**Stinear C. M. et al. 2017**)* and could be met with the assistance of neuroimaging techniques *(**Thomalla G. et al. 2019**)*. In our study, we demonstrate that Ultrafast Ultrasound can be a relevant neuroimaging modality for stroke. In mice, no contrast agent nor skull removal is necessary to image perfusion limiting the invasiveness of the technique. Ultrafast Doppler imaging allows for continuous monitoring of brain perfusion, in 3D and during the early phase of stroke with great sensitivity, spatial and temporal resolution. More importantly, we show that early assessment of cerebral perfusion using *in vivo* Ultrafast Doppler brain imaging, when performed early after stroke onset (here 2 hours in rodents) is predictive of final lesion volumes measured by MRI at 24 hours. We also demonstrate, that when performed just after thrombolytic treatment (rtPA-induced fibrinolysis), this methodology is predictive of the response to treatment.

However, the translation of results to humans should always be done carefully, especially in the context of stroke. Animal models of stroke have been used to gain an understanding of the pathophysiology of the disease, unfortunately, all strategies identified to save the brain excepted rtPA treatment have failed in the clinic, mainly because of poor animal modeling. The model of stroke we have used in the present study *(**Orset C. et al. 2007, Orset C. et al. 2016**)* is highly relevant to the actual clinical setting. It consists of a clot induced *in situ* in the middle cerebral artery of mice, by local injection of the pro-coagulant compound thrombin, a stroke model responsive to rtPA-induced thrombolysis when injected intravenously, 10 % in bolus – 90% in infusion as in clinic *(**Orset C. et al. 2016**)*. We also reported a 90 minutes therapeutic window for this model, in a multicentric preclinical study *(**Orset C. et al. 2016**)*.

In Humans, a meta-analysis of 53 studies encompassing 2066 patients reported a strong association of recanalization with the good functional outcome (OR 4.43, 95% CI 3.32 to 5.91), and reduced mortality (OR 0.24, 95% CI 0.16 to 0.35) at 3 months in acute ischemic stroke. In this study, the authors have classified patients between those with spontaneous recanalization, intravenous (IV) fibrinolytic or intra-arterial (IA) fibrinolytic treatments, combined IV and IA thrombolysis or mechanical thrombectomy with rates of recanalization of 24.1, 46.2, 63.2, 67.5, 83.6%, respectively *(**Zaidat O et al 2012**)*. The current consensus is that recanalization and more precisely tissue perfusion is directly associated with favorable clinical outcome and survival after acute ischemic stroke *(**Campbell B. C. V. et al. 2019, Thomalla G. et al. 2019**)*.

Today, intravenous thrombolysis with recombinant tissue type plasminogen activator (rtPA, Alteplase) and endovascular clot removal are the two gold standards of care in stroke therapy. The therapeutic window for rtPA treatment is 4.5 hours after stroke onset, possibly extended to 9 hours based on the more recent clinical trials published *(**Ma H. et al. 2019**)*. Using MR-imaging based selection of acute ischemic stroke patients with a proximal occlusion and a significant hypoperfused but not dead brain region, the time window of mechanical thrombectomy may extend to 24 h (or beyond) since symptom onset, combined with rtPA treatment *(**Nogueira R. G. et al. 2018**)*. Nonetheless, too many patients are excluded from rtPA infusion because of this limited 4.5-hour time window. With the recommendations, which suggest a therapeutic window of 6 hours to start rtPA, less than 10% of stroke patients can benefit the combination between rtPA and endovascular thrombectomy.

It is well admitted that advanced imaging-based approaches to select appropriate patients, should widen the time-window for patient selection and would contribute to more efficient recanalization-reperfusion strategies and thus improved clinical outcomes. The current consensus is that no imaging method alone could provide sufficient information. Arterial spin labeling (ASL) *(**Zaharchuk G. et al. 2014**)* is an MRI method that enables the measurement of tissue perfusion without the use of exogenous contrast agents, by magnetically tagging the water in inflowing blood, with development ongoing to increase imaging speed and image quality *(**Veclytte S. et al. 2017**)*. ASL is perhaps the most promising methods but cannot be used in routine because of the acquisition time and limited access to the MR machines.

The possibility to have access to an easy to use, cheap, portable machine to image cerebral perfusion would undoubtedly help to increase the number of patients eligible to treatment, without forgetting the possibility to use this imaging method directly in the ambulance. Although recanalization is associated with rapid clinical improvement in some patients, for others despite recanalization of the occluded artery they show delayed or impaired reperfusion. Ideal patient selection for thrombolysis alone or combined to thrombectomy should therefore not be based on therapeutic windows but rather on perfusion imaging to determine “a signature” of response to treatments.

Unlike other vascular imaging such as CT-angiography or MR-Angiography, Ultrafast Ultrasound is an easy to use and transportable setup, which could be compatible with long term recording of whole brain cerebral perfusion of stroke patients as early as in the ambulance. Such type of monitoring could be very useful to monitor recovery, to prevent and treat recurrent stroke and eventually to anticipate delayed effects.

There are clear limitations about the possibility to use Ultrafast Doppler Ultrasound *in vivo* in humans due to strong aberrations and absorption of the skull. However, the use of microbubbles could allow to perform whole brain real time imaging of the cerebral blood flow with Ultrasound Localization Microscopy, which improves SNR and resolution. Microbubbles are ultrasonic contrast agents which are already available on the market and commonly used in Humans (Sonovue, Bracco), a major point considering the recent report made by the Food and Drug Administration (FDA) about a Safety Announcement related to gadolinium-based contrast agents (GBCAs) administered for MRIs ***(Levine D et al 2018)***.

5. Conclusion

In conclusion, we provide here, in a relevant model of thromboembolic stroke model in mice with rtPA treatment, the demonstration that Ultrafast Ultrasound *in vivo* imaging can be used in the context of stroke to diagnose ischemic injury, to prognose outcome and response to treatment, in an early time frame after stroke onset or treatment compatible to the clinical time for decision making. We think that this methodology is also highly promising for translation to the clinic, especially in combination with microbubbles, allowing neurologists and radiologists to better cure stroke patients in the future.

This study of cerebral ischemia in mice using ULM will prepare the translation of ULM to stroke patients. One future step is the replication of this study in animals with thicker skulls to test ULM performances in real situations. Using attenuation models in bones, our calculations showed that MB detection should be possible through the rat's skull with a 9 MHz probe and through a human skull using a 1.25 MHz probe. Two 3D multiplexed probes were designed specifically to perform the proof of concept in rat's first, then in sheep and humans. Preliminary work from Arthur Chavignon showed that ULM could indeed be performed in 3D and through a rat's skull in these conditions. Hopefully, the proof of concept for ULM in 3D through a human skull could be performed in the coming years.

In the meantime, the setup I developed to characterize cerebral perfusion during stroke in mice will be a valuable tool for physiologists to test new drugs and new strategies with a complete and quantitative understanding of vascular flows during ischemia and reperfusion. This opens the door for finer physiological studies and a better translation of these strategies to human patients.

6. References

- J. Zivin, et al, Tissue plasminogen activator reduces neurological damage after cerebral embolism, *Science* **230**, 1289–1292 (1985).

- B. C. V. Campbell et al, Extending thrombolysis to 4·5–9 h and wake-up stroke using perfusion imaging: a systematic review and meta-analysis of individual patient data, *The Lancet* (2019), doi:10.1016/S0140-6736(19)31053-0.

- O. A. Berkhemer, et al, A Randomized Trial of Intraarterial Treatment for Acute Ischemic Stroke, *N. Engl. J. Med.* **372**, 11–20 (2015).

- J. M. Coutinho, et al, Combined Intravenous Thrombolysis and Thrombectomy vs Thrombectomy Alone for Acute Ischemic Stroke: A Pooled Analysis of the SWIFT and STAR Studies, *JAMA Neurol.* **74**, 268 (2017).

- R. G. Nogueira, et al, Thrombectomy 6 to 24 Hours after Stroke with a Mismatch between Deficit and Infarct, *N. Engl. J. Med.* **378**, 11–21 (2018).

- A. M. Thiebaut, et al, The role of plasminogen activators in stroke treatment: fibrinolysis and beyond, *Lancet Neurol.* **17**, 1121–1132 (2018).

- M. Wintermark, et al, Comparative Overview of Brain Perfusion Imaging Techniques, *Stroke* **36** (2005), doi:10.1161/01.STR.0000177884.72657.8b.

- M. Essig, et al, Perfusion MRI: The Five Most Frequently Asked Technical Questions, *Am. J. Roentgenol.* **200**, 24–34 (2013).

- Q. Shen, T. Duong, Magnetic resonance imaging of cerebral blood flow in animal stroke models, *Brain Circ.* **2**, 20 (2016).

- M. Tanter, M. Fink, Ultrafast imaging in biomedical ultrasound, *IEEE Trans. Ultrason. Ferroelectr. Freq. Control* **61**, 102–119 (2014).

- T. Deffieux, et al, Functional ultrasound neuroimaging: a review of the preclinical and clinical state of the art, *Curr. Opin. Neurobiol.* **50**, 128–135 (2018).

- E. Macé, et al, Functional ultrasound imaging of the brain, *Nat. Methods* **8**, 662–664 (2011).

- C. Demené, et al, 4D microvascular imaging based on ultrafast Doppler tomography, *NeuroImage* **127**, 472–483 (2016).

- E. Tiran, et al, Transcranial Functional Ultrasound Imaging in Freely Moving Awake Mice and Anesthetized Young Rats without Contrast Agent, *Ultrasound Med. Biol.* **43**, 1679–1689 (2017).

- C. Demene, et al, Functional ultrasound imaging of brain activity in human newborns, *Sci. Transl. Med.* **9**, eaah6756 (2017).

- M. Imbault, et al, Intraoperative Functional Ultrasound Imaging of Human Brain Activity, *Sci. Rep.* **7** (2017), doi:10.1038/s41598-017-06474-8.

- C. Errico, et al, Ultrafast ultrasound localization microscopy for deep super-resolution vascular imaging, *Nature* **527**, 499–502 (2015).

- O. Couture, et al, Ultrasound Localization Microscopy and Super-Resolution: A State of the Art, *IEEE Trans. Ultrason. Ferroelectr. Freq. Control* **65**, 1304–1320 (2018).

- J. Baranger, et al, Adaptive Spatiotemporal SVD Clutter Filtering for Ultrafast Doppler Imaging Using Similarity of Spatial Singular Vectors, *IEEE Trans. Med. Imaging* **37**, 1574–1586 (2018).

- V. Hingot, et al, Microvascular flow dictates the compromise between spatial resolution and acquisition time in Ultrasound Localization Microscopy, *Sci. Rep.* **9** (2019), doi:10.1038/s41598-018-38349-x.

- B. Heiles, et al,, Ultrafast 3D Ultrasound Localization Microscopy using a 32×32 Matrix Array, *IEEE Trans. Med. Imaging* , 1–1 (2019).

- A. Martín,.et al, Imaging of Perfusion, Angiogenesis, and Tissue Elasticity after Stroke, *Journal of Cerebral Blood Flow & Metabolism* **32**, 1496–1507 (2012).

- A. Martín et al, Imaging of Perfusion, Angiogenesis, and Tissue Elasticity after Stroke, Journal of Cerebral Blood Flow & Metabolism 32, 1496–1507 (2012).

- C. Brunner, et al, Mapping the dynamics of brain perfusion using functional ultrasound in a rat model of transient middle cerebral artery occlusion, *J. Cereb. Blood Flow Metab.* **37**, 263–276 (2017).

- C. Brunner, et al, Evidence from functional ultrasound imaging of enhanced contralesional microvascular response to somatosensory stimulation in acute middle cerebral artery occlusion/reperfusion in rats: A marker of ultra-early network reorganization?, *J. Cereb. Blood Flow Metab.* **38**, 1690–1700 (2018).

- G. Llovera, et al, Results of a preclinical randomized controlled multicenter trial (pRCT): Anti-CD49d treatment for acute brain ischemia, *Sci. Transl. Med.* **7**, 299ra121-299ra121 (2015).

- C. Orset, et al, Mouse Model of In Situ Thromboembolic Stroke and Reperfusion, *Stroke* **38**, 2771–2778 (2007).

- C. Orset, et al, Efficacy of Alteplase in a Mouse Model of Acute Ischemic Stroke: A Retrospective Pooled Analysis, *Stroke* **47**, 1312–1318 (2016).

- J. Bercoff, et al, Ultrafast compound doppler imaging: providing full blood flow characterization, *IEEE Transactions on Ultrasonics, Ferroelectrics, and Frequency Control* **58**, 134–147 (2011).

- S. Martinez de Lizarrondo, et al, Potent Thrombolytic Effect of *N* -Acetylcysteine on Arterial Thrombi, *Circulation* **136**, 646–660 (2017).

- C. Demene, et al, Spatiotemporal Clutter Filtering of Ultrafast Ultrasound Data Highly Increases Doppler and fUltrasound Sensitivity, *IEEE Trans. Med. Imaging* **34**, 2271–2285 (2015).

- O. O. Zaidat, et al, Revascularization grading in endovascular acute ischemic stroke therapy, *Neurology* **79**, S110–S116 (2012).

- K. K. Shung, R. A. Sigelmann, J. M. Reid, Scattering of Ultrasound by Blood, *IEEE Transactions on Biomedical Engineering* **BME-23**, 460–467 (1976).

- G. Cloutier, Z. Qin, Ultrasound backscattering from non-aggregating and aggregating erythrocytes—A review, *Biorheology* **34**, 443–470 (1997).

- C. Zerna, et al, Current practice and future directions in the diagnosis and acute treatment of ischaemic stroke, *The Lancet* **392**, 1247–1256 (2018).

- C. M. Stinear, Prediction of motor recovery after stroke: advances in biomarkers, *Lancet Neurol.* **16**, 826–836 (2017).

- G. Thomalla, C. Gerloff, Acute imaging for evidence-based treatment of ischemic stroke:, *Curr. Opin. Neurol.* , 1 (2019).

- E. A. Mistry,et al, Mechanical Thrombectomy Outcomes With and Without Intravenous Thrombolysis in Stroke Patients: A Meta-Analysis, *Stroke* **48**, 2450–2456 (2017).

- H. Ma,et al, Thrombolysis Guided by Perfusion Imaging up to 9 Hours after Onset of Stroke, *N. Engl. J. Med.* **380**, 1795–1803 (2019).

- G. Zaharchuk, Arterial Spin–Labeled Perfusion Imaging in Acute Ischemic Stroke, *Stroke* **45**, 1202–1207 (2014).

- S. Verclytte, et al, ASL and susceptibility-weighted imaging contribution to the management of acute ischaemic stroke, *Insights Imaging* **8**, 91–100 (2017).

- D. Levine, et al, Gadolinium Retention After Contrast-Enhanced MRI, *JAMA* **320**, 1853 (2018).

Chapter 6: Ultrasound Localization Microscopy and functional Ultrasound

1. Functional ultrasound

Functional ultrasound (fUS) is a recently introduced imaging strategy to image brain function. It is an analog of functional MRI and image the hemodynamic fluctuations associated with neural function. It is a not a direct functional imaging since it doesn't image neural activity, but rely on neurovascular coupling. It has been demonstrated in various animal models (***Mace E et al 2013***, ***Tiran E et al 2018***, ***Deffieux T et al 2018 Rabut C et al 2019***) but also in newborns (***Demene C et al 2016***, ***Baranger J et al 2018***) and intra operatively (***Imbault M et al 2016***). Unlike MRI, the spatio-temporal resolution and sensitivity of ultrasound allows a finer monitoring of hemodynamic fluctuations.

In this Chapter, I will give an example of how fUS can be used to study the effect of a molecule involved in neurovascular coupling. However, because the resolution of fUS is limited by the diffraction limit, it only provides general information on hemodynamic fluctuations. I will discuss the possibility to use concurrently ULM and fUS in two models where blood flow and structures are related to the function of an organ. Finally, I will discuss an attempt to perform functional imaging using ULM and compare it with the acquisition times required depending on the size of the vessel that I discussed in *Chapter 3*.

2. Functional Ultrasound in tPA deficient mice

rtPA is the gold standard treatment for ischemic stroke (***Zivin J et al. 1985, Thiebault A et al. 2018***). It is a fundamental player in the complex coagulation regulation as it triggers the dissolution of fibrin clots. It also happens to be involved in neurovascular coupling. My collaborators in Caen, Cyrille Orset, Denis Viven and Antoine Anfray demonstrated its impact using various imaging methods. Because we started working together, it became obvious than functional ultrasound could further illustrate their work. The objective of the study was to measure the difference in the evoked response and the effect of vascular rtPA. In rtPA deficient mice, we measured the increase in blood supply during mechanical stimulation of the whiskers. We repeated the operation 20 minutes after intravenous injection of rtPA in the same mouse and in the same imaging plane. A comparison of the increase in Doppler intensity indicates that rtPA deficiency mouse exhibited a lower response during whisker stimulation. A significative increase in activation was observed after injection of vascular rtPA thus confirming the hypothesis that rtPA is affecting neurovascular coupling. Although I didn't design the experiment, I did all the ultrasound acquisition and processing which brought more strength to the study. My contribution to this work can be summed up by the following Figure 1. This work was published in 2019 *(**A. Anfray et al 2019**).*

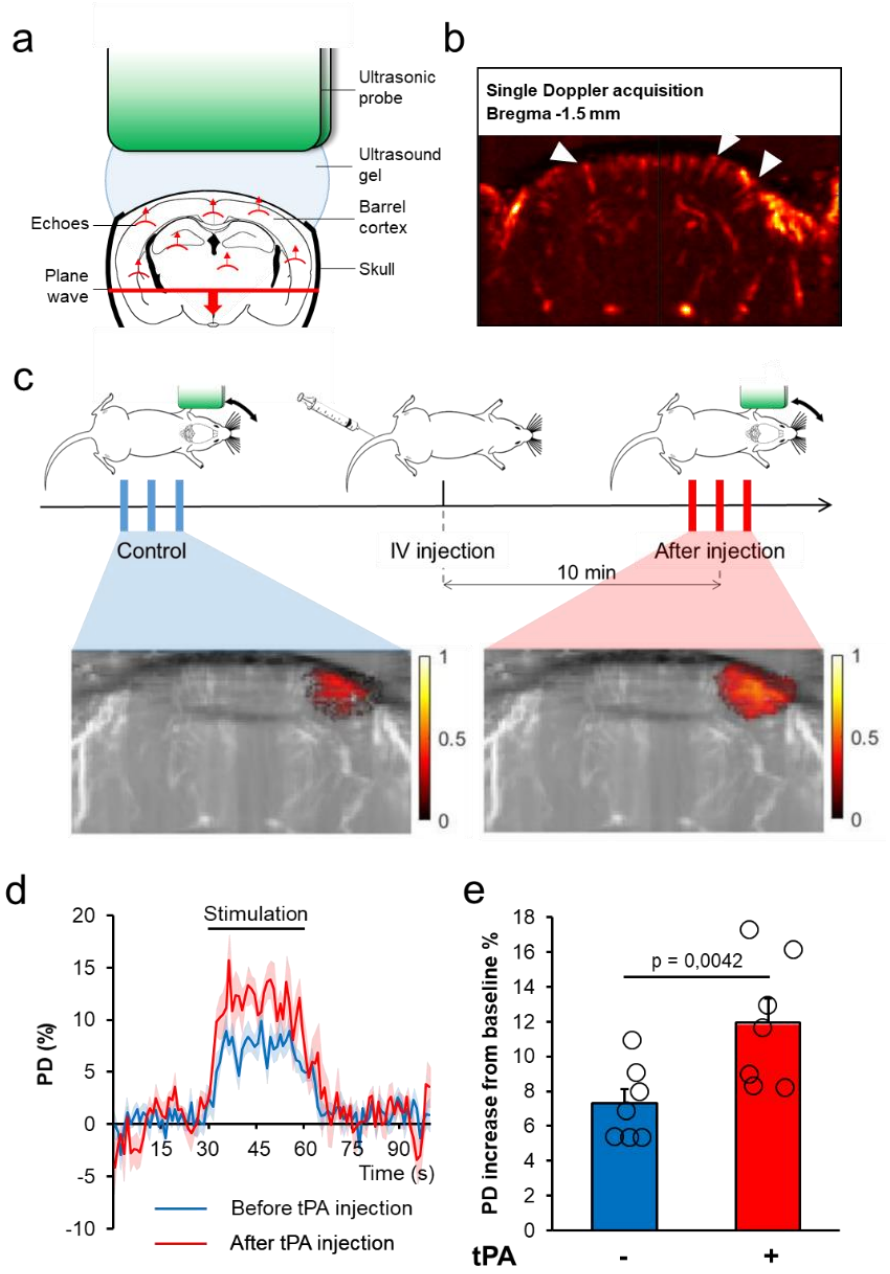

Figure 1: The promotion of the functional hyperemia by tPA is not restricted to the surface of the brain but involved the whole cortex.

A. Schematic of fUS. B. Ultrasensitive Doppler image of the brain of a C57BL/6 mouse through a thinned skull window. C. Schematic representation of the experimental timeline. D. Quantification of the relative P.D intensity increase in the activated area during whiskers stimulation in $tPA^{-/-}$ mice (Mean ± SEM, Wilcoxon test, n=7). E. Relative augmentation of the PD during whiskers stimulation before (–) or after (–) intravenous injection of tPA (n=7) in the activated area.

3. Concurrent fUS and ULM in the rat's spinal cord

The spinal cord is the link between the nervous system and the brain. It is among other things involved in transmitting painful information to the brain. Painful stimulation causes neuronal information to go up the spinal cord to the brain and like the brain when performing a cognitive task, it requires an increase in blood supply. In the brain, functional ultrasound (fUS) have shown in several situations how it could map the brain activity by monitoring hemodynamic fluctuations (***Mace E et al 2013, Deffieux T et al 2018***). fUS is performed by acquiring repeated ultrasensitive Doppler images and correlating temporal signals in each pixels with the temporal pattern of the external stimulus. In a study conducted by Julien Claron and Dr. Sophie Pezet, it was shown that fUS was also able to monitor hemodynamic fluctuations in the spinal cord during painful stimulus. The spatial resolution of ultrasensitive Doppler in these conditions is 100 µm (*Figure 2.A, Figure 2.D*). This is larger than the larger arterioles involved in supplying the spinal cord with blood. To understand which structures where responsible for the increased blood supply, we performed fUS and ULM concurrently (*Figure 2.C, Figure 2.E*). This enabled a fine quantification of the blood flows in the spinal cord. Histology with vessels staining was also performed and provided useful insight on the level of details that could be attained with ULM (*Figure 2.D, Figure 2.F*). Moreover, we could measure blood velocities in the main spinal structures (*Figure 2.G*).

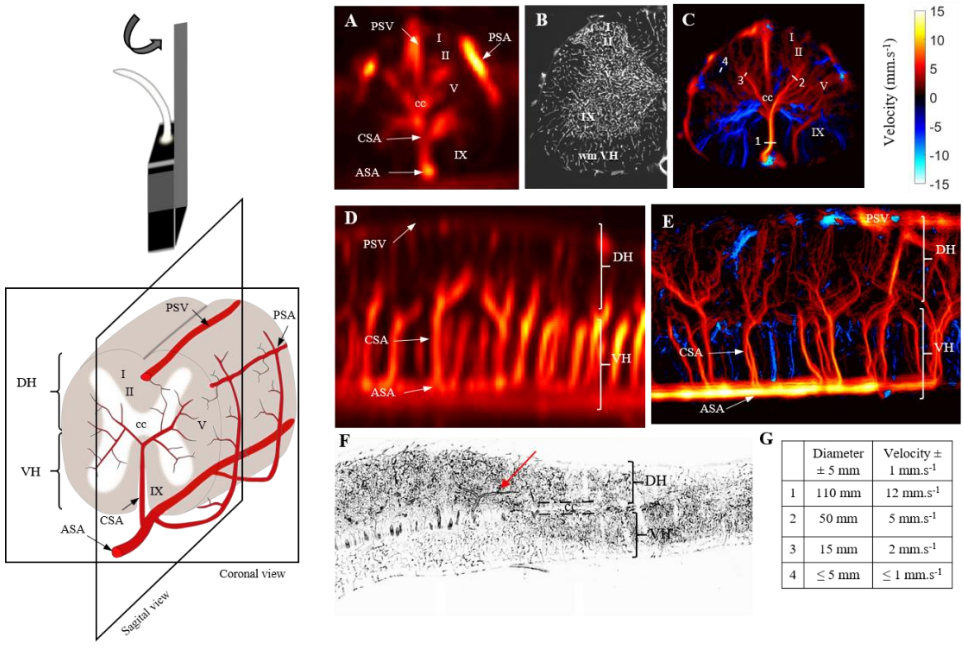

Figure 2: Vascular organization in the rat's spinal cord using ultrafast Doppler, ULM and histology

Ultrafast Ultrasound over the spinal cord. **A**. Ultrasensitive Doppler over a coronal plane. **B**. Histology over a coronal plane. **C**. ULM over a coronal plane. **D**. Ultrasensitive Doppler over a sagittal plane. **E**. ULM over a sagittal plane. **F**. Histology over a sagittal plane. **G**. Vascular quantification using ULM.

4. Explore pancreatic function with fUS and ULM

The major health issue of the century are cancer, cardiovascular diseases, stroke, and diabetes (***WHO, 2014***). Diabetes is the generic term for lack of glycemic regulation and can be of two types. The regulation of glycaemia is done by Langerhans islets which are insulin producing cells. Type 1 diabetes is caused by the destruction of these cells, often by auto immune reaction, whereas type 2 diabetes is more common and is caused by chronic habituation to high blood level often caused by high sugar consumption. The diagnostic of diabetes is based on symptoms mainly high blood sugar and confirmed by a blood test. It is thought that similarly to the brain, the activity of Langerhans islets should be accompanied by increased blood supply. Old studies using microspheres as post mortem markers of blood flow showed that pancreatic blood flow did increase following a provoked hyperglycemia (***Goodhead B et al 1970***). A more recent study using CEUS to estimate perfusion showed similar results (***St Clair J et al 2018***). The objective of this project was to use ultrasensitive Doppler and ULM to investigate how blood flow was affected by provoked hyperglycemia. In particular how ULM could image Langerhans islets which spherical organization of capillaries responsible for 20% of pancreatic blood flow (***Fossati P et al 2004***).

The following work has been done in collaboration with a team of pancreas specialist in Institut Cochin in Paris (Raphael Scharfmann) and surgeons from Hopital Necker (Carmen Capito, Pauline Lopez). I was in charge of the imaging part of the project. At first, we tried to adapt the experimental protocol for these studies in naïve rats, where hyperemia was caused by the injection of glucose in anesthetized animals. Ultrasensitive Doppler was performed longitudinally over the exposed pancreas (*Figure 4.A*). Another objective of the study was to highlight pancreatic function through the detection and observation of the Langerhans islets using ULM. Those islets are spherical organization of capillary vessels with an average diameter of around 100 μm. ULM was performed over exposed rat's pancreas and motions were corrected. However, the smallest vessels were hard to image because of remaining motion artefacts (*Figure 4.B*). Moreover, the small size of the vessels in Langerhans islets might not allow MB to effectively pass in them, and make them not imageable in ULM.

Our first experiments were done with ketamine anesthesia and intravenous injection of glucose while measuring the glycaemia every 10 minutes. The first observation we did showed that blood flow quickly increased after intravenous injection. However, it was unlikely that the increase was caused by pancreatic functions rather than because of increased blood pressure. We confirmed it by longitudinal measurements of arterial pressure.

Moreover, ketamine anesthesia was a natural provoker of hyper glycaemia, which didn't allow a proper baseline glucose level to be established and had to, therefore, be changed. Moreover, during these experiments, we observed strong vascular oscillations at 0.1 Hz that are normally observed in the brain. Their cause and mechanisms are still unclear but they are thought to be associated with high blood pressure and increased by ketamine anesthesia (*Julien C et al 2006*). Though it is an interesting phenomenon in itself, it affects the reading of small fluctuations that would be associated with the endocrine function.

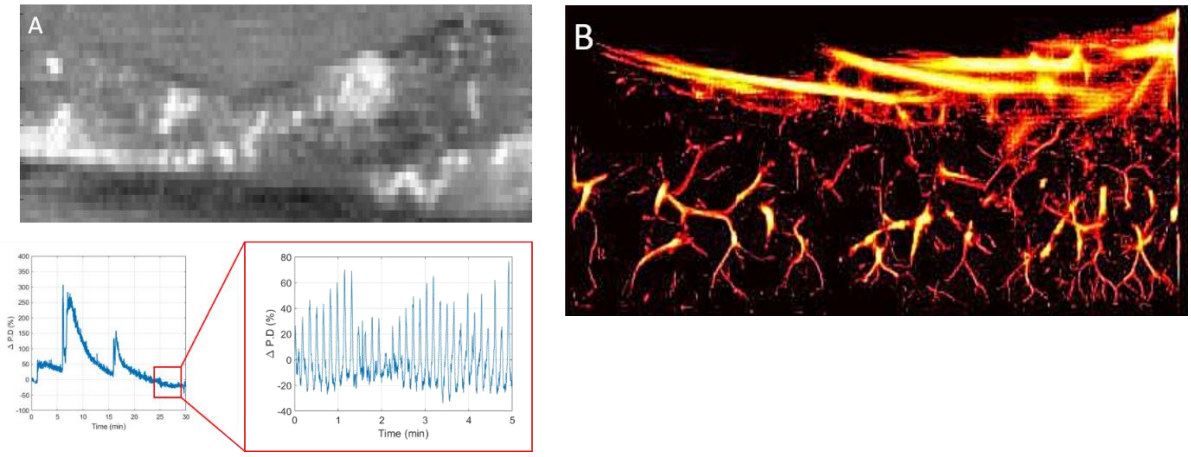

Figure 3: Pancreatic blood flows vary a lot but not only because of hyperglycemia

A. Ultrasensitive Doppler image over an exposed rat's pancreas. Fluctuation of blood flow after intravenous injection of glucose under ketamine/Dormitor anesthesia. It also reveals strong Mayer waves. B. ULM not over the same plane of pancreas.

Eventually, we had to rethink the whole experimental plan and switch to isoflurane anesthesia and intraperitoneal injection of glucose. New experiments have been performed and will be analyzed in the following weeks. Because the diagnostic of diabetes is not challenging in itself, there is little chance that even if we manage to develop a functional imaging of the pancreas, it will not replace current methods but should provide a better understanding of the link between diabetes and blood flow (*Almaça J et al. 2018*). However, the imaging of Langerhans islets would really be interesting to grade the gravity of type 1 diabetes. More importantly, ultrasensitive Doppler and ULM could enable a better imaging of infantile hyper insulinisms, which are cancers causing an abnormal quantity of insulin to be secreted by the pancreas leading to severe conditions in newborns.

5. Introduce super-resolution in functional imaging

Intravital microscopy has a far better resolution than MRI and ultrasound imaging. Its field of view is however limited to the surface of the brain. It can image individual dilatation of capillaries and arterioles (***Lecocq J et al, 2011***). ULM showed to be able to improve the spatial resolution for ultrasound imaging to the scale of 10 μm which is the size of the smallest arterioles and mark the limit with capillaries. The objective of this project was to adapt ULM to functional imaging. However, despite many attempts, the temporal resolution of ULM remained too low to follow the small hemodynamics fluctuations during whisker stimulation. We did see a slight increase in MB supply in the cortical region associated with whisker stimulation although with lower sensitivity than Doppler.

Eventually, we took some time to characterize the acquisition time required to reconstruct vessels in ULM to come to the conclusion that the experimental conditions in which the experiments should be performed to succeed where just too drastic. To reconstruct our signature image in the rat's brain, 4 minutes of acquisition was required with an injection of MB at 0.8 ml.kg which is already 15 times the recommended dose. In these conditions, vessels below 50 μm took at least a minute to be reconstructed with a minimal amount of MB. To see fluctuation of blood supply of 10-20% with a strong statistical correlation, it would take a lot longer than a few minutes, and possibly a lot more in smaller vessels. I estimate it would take about an hour of injection with similar rates to really perform the experiment. This proved to be too challenging for the time I could reasonably spend on it.

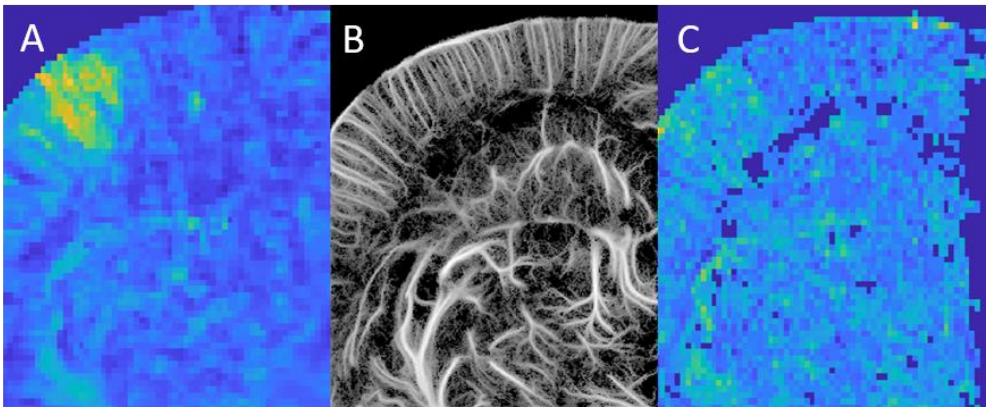

Figure 4: Functional ULM is difficult

A. Correlation map on ultrasensitive Doppler with the injection of contrast agents. **B**. ULM image reconstructed during this injection of contrast agents. **C**. Correlation map on the density of MB during rest and stimulation pattern.

6. Conclusion

The importance of ultrasound in neuroimaging is likely to grow in the coming years. The sensitivity and both spatial and temporal resolution of fUS can in some situations be similar to better than fMRI for a much cheaper system. However, except in mice or newborn rats (***Tiran E et al 2017***), fUS imaging requires partial or complete removal of the skull or the injection of contrast agents (***Errico C et al 2015***). In any case, the spatial resolution for in depth imaging remains bound by diffraction to several tens of μm.

Performing concurrent ULM can bring a fine understanding of the underlying microvasculature and enhance the interpretation of fUS imaging. However, to combine the two techniques in a single functional and super resolution imaging method proved too challenging because of the long acquisition times and high MB doses required to ensure proper separation of MB echoes. In theory, this experiment could work but should take tens of minutes and probably hours of constant and stable injection of MB together with a stable baseline for cerebral blood flow.

7. References

- Lecoq J, Parpaleix A, Roussakis E, Ducros M, Goulam Houssen Y, Vinogradov SA, Charpak S. Simultaneous two-photon imaging of oxygen and blood flow in deep cerebral vessels. *Nature Medicine*. 17: 893-8. PMID 21642977 DOI: 10.1038/nm.2394
- Pierre Fossati, « Édouard Laguesse à Lille en 1893 crée le terme “endocrine” et ouvre l'ère de l'endocrinologie. Son modèle: l'îlot endocrine du pancréas et le diabète. », Histoire des sciences médicales, 2004, 38 (4), pp. 433-440
- T. Deffieux, et al, Functional ultrasound neuroimaging: a review of the preclinical and clinical state of the art, *Curr. Opin. Neurobiol.* **50**, 128–135 (2018).
- E. Macé, et al, Functional ultrasound imaging of the brain, *Nat. Methods* **8**, 662–664 (2011).
- C. Demené, et al, 4D microvascular imaging based on ultrafast Doppler tomography, *NeuroImage* **127**, 472–483 (2016).
- E. Tiran, et al, Transcranial Functional Ultrasound Imaging in Freely Moving Awake Mice and Anesthetized Young Rats without Contrast Agent, *Ultrasound Med. Biol.* **43**, 1679–1689 (2017).
- C. Demene, et al, Functional ultrasound imaging of brain activity in human newborns, *Sci. Transl. Med.* **9**, eaah6756 (2017).

- M. Imbault, et al, Intraoperative Functional Ultrasound Imaging of Human Brain Activity, *Sci. Rep.* **7** (2017), doi:10.1038/s41598-017-06474-8.
- Rabut C, Correia M, Finel V, Pezet S, Pernot M, Deffieux T*, Tanter M*. 4D functional ultrasound imaging of whole-brain activity in rodents. *Nature Methods*
- Zivin, J. A., Fisher, M., DeGirolami, U., Hemenway, C. C. & Stashak, J. A. Tissue plasminogen activator reduces neurological damage after cerebral embolism. Science **230**, 1289–1292 (1985).
- Thiebaut, A. M. et al. The role of plasminogen activators in stroke treatment: fibrinolysis and beyond. The Lancet Neurology **17**, 1121–1132 (2018).
- Goodhead B, Himal HS, Zanbilowicz J. Relationship between pancreatic secretion and pancreatic blood flow. *Gut*. 1970;11(1):62–68. doi:10.1136/gut.11.1.62
- St Clair JR, Ramirez D, Passman S, Benninger RKP. Contrast-enhanced ultrasound measurement of pancreatic blood flow dynamics predicts type 1 diabetes progression in preclinical models. *Nat Commun*. 2018;9(1):1742. Published 2018 May 1. doi:10.1038/s41467-018-03953-y*Fossati P et al 2004*
- Claude Julien, The enigma of Mayer waves: Facts and models, *Cardiovascular Research*, Volume 70, Issue 1, April 2006, Pages 121
- Almaça J, Weitz J, Rodriguez-Diaz R, Pereira E, Caicedo A. The Pericyte of the Pancreatic Islet Regulates Capillary Diameter and Local Blood Flow. *Cell Metab*. 2018;27(3):630–644.e4. doi:10.1016/j.cmet.2018.02.016
- Errico C, Osmanski BF, Pezet S, Couture O, Lenkei Z, Tanter M. Transcranial functional ultrasound imaging of the brain using microbubble-enhanced ultrasensitive Doppler. *Neuroimage*. 2016;124(Pt A):752–761. doi:10.1016/j.neuroimage.2015.09.037

Chapter 7: Vaporizable contrast agents for drug delivery

1. Acoustic vaporization of composite droplets

Similarly to ultrasound imaging, therapeutic ultrasound remains limited by the diffraction limit. The treatment often affects the surrounding tissues, which can be fragile, such as nerves, arteries or brain tissue. Moreover, the ultrasound therapeutic frequency cannot significantly be reduced to treat deeper or transcranial structures, without directly affecting the accuracy of the therapy. It is, in particular, true for acoustic droplet vaporization (ADV) where microdroplets (MD) are released using focused ultrasound. The release area corresponds to the size of the focal spot. These MD were introduced for localized drug-delivery using acoustic vaporization (***Kripfgans, O.D et al 2000, Fabiili M et al 2010***). They are formed as a double emulsion (water in perfluorohexane (PFH) in water) where the PFH phase acts both as a barrier between the inner phase and the outer phase, but also as a vaporizable matrix that converts into a gas with an appropriate drop in pressure initiated by an ultrasound wave. The main application of such droplets would be as cargos for precise delivery of drugs. We propose an approach to attain subwavelength precision in targeted drug-delivery. To achieve this goal, we exploit the interaction between ultrasound and microdroplets (MD) characterized by a very sharp release pressure threshold (***Couture O et al, 2011, Couture 0 et al 2012***). The idea is that the intensity of the focused pulse can be chosen so that the size of the area where the pressure is higher than the release threshold of MD can be controlled precisely. We first had to develop a production system able to form monodisperse droplets with a high throughput. Then, we proved in an in vitro setup that sub wavelength delivery could indeed be obtained. Finally, we show that sub wavelength monitoring of the delivery can be performed concurrently with the same probe used for delivery using similar concepts as in ULM. These results were published (***Hingot V et al 2017***).

2. Microfluidic chip design for micro droplet production

The payload of microdroplets increase with MD volume. Bigger MD would carry bigger loads. However, biocompatible MD sizes should be smaller than the smallest vessels (< 10 μm). To achieve sub wavelength delivery, the release threshold needs to be as sharp as possible. To do this, we developed a terraced microfluidic chip composed of two rivers (*Figure 1.A*). In the first river flows the inner phase of the microdroplets, an emulsion of PFH and an aqueous phase containing the load, here fluorescein. In the second river flows the outer phase, water, and surfactant. 128 micro channels link the two rivers and make the inner phase flow through the outer phase. Upon exit of the channel, a bud forms and eventually detach to encapsulate the inner phase in the outer phase to form a droplet (*Figure 1.B*).

A terrace on the exit of the channels confines the droplet and enables the control of the release time and of the size of the droplet (***Teston E et al. 2018***). An analysis of different parameters driving the detachment of the droplets showed that surface tension, as well as the outer phase flow velocity, could be tuned to allow the formation of stable and monodisperse droplets with a mean diameter of 4 µm and polydispersity index down to 5 % (*Figure 1.C*). In these conditions, the release threshold is known to be sharp (***Couture O et al, 2011, Couture 0 et al 2012***).

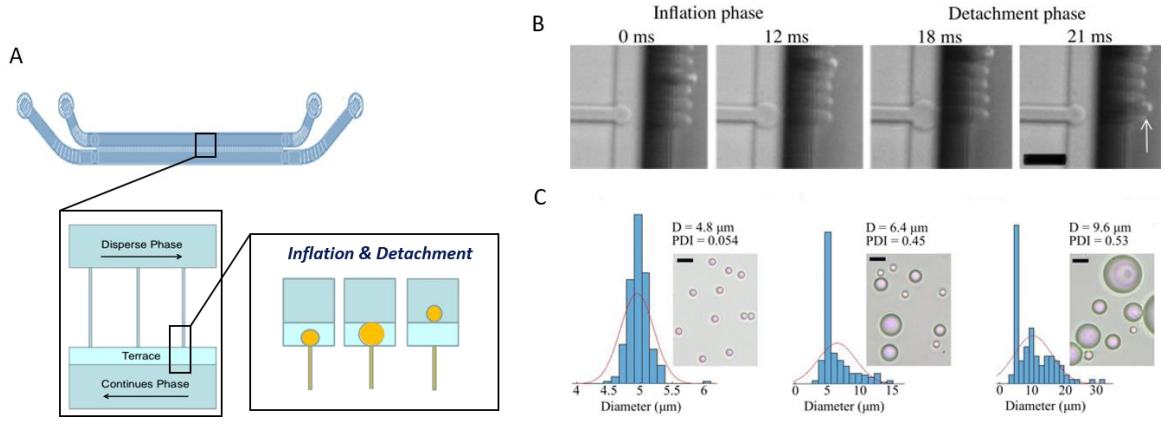

Figure 1: Microfluidic production of microdroplets for Acoustic Droplets Vaporization

A. Terraced system for parallel microdroplets production using two major channels, a feeding channel with the dispersed phase to be encapsulated and the continuous phase to form the droplets, and 128 parallel production channels and the production terrace. B. High speed images of microdroplets production. After an inflation phase, the droplets are detached and carried away by the flow in the continuous phase channel. C. Characterization of polydispersity and sizes in different production conditions. (***Teston E et al. 2018***)

3. Monodisperse droplets to overcome the release diffraction limit

Approximatively 10 million composite droplets were injected in a cell culture plate placed horizontally in a water-bath for acoustical coupling. The plate was observed through a macroscope (Leica, MZ10F) with an 8 X magnification and pictures are taken with an SLR camera (Canon EOS70D). This plate was also placed above a 128-elements linear array used at 5 MHz central frequency (wavelength 300 µm). The array was piloted by a programmable ultrafast scanner. It was used to generate focused pulses for ultrasound-induced delivery with increasing pressures between 1 and 5.2 MPa peak-negative pressure (PNP) for 4 µs. For monitoring, delivery pulses were followed by 200 plane-wave images (13 kHz frame rate).

Increasing the pressure from 1 to 5 MPa, we could set the intersection between the pressure of the focused pulse and the release threshold and choose the size of the release zone. The smallest release zone that could be obtained was 70 μm or λ/4. Similarly, two release spot could be performed distant of 70 μm while leaving a gap between the two. Using ultrafast plane wave directly after the pulse, we could image the microbubble formed after the vaporization of the MD as it formed an echoic cloud. It was also possible to localize two close but delayed pulses and vaporization with a precision of 100 μm λ/3. This was done using ultrasound only.

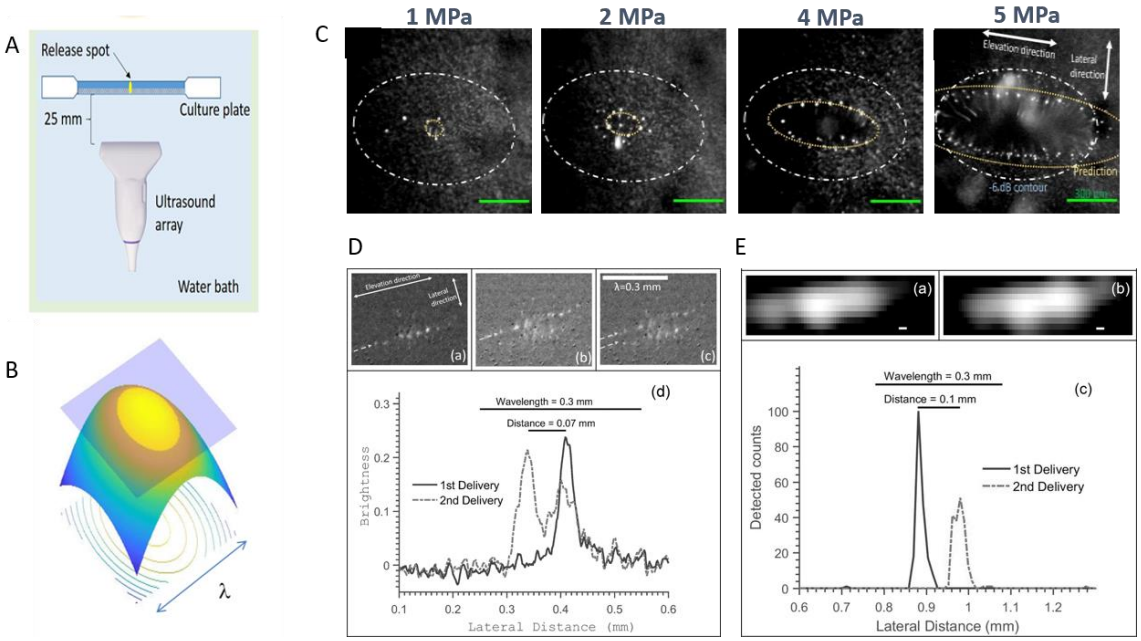

Figure 2: Subwavelength delivery using composite microdroplets

A. Experimental setup for in vitro delivery of fluorescein loaded microdroplets, the camera being on top of the culture plate. **B**. Pressure repartition of an ultrasound pulse. Only droplets within the central area will receive a pressure higher than their release threshold and vaporize. **C**. Shaping the size of the release zone by controlling the pressure of the ultrasound pulse. **D**. Separating two pulses by λ/4. **E**. Monitoring the release of two pulses distant of λ/3 using only ultrasounds.

4. Hemorrhagic conversion limits the use in vivo

Initially, the microdroplets were supposed to be loaded with a powerful anti-cancerous drug. A first proof of concept of release in vivo was needed before engaging in the heavier step of loading the droplets with the drug. We chose to use luciferin which pairs with an enzyme called luciferase that can be present in an adequate model of tumors. When luciferin and luciferase get in contact, they produce luminescence. Therefore, we could detect where the load would meet the tumors.

Unfortunately, the tumors always produced luminescence even when the droplets were injected without being activated by ultrasound pulses, which indicates that our droplets leaked in the general circulation (*Figure 3.A*). Fixing the leakage has not been a simple task and remains the major issue with these droplets even to this day.

Moreover, we noticed that the skin tended to bruise where we targeted the ultrasound pulses. A closer looked indicated clear hemorrhages where microdroplets were activated by ultrasound (*Figure 3.B*). We started investigating this in an in vitro model of vascular network made of cultured endothelium and discovered that the combination of droplets and ultrasound do impact quite drastically the integrity of vessels (*Figure 3.C* & *Figure 3.D*). This was another blow to the idea of safe and efficient drug delivery using microdroplets, but we decided to try the disrupting abilities of the microdroplets to disrupt the vasculature in the tumors.

Although we could get marks on the skin, we never saw evidence of damage to vessels inside the tumors. We tried in other organs who were all shattered by the droplets but tumors remain intact. We did perform ULM in these tumors (*Figure 3.E*) which indicates that the size of the droplets was not the reason of the failure. Our main hypothesis is that the pressure in the tumor and the confinement of the droplets in the chaotic and small vessels increased the release threshold and didn't allow for vaporization.

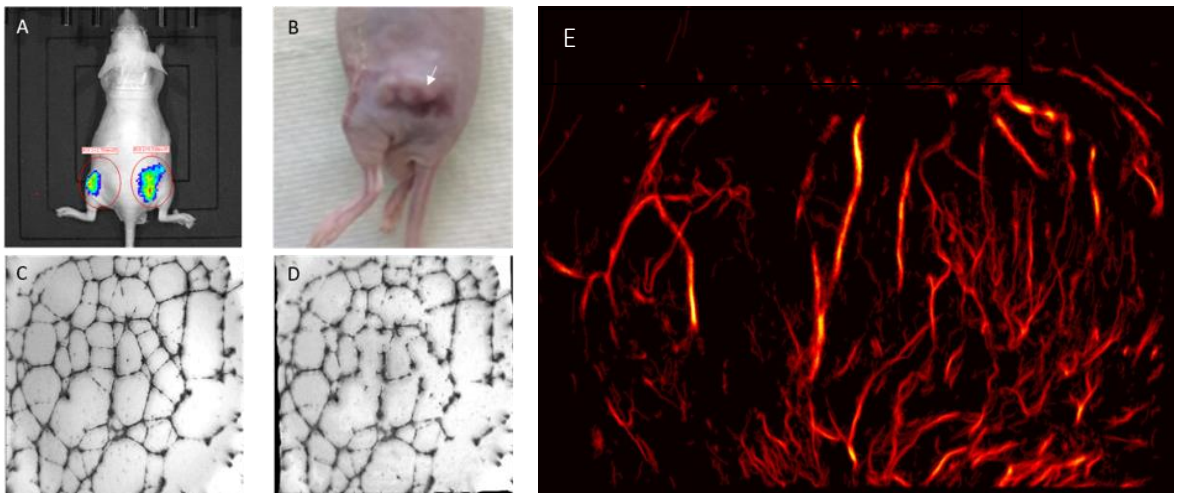

Figure 3: Microdroplets release in vivo, leakage, and hemorrhage

A. Without ultrasound pulses, luciferin leaks out of the droplets and activate luciferase in tumors. B. hemorrhage in the mouse skin. C. In Vitro vascular network before MD induced disruption. D. In Vitro vascular network after MD induced disruption. E. ULM in tumors show no sign of disruption after vaporization.

5. Conclusion

The main result of this project is that using monodisperse vaporizable agents, we were able to control the size of the release zone and perform a form of super resolution in therapy. Although this will be challenging to reproduce in vivo, the concept of super resolution in delivery could be translated to other contrast agents with sharp thresholding behaviors, like MB during the opening of the Blood Brain Barrier, or liposomes when exposed to heat. As for the use of microdroplets as cargos or vessel disrupters, their use for medical application seems shady to say the least. The evidence of hemorrhagic conversion, however, could serve as a warning for people pushing vaporizable agents for imaging and therapy, as they might cause involuntary damage even at low pressures within clinical imaging standards.

6. References

- Organisation mondiale de la santé. Global status report on noncommunicable diseases 2014: attaining the nine global noncommunicable diseases targets; a shared responsibility. (World Health Organization, 2014).
- Thiebaut, A. M. et al. The role of plasminogen activators in stroke treatment: fibrinolysis and beyond. The Lancet Neurology **17**, 1121–1132 (2018).
- Tanter, M. & Fink, M. Ultrafast imaging in biomedical ultrasound. IEEE Transactions on Ultrasonics, Ferroelectrics, and Frequency Control **61**, 102–119 (2014).
- Deffieux, T., Demene, C., Pernot, M. & Tanter, M. Functional ultrasound neuroimaging: a review of the preclinical and clinical state of the art. Current Opinion in Neurobiology **50**, 128–135 (2018).
- Macé, E. et al. Functional ultrasound imaging of the brain. Nature Methods **8**, 662 (2011).
- Demené, C. et al. 4D microvascular imaging based on ultrafast Doppler tomography. NeuroImage **127**, 472–483 (2016).
- Tiran, E. et al. Transcranial Functional Ultrasound Imaging in Freely Moving Awake Mice and Anesthetized Young Rats without Contrast Agent. Ultrasound in Medicine & Biology **43**, 1679–1689 (2017).
- Demene, C. et al. Functional ultrasound imaging of brain activity in human newborns. Science Translational Medicine **9**, eaah6756 (2017).
- Imbault, M., Chauvet, D., Gennisson, J.-L., Capelle, L. & Tanter, M. Intraoperative Functional Ultrasound Imaging of Human Brain Activity. Scientific Reports **7**, 7304 (2017).

- Errico, C. et al. Ultrafast ultrasound localization microscopy for deep super-resolution vascular imaging. Nature **527**, 499–502 (2015).
- Couture, O., Hingot, V., Heiles, B., Muleki-Seya, P. & Tanter, M. Ultrasound Localization Microscopy, and Super-Resolution: A State of the Art. IEEE Transactions on Ultrasonics, Ferroelectrics, and Frequency Control **65**, 1304–1320 (2018).
- Cobbold, R. S. C. Foundations of Biomedical Ultrasound. (Oxford University Press, 2007).
- Montaldo, G., Tanter, M., Bercoff, J., Benech, N. & Fink, M. Coherent plane-wave compounding for very high frame rate ultrasonography and transient elastography. *IEEE Transactions on Ultrasonics, Ferroelectrics, and Frequency Control* **56**, 489–506 (2009).
- Hingot, V. *et al.* Subwavelength far-field ultrasound drug-delivery. *Appl. Phys. Lett.* **109**, 194102 (2016).
- Heiles, B. *et al.* Ultrafast 3D Ultrasound Localization Microscopy using a 32×32 Matrix Array. *IEEE Transactions on Medical Imaging* 1–1 (2019). doi:10.1109/TMI.2018.2890358
- Provost, J. *et al.* 3D ultrafast ultrasound imagingin vivo. *Phys. Med. Biol.* **59**, L1–L13 (2014).
- Provost, J. *et al.* 3-D Ultrafast Doppler Imaging Applied to the Noninvasive and Quantitative Imaging of Blood Vessels in Vivo. *IEEE Trans Ultrason Ferroelectr Freq Control* **62**, 1467–1472 (2015).
- Couture, O., Faivre, M., Pannacci, N., Babataheri, A., Servois, V., Tabeling, P. and Tanter, M. Medical physics,38(2), p 1116 (2011)
- Couture, O., Urban, A., Bretagne, A., Martinez, L., Tanter, M. and Tabeling, P. Medical physics, 39(8), p 5229 (2012).
- Kripfgans, O.D., Fowlkes, J.B., Miller, D.L., Eldevik, O.P. and Carson, P.L. Ultrasound in medicine & biology, 26(7), p.1177 (2000).
- Fabiilli ML, Haworth KJ, Sebastian IE, Kripfgans OD, Carson PL, Fowlkes JB. Delivery of chlorambucil using an acoustically-triggered perfluoropentane emulsion. *Ultrasound Med Biol*. 2010;36(8):1364–1375. doi:10.1016/j.ultrasmedbio.2010.04.019

Chapter 8: Conclusion and Perspectives

1. My main contribution in Ultrasound Localization Microscopy

The long term objective in which my work took place is the creation of a human stroke scanner to make a rapid diagnostic of ischemic or hemorrhage stroke based on ULM. Together with another Ph.D. student Baptiste Heiles, we started our Ph.D. shortly after the first proof of concept for 2D ULM in the rat's brain. We worked in strong collaboration to understand how to make ULM more reliable and improve image quality, in terms of data acquisition and processing algorithms. He successfully translated the technique to 3D whereas I translated the technique to study animal models of stroke. I characterized the spatial and temporal resolution of ULM, and developed a motion correction strategy to enable ULM imaging in moving organs like kidneys, spinal cord or tumors. Our work now enables to perform ULM relatively simply, in various animal models and organs, with a fast and performant processing framework. It provides in vivo imaging of the vasculature with a combination of precision, sensitivity, and depth unmatched by other imaging techniques. It necessarily comes with specific drawbacks, like the need for contrast agents and the relatively long acquisition times but overall has to advantages to make up for it.

In the field of ULM, the motion correction strategy I develop, although simple, was adapted in other groups (***Harput S et al 2018***) and should allow the improvement of image quality in moving organs. The precise characterization of the tradeoff between spatial resolution and acquisition times posed several fundamental issues that people are started to address. In particular, how to accelerates the acquisition time without degrading the image (***Van Sloun et al 2019***), along with fundamental questions around the behavior of MB in the capillaries and how they precisely affect image reconstruction.

Today, the human stroke scanner on its way with the beginning of a new preclinical study of ULM in animal model of stroke, but this time in 3D and through rat's skulls and should be followed by a validation step in sheep before it can finally be tested in human patients. The major question that will have to be addressed is the quality of the images through the skull. Models for signal to noise ratio of MB after imaging through the skull, as well as in vitro proof of concept show that performing ULM through the skull should work (***Siouloti D et al, 2019, O'Reilly M et al. 2013***). However, in order to be of use for doctors, it needs to not only work, but to be a lot better than the methods they have today, in order to compensate for the change of system and the necessary injection of contrast agent.

2. Future developments in super resolution ultrasound

Non localization approaches

The major drawback of ULM is the elongation of acquisition time to several minutes as well as the need for contrast agents. This are relatively minor concerns when comparing to other medical imaging modalities for perfusion imaging, where acquisition times are tens of minutes and the contrast agents more toxic. Acoustic Structured Illumination is an interesting approach that was proposed to achieve super resolution without the need for contrast agents. It is an analog of Structured Illumination Microscopy (SIM) and can improve the axial resolution by a factor 2 without affecting the frame rate (*Ilovitsh T et al. 2018*).

Another method super resolution method based on contrast agents is an analog of optical fluctuation imaging (SOFI) and relies on statistical decorrelation of MBs (***Bar-Zion A et al. 2017*).** If this can reduce acquisition times in big vessels, MB passage in small vessels is what ultimately determines acquisition times of all contrast agents based super resolution techniques (*Hingot et al. 2019*) and non-localization based techniques shouldn't perform better in terms of temporal resolution to image the capillaries.

Deep learning for MB Localization

A method was proposed to overcome the resolution limit based on deep learning (*Van Sloun RGJ et al 2019*) with shorter acquisition times than ULM. A library of MB signals was simulated at multiple localizations to train a neural network to perform MB localization. It is expected to perform well in situations with dense concentration of MBs though it will have a lower resolution that ULM. Moreover, as the method relies on the presence of MB in the vessels, the limit will ultimately be the presence of MB in vessels and therefore be limited by microvascular flow as we showed in the rat's brain *(Hingot V. et al. 2019).* In the future, we can imagine a set of different methods with different set of acquisition times and resolution, ULM being the longest but most resolved method, ultrasensitive Doppler the fastest and least resolved, and in between, hybrid methods like SOFI or Deep-ULM. Similarly to optical microscopy, ultrafast ultrasound and contrast agents could offer a wide range of solutions to different biomedical constraints.

Phase shift agents could populate the microvascular bed faster

One method that may one day shortens the acquisition times without compromising the spatial resolution relies on vaporization of phase shift agents. Small droplets composed of perfluorocarbon gas have been used as substitutes to gaseous MBs (*Kawabata et al 2007, Sheeran P et al. 2011*). These

agents are vaporized under ultrasonic focalization and turn into stable MBs. Because they are potentially much smaller than MBs, they can be injected in greater numbers and therefore populates the vascular network faster, and eventually reach micro structures where MB could not penetrate, like the extravascular space, especially in tumors, in the lymphatic system.

They also circulate longer than regular MB. They could potentially be used as contrast agents for ULM (***Zhang G et al. 2018***) and have been demonstrated in vitro (*Figure 1.A*). Even if the focused ultrasound pulse has a wide focal point, the release zone of these agents can be controlled with sub-wavelength accuracy (*Figure 1.B*, ***Hingot V et al. 2016***) and could one day be used to locally activate and deactivate nanodroplets in the capillary network thus accelerating considerably the acquisition time for the capillary bed and produce images in a similar fashion than fPALM, with blinking and bleaching of sources.

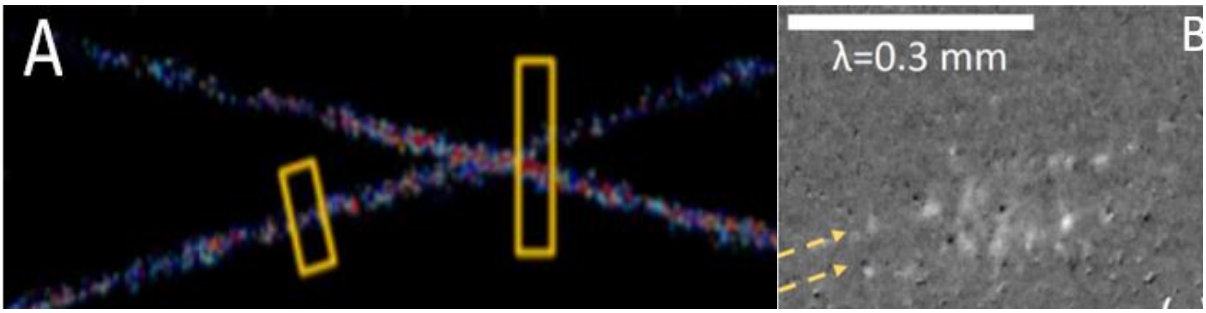

Figure 1: Acoustic vaporization of nano and microdroplets for ULM

A. Vaporization and localization of perfluorocarbon nanodroplets using focused ultrasound (***Zhang G et al. 2018***). B. Control of the release zone for perfluorocarbon composite microdroplets (***Hingot V et al. 2016***).

The future of ULM is 3D

The major limitation of ultrasound imaging is its dependency on the operator and its inability to follow blood and tissue motion in the elevation direction. If ULM turns out to be a convincing method to image cerebral perfusion in the clinic because it might improve image quality, there is little doubt that 3D might help reduce the dependency on the operator. A full 3D angiogram would enable automatic image treatments and will be easier to read by other radiologists. Moreover, a fundamental limitation for ULM is the inability to follow MB flowing across the plane. The same remark is true for motion correction that is ultimately limited by out of plane motions. Although some approaches for 3D were introduced based on 2D scanning (***Errico C et al. 2015, Lin F et al. 2018***), or 1.5 arrays (***Desailly Y et al, 2013***), the development of 4D machines (***Provost J et al. 2014***) eventually enabled first proof of concept for true volumetric ULM.

As ultrafast systems and probes are getting more and more performant, we can now perform 3D imaging and ULM on a 256 channel verasonics system using an appropriately addressed matrix probe. Although new difficulties appeared due the size of the data needed to form a 3D ULM volume (1 To), the framework in ULM was successfully translated from 2D to 3D, using a 32x32 matrix array connected to a homemade 4D ultrafast system, first in vitro followed by impressive 3D renderings in the rat's brain (***Desailly Y et al, 2013***, ***Heiles B et al 2019, Heiles B et al In Prep***).

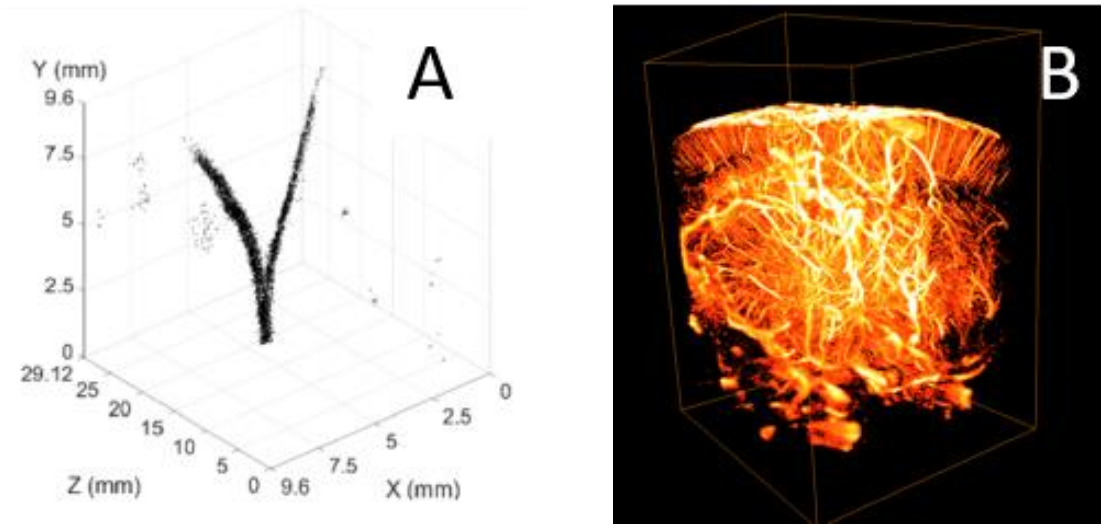

Figure 2: The future of ULM is 3D

A. First proof of concept of 3D ULM in vitro using a 32x32 probe and a volumetric system (***Heiles B et al. 2019***). B. First proof of concept of 3D ULM in vivo using a 32x32 probe and a volumetric system (***Heiles B et al. In Prep***)

3. General consideration and conclusion

The work presented in this thesis, in parallel with the thesis of Baptiste Heiles on 3D ULM, paves the way for the making of the first ultrasound based human stroke scanner. We demonstrated that ULM could image the whole brain and that it was adapted to the imaging of stroke. Hopefully, the translation to the first human patients will be successful in the coming years and will help medical care for patients affected with stroke. It is not clear when ULM would be better than other imaging techniques. The conditions in which imaging systems are used are often dictated by medical constraints, and the long acquisition times might limit ULM to particular medical situations. The research on non-localization based method could allow physicians to choose their imaging method depending on their constraints. Ultrasound systems are relatively cheap and transportable but until recently, image quality was not comparable with CT and MRI. Recent development, and in particular of ULM, showed that ultrasound could be used even more in the future and should be available to more people throughout the world.

4. References

- S. Harput et al., "Two-Stage Motion Correction for Super-Resolution Ultrasound Imaging in Human Lower Limb," in IEEE Transactions on Ultrasonics, Ferroelectrics, and Frequency Control, vol. 65, no. 5, pp. 803-814, May 2018.
- R. J. van Sloun, O. Solomon, M. Bruce, Z. Z. Khaing, Y. C. Eldar and M. Mischi, "Deep Learning for Super-resolution Vascular Ultrasound Imaging," *ICASSP 2019 - 2019 IEEE International Conference on Acoustics, Speech and Signal Processing (ICASSP)*, Brighton, United Kingdom, 2019, pp. 1055-1059. doi: 10.1109/ICASSP.2019.8683813
- O'Reilly, M. A. & Hynynen, K. A super-resolution ultrasound method for brain vascular mapping. Med Phys 40, 110701 (2013).
- D. Soulioti, et al, Super resolution imaging through the human skull, September 2019 IEEE Transactions on Ultrasonics Ferroelectrics and Frequency Control PP(99):1-1
- Ilovitsh, T., Ilovitsh, A., Foiret, J., Fite, B. Z. & Ferrara, K. W. Acoustical structured illumination for super-resolution ultrasound imaging. *Communications Biology* **1**, (2018).
- Bar-Zion, A., Tremblay-Darveau, C., Solomon, O., Adam, D. & Eldar, Y. C. Fast Vascular Ultrasound Imaging With Enhanced Spatial Resolution and Background Rejection. *IEEE Trans Med Imaging* **36**, 169–180 (2017).
- Sheeran, P. S. *et al.* Decafluorobutane as a phase-change contrast agent for low-energy extravascular ultrasonic imaging. *Ultrasound Med Biol* **37**, 1518–1530 (2011).
- Zhang, G. *et al.* Acoustic wave sparsely activated localization microscopy (AWSALM): Super-resolution ultrasound imaging using acoustic activation and deactivation of nanodroplets. *Appl. Phys. Lett.* **113**, 014101 (2018).
- Hingot, V. *et al.* Subwavelength far-field ultrasound drug-delivery. *Appl. Phys. Lett.* **109**, 194102 (2016).
- Provost, J. *et al.* 3D ultrafast ultrasound imagingin vivo. *Phys. Med. Biol.* **59**, L1–L13 (2014).
- Heiles, B. *et al.* Ultrafast 3D Ultrasound Localization Microscopy using a 32×32 Matrix Array. *IEEE Transactions on Medical Imaging* 1–1 (2019).
- Errico, C. et al. Ultrafast ultrasound localization microscopy for deep super-resolution vascular imaging. Nature **527**, 499–502 (2015).
- Desailly, Y., Couture, O., Fink, M. & Tanter, M. Sono-activated ultrasound localization microscopy. Appl. Phys. Lett. 103, 174107 (2013).

– Lin F, et al. (2017) 3-D Ultrasound Localization Microscopy for Identifying Microvascular Morphology Features of Tumor Angiogenesis at a Resolution Beyond the Diffraction Limit of Conventional Ultrasound. *Theranostics* 7(1):196–204. doi: 10.7150/thno.16899

Publication and participation in international conferences

My publications in international peer reviewed journal

- V. Hingot, M. Bézagu, C. Errico, Y. Desailly, R. Bocheux, M. Tanter, O. Couture, Subwavelength far-field ultrasound drug-delivery, *Appl. Phys. Lett.* 109, 194102 (***2016***).
- V. Hingot, C. Errico, M. Tanter, O. Couture, Subwavelength motion-correction for ultrafast ultrasound localization microscopy, *Ultrasonics*77, 17–21 (***2017***).
- O. Couture, V. Hingot, B. Heiles, P. Muleki-Seya, M. Tanter, Ultrasound Localization Microscopy and Super-Resolution: A State of the Art, *IEEE Transactions on Ultrasonics, Ferroelectrics, and Frequency Control* 65, 1304–1320 (***2018***).
- E. Teston, V. Hingot, V. Faugeras, C. Errico, M. Bezagu, M. Tanter, O. Couture, A versatile and robust microfluidic device for capillary-sized simple or multiple emulsions production, *Biomedical Microdevices* 20 (***2018***).
- V. Hingot, C. Errico, B. Heiles, L. Rahal, M. Tanter, O. Couture, Microvascular flow dictates the compromise between spatial resolution and acquisition time in Ultrasound Localization Microscopy, *Scientific Reports* 9 (***2019***).
- B. Heiles, M. Correia, V. Hingot, M. Pernot, J. Provost, M. Tanter, O. Couture, Ultrafast 3D Ultrasound Localization Microscopy using a 32×32 Matrix Array, *IEEE Transactions on Medical Imaging* , 1–1 (***2019***).
- A. Anfray, A. Drieux, V. Hingot, Y. Hommet, M. Yetim, M. Rubio, T. Deffieux, M. Tanter, C. Orset, D. Vivien, Circulating tPA contributes to neurovascular coupling by a mechanism involving the endothelial NMDA receptors, Journal of Cerebral Blood Flow and Metabolism (***Accepted***).

Other publication in preparation

- V. Hingot, C. Brodin, B. Heiles, A. Chagnot, M. Yetim, C. Orset, M. Tanter, O. Couture, T. Deffieux, D. Vivien, Preclinical evidences that early ultrafast ultrasound imaging can be used to predict ischemic stroke outcome and response to treatment. (***Submitted***)
- J. Claron, V. Hingot, L. Rahal, M. Thiebault, J. Baranger, I. Rivals, O. Couture, M. Tanter, S. Pezet, Ultrafast ultrasound imaging of the rat spinal cord reveals in depth physiological properties of spinal nociceptive circuits. (***In prep***)
- B. Heiles , V. Hingot, L. Rahal, P. Lopez, C. Rabut, A. Bergel, M. Pernot, M. Tanter, O. Couture, Volumetric ultrafast Ultrasound Localisation Microscopy in vivo (***In prep***)
- B. Heiles, A. Chavignon, V. Hingot, O. Couture, Single particle localization algorithms for ultrasound localization microscopy in silico and in vivo. (***In prep***)

My participation in international conferences

- *Subwavelength far-field ultrasound drug-delivery (*IEEE IUS, 2017, Echocontrast, 2017 (Poster), Le Studium, 2017)
- *Subwavelength motion-correction for ultrafast ultrasound localization microscopy (*IEEE IUS, 2017, Echocontrast, 2017)
- *Microvascular flow dictates the compromise between spatial resolution and acquisition time in Ultrasound Localization Microscopy (*Echocontrast, 2018 (Poster))
- *Preclinical evidences that early ultrafast ultrasound imaging can be used to predict ischemic stroke outcome and response to treatment (*IEEE IUS, 2018 (Poster), IEEE IUS, 2019)

Figure Index

Annex 1: Protocol for ULM in the rat's brain

Animal preparation

The skull bone had to be removed to maximize the contrast between microbubbles and tissues and to limit aberrations. As in previous studies, Adult Sprague Dawley rats were anesthetized with medetomidine (Domitor ®, 0.3 $mg.kg^{-1}$) and ketamine (Imalgène®, 40 $mg.kg^{-1}$), a catheter was placed in the jugular vein and the head of the animal was fixed in a stereotaxic frame. A cranial window was carved using a 1.4 mm drill and the skull bone was removed, leaving the brain intact. Agar gel was put on the brain to make a protecting layer and ultrasound gel was put to ensure coupling with the probe. Vital parameters (body temperature, breathing frequency) were checked regularly to ensure the stability of the animal. All procedures were performed in accordance with the European Community Council Directive of 22nd September 2010 (010/63/UE) and approved by the institutional committee C2EA-59: "Comité d'éthique en matière d'expérimentation animale Paris Centre et Sud" under the protocol 2015–23. All experiments were performed in accordance with the ARRIVE guidelines.

Data acquisition

240 blocs of 800 compounded frames, with angles at −5°, 0°,+5°, at 1000 Hz at a depth of 8 mm were acquired every second using a 15 MHz probe (Vermon, Tours, France) with a pitch of 0.1 mm which enables a 100 µm × 100 µm in plane resolution. The elevation focusing is done by a plastic lens to reach 500 µm at 8 mm in depth. Acquisitions were performed on a programmable ultrafast ultrasound scanner (SuperSonic Imagine, Aix-En-Provence, France). Every bloc is beamformed using a delay and sum beamforming directly on the machine and only the compounded IQ beamformed data are saved at each iteration. Each bloc is 60 Mb and the total dataset is 14 Gb.

Microbubble injection

400 µL of Sonovue microbubbles were injected through a catheter placed in the jugular vein at a steady rate of 80 $\mu L.min^{-1}$ for 5 minutes to keep a stable concentration in the blood stream. After 1 minute of injection, perfusion of microbubbles in the vasculature reached a steady state and acquisition was started. The rats weigh 500 g which corresponds to microbubble injections of 0.8 ml.kg−1, higher than clinical recommendations (0.03 ml.kg−1) but below safety tested doses (<1ml.kg−1) for Sonovue.

MB extraction

To extract MB from surrounding tissues, a first SVD was performed on each bloc of 800 frames. The first 2 singular values were rejected. On the filtered matrix, a second order Butterworth high pass filtered

with a cut frequency of 20 Hz was performed to remove remaining tissue signals and reveal MB signals. In these conditions, the MB signal to noise ratio is around 60dB compared to remaining tissue and blood signal and electrical noise.

Localization

MB signals were found using a local maximum finder. MB was localized with the pixels using an algorithm based on the radial symmetry. Each MB is then stored as a [z,x,t] vector in a general list of all detected and localized MB.

Tracking

Tracking is performed using a pairing algorithm based on the Kuhn-Munkres method for assignment. All distances between MB positions in successive frames are calculated to form an interdistance matrix in the sense of the Euclidian distance. Through simple operations on the lines and columns of the interdistance matrix, an effective pairing can be done by minimizing the sum of the paired distances of all MBs. A second step then links pairs to form continuous tracks. These two steps are done using the function *simpletracker* written by *Tivenez J-Y.* (2019). All tracks are then interpolated to fill any gaps and rounded to the chosen pixel size. Duplicates are removed to form a continuous and unique track along MB path.

Density image

After tracking, data consists of a list of MB tracks rounded on a pre-defined grid size. A density image is reconstructed by summing in each pixel all the MB that passed through it. If we hypothesis a perfect dilution of MBs in the blood, the density image is an equivalent of the CBV as it counts the numbers of detected MB which would be proportional to the volume of blood that passed through the pixel.

Velocity image

Similarly to the density image, a velocity image can be reconstructed from MB velocity. In particular, a specific colormap can be used to indicate MB flowing towards the probe (blue) or away from the probe (red). In the cortex, this reveals the arterial vs venous organization.

Annex 2: ULM images in high definition

Rat's brain

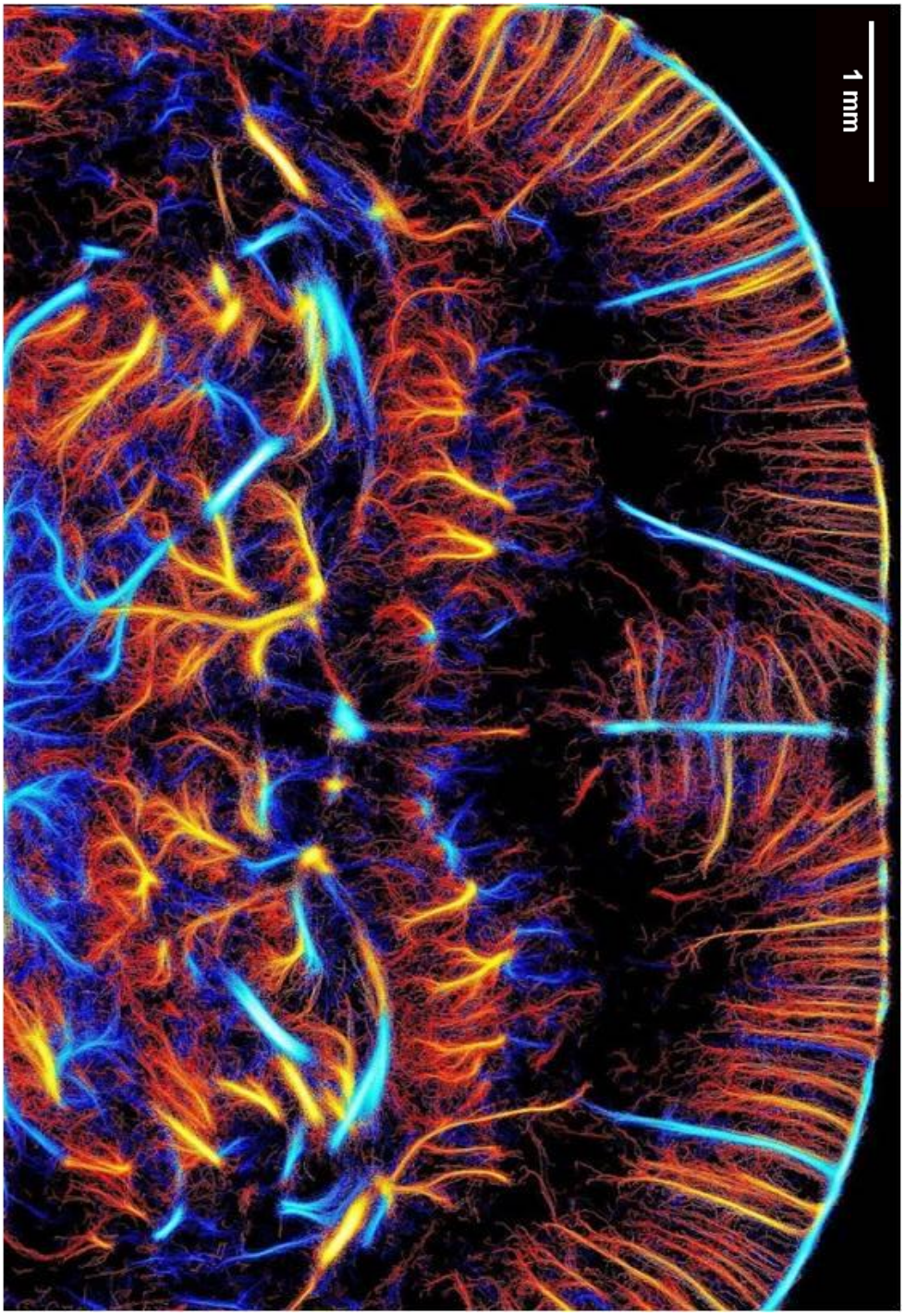

Rat’s spinal cord in a coronal plane

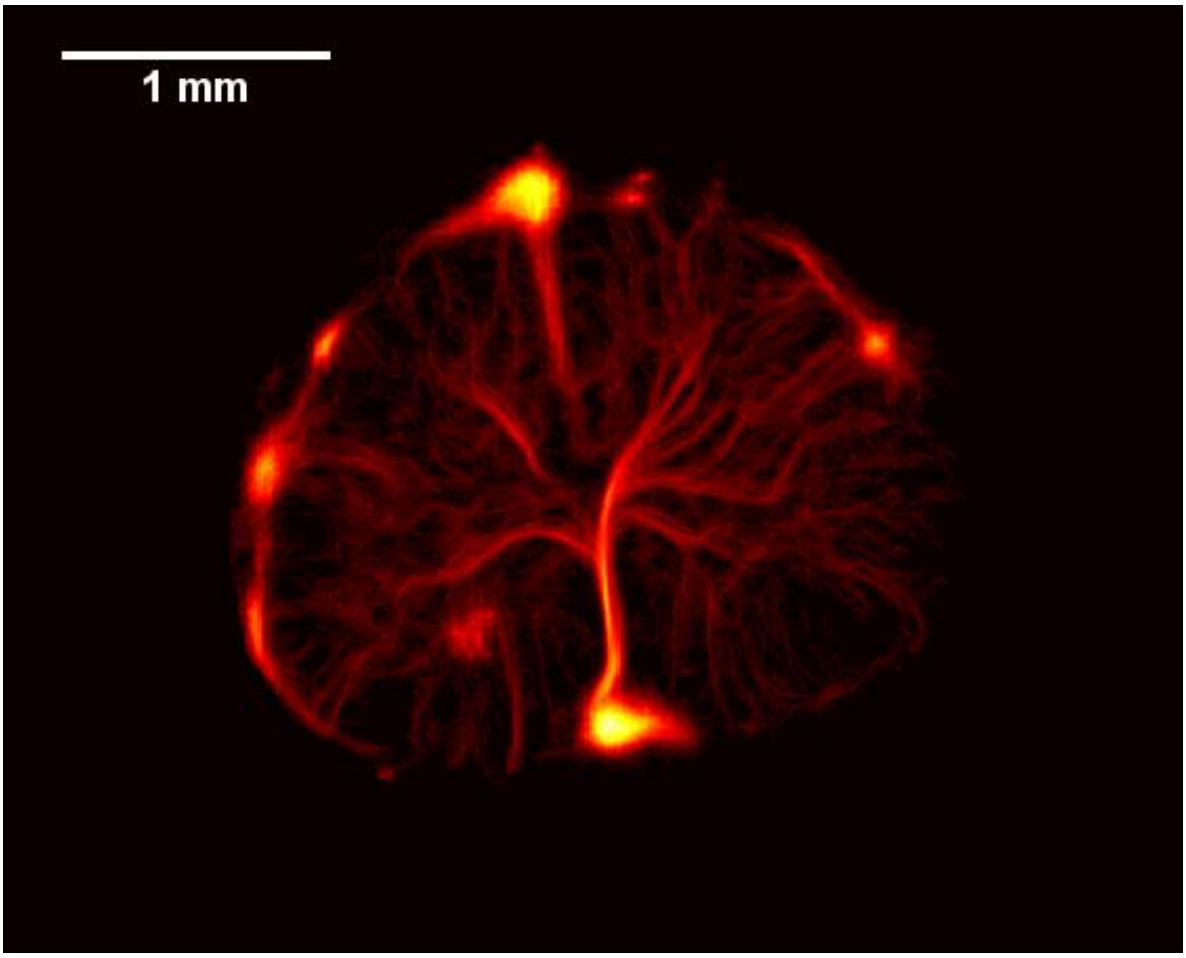

Rat’s spinal cord in a sagittal plane

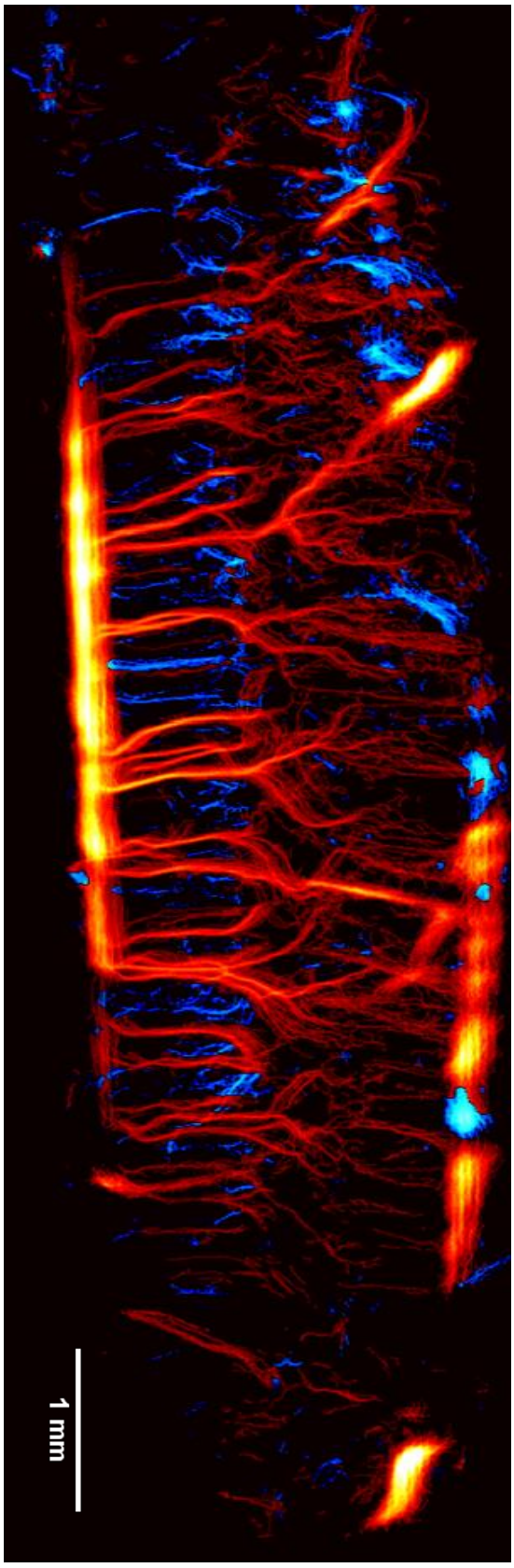

Rat’s kidney

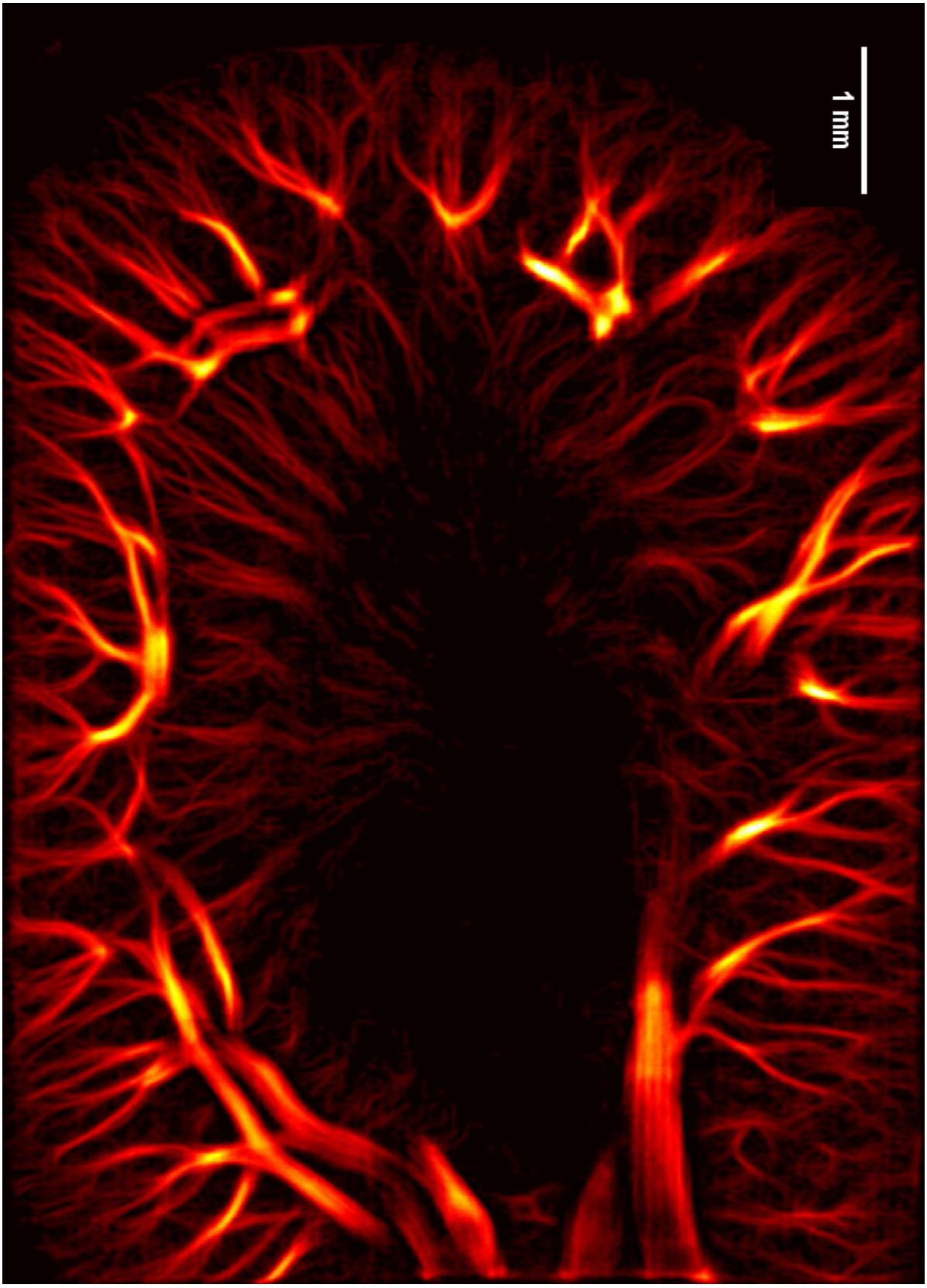

Mouse’s subcutaneous tumor